

UAS MAPPING FOR OIL SPILL RESPONSE IN SANDY BEACH ENVIRONMENTS:
FEASIBILITY AND BEST PRACTICES

A Thesis

by

JACOB BERRYHILL

BS, Texas A&M University Corpus Christi, 2016

Submitted in Partial Fulfillment of the Requirements for the Degree of

MASTER OF SCIENCE

in

GEOSPATIAL SYSTEMS ENGINEERING

Texas A&M University-Corpus Christi
Corpus Christi, Texas

December 2021

© Jacob Lee Berryhill

All Rights Reserved

December 2021

UAS MAPPING FOR OIL SPILL RESPONSE IN SANDY BEACH ENVIRONMENTS:
FEASIBILITY AND BEST PRACTICES

A Thesis

by

JACOB BERRYHILL

This thesis meets the standards for scope and quality of
Texas A&M University-Corpus Christi and is hereby approved.

Michael J. Starek, PhD
Chair

Tianxing Chu, PhD
Committee Member

Jim Gibeaut, PhD
Committee Member

December 2021

ABSTRACT

Oil spill events can be catastrophically harmful to coastal ecosystems, causing considerable and long-term environmental and economic impacts before associated consequences are finally eliminated. Conducting timely, flexible, and accurate surveys immediately after a spill incident is of crucial importance for oil spill response in order to locate the spill, determine the size and volume of the spill, monitor and track the oil movement. Traditional survey methods and visual observations are usually performed for investigating the affected shoreline after an oil spill. Field sketches are used to record and convey the state of oiling in the affected areas. Diagnosis of oiling extent is limited to line-of-sight observations on the ground or by expensive manned aircraft operations.

Recently, Unmanned Aircraft Systems (UAS) have been increasingly employed in various real-world applications, spanning from military scouting and scientific research to urban planning and entertainment. With the rapid development of miniaturized imaging and positioning technologies, UAS Structure-from-Motion (SfM) photogrammetry has become an emerging, cost-effective, and flexible solution for fulfilling various surveying and mapping needs at local scales. This thesis examined the potential and feasibility of using commercially available rotor copter and fixed-wing UAS platforms with SfM photogrammetric techniques to measure and monitor changes in beach elevation for shoreline oiling surveys.

The state of the art of UAS-SfM together with its benefits and generic workflow in oil spill surveying were reviewed. A typical stretch of beach in South Texas was chosen as the study area in the thesis due to abundant historical data collected by the research laboratory from prior projects. The study site contains jetty blocks that provide stable features, as well as beaches that are both maintained and unmaintained. Four objectives were outlined with an effort to develop

guidelines for UAS-SfM best practices for Shoreline Cleanup and Assessment Technique (SCAT).

Based on the data collected at the study area, research findings suggest that without ground control points (GCPs), SfM processing with post-processing kinematic (PPK)-enabled image locations can achieve remarkably higher accuracy than that with autonomous Global Navigation Satellite System (GNSS) image geotags. Adding more GCPs can exponentially improve the overall accuracy for autonomous GNSS geotagged images. For the specific study area, the accuracy performance of the autonomous GNSS geotagged SfM products is on par with that of the differentially corrected GNSS geotagged SfM products with 10 GCPs used for georeferencing. By comparing against coordinates of the check points, the z residuals of a SfM-generated DSM were found better near the center of the beach and worse towards the water and in the dunes and vegetation. Another benefit of using a rigorous GCP control network is it significantly alleviates the bowing effect. Alternative solution for effectively alleviating the bowing effect in time critical survey missions where surveying GCPs is impossible is the use of high overlap oblique imagery and/or multi-elevation coverage. Height adjustments on erratic height values that occurred within autonomous GNSS geotagged images will not improve the accuracy in DSM rendering, however it is still recommended for reducing time and effort in identifying aerial target locations within the image set. When using the PPK operation mode, special attention needs to be paid because a consistent vertical datum should be maintained for the coordinates of both GCPs and image locations throughout the project. In case rapid SfM processing is considered essential for the sake of time, commercial SfM software demonstrated that several hours may be saved in terms of processing, but overall data quality of the geospatial products may have to be compromised.

ACKNOWLEDGEMENTS

I would like to thank Dr. Michael Starek for the guidance that he provided during my work on this project and at the university. I would also like to thank the TGLO for supporting this work. Finally, I would like to thank my amazing family with whom none of this would be possible.

TABLE OF CONTENTS

	Page
ABSTRACT.....	iv
ACKNOWLEDGEMENTS.....	vi
TABLE OF CONTENTS.....	vii
LIST OF FIGURES	xii
LIST OF TABLES	xvii
CHAPTER I: INTRODUCTION.....	1
1.1 Problem Area	1
1.1.1 Oil Spills on Sandy Beaches	1
1.2 Current State of SCAT Surveys.....	2
1.3 UAS-SfM Surveying.....	4
1.4 UAS PaRS for Oil Spill Monitoring.....	7
CHAPTER II: STUDY PURPOSE AND OBJECTIVES.....	9
2.1 Oil Spill Response Benefit from UAS-SfM.....	9
2.2 Study Purpose and Objectives	10
CHAPTER III: BACKGROUND.....	11
3.1 Data Acquisition for UAS-SfM Surveying.....	11
3.1.1 Acquiring Imagery	11
3.1.2 Acquiring Ground Control Points and Accuracy Assessment Data	12

3.2 SfM Processing	13
3.2.1 Feature Detection	13
3.2.2 Keypoint Correspondence.....	14
3.2.3 Identifying Geometrically Consistent Matches	14
3.2.4 Structure-from-Motion (SfM).....	15
3.2.5 Scale and Georeferencing	17
3.2.6 Optimization of Image Alignment	18
3.2.7 MVS Image Matching Algorithms	18
3.3 Spatial Product Generation	19
3.4 Common Problems and Sources of Error	20
3.5 Benefits of Using UAS-SfM with SCAT.....	21
3.5.1 Accuracy Improvements and Cost Efficiency	21
3.5.2 UAS-SfM Vertical Errors and DEM-Based Change Detection.....	22
CHAPTER IV: METHODS.....	24
4.1 Study Area and Equipment	24
4.1.1 Study Area	24
4.1.2 Data Collection Equipment: UAS.....	26
4.1.3 Data Collection Equipment: Ground Control	28
4.1.4. Data Processing: Resources and Software	30
4.2 UAS Surveys.....	30

4.2.1 Monitoring Campaign.....	32
4.2.2 Field Experiment.....	33
4.3 Objective 1. Evaluate UAS-SfM Vertical Accuracy and Change Detection Error	33
4.3.1 Assessment of Control Network Geometry and Image Location Accuracy	33
4.3.2 Bowling Effect Observed in UAS Flights	36
4.3.3 Assessing Impacts of Flight Design and GCPs on Bowling Effect.....	37
4.4 Objective 2. Evaluate SfM Workflows and GIS Analyses for Change Detection	38
4.4.1 SfM Processing Workflows	38
4.4.2 Image Altitude Rectification for UAS Equipped with Autonomous GNSS.....	39
4.4.3 DoD Creation for GIS Analyses	41
4.4.4 Core-Envelope Surface Approach for Repeat Topographic UAS-SfM Surveys.....	44
4.5 Objective 3. Evaluate UAS for Rapid Response and Monitoring	45
4.5.1 Rapid Processing from a Standard Flight Plan	45
4.5.2 Producing an Ortho from UAS Videography	46
4.5.3 Video Documentation of Spills.....	47
4.6 Objective 4. Guidelines for Surveying of Spill Events on Sandy Beaches with UAS	48
CHAPTER V: RESULTS AND DISCUSSION.....	49
5.1 UAS-SfM Vertical Accuracy and Change Detection Error	49
5.1.1 Assessment of Control Network Geometry and Image Location Accuracy	49
5.1.2 Assessment of UAS-SfM DSMs Relative to TLS DSMs.....	50

5.1.3 Assessment of UAS-SfM relative to RTK GNSS Check Points	61
5.1.4 Assessment of UAS-SfM DSM Relative to RTK GNSS Topo Transects.....	61
5.1.5 Best achieved Accuracy from Field Campaigns	64
5.1.6 PPK vs. Autonomous GNSS Onboard UAS with Control	65
5.1.7 Example of UAS-SfM Change Detection Uncertainty with DoDs	65
5.2 Core-Envelope Results.....	67
5.3 Flight Design Impacts for Reducing Bowling Effect	71
5.3.1 Multi-Altitude Flights and Oblique Imagery	71
5.3.2 Rigorous Ground Control Network	75
5.4 SfM Workflows and Processing	79
5.4.1 General SfM-MVS Workflow	79
5.4.2 SfM Workflows Evaluated	81
5.4.3 Tommy Nobel Workflow in Agisoft.....	84
5.5 Autonomous GNSS Image Geotag Elevation Rectification	85
5.6 Orthometric Heights Versus Ellipsoid Heights for Control.....	89
5.7 GSD and Resolving Oiling on a Beach.....	91
5.8 Evaluation of UAS-SfM for Rapid Response Mapping	94
5.8.1 Rapid SfM Processing of Still Images for Orthomosaic Generation.....	94
5.8.2 Comparison of Rapid Processing versus Normal Processing Accuracy	96
5.8.3 Rapid SfM Processing of Videography Data for Orthomosaic Generation.....	99

5.8.4 Advantages of UAS Video to Standard SCAT Reconnaissance	102
5.8.5 Importance of Documenting the Video Flight and Inclusion of Landmarks	103
CHAPTER VI: CONCLUSION	104
6.1 Summary and Contributions	104
6.2 Future Work	106
REFERENCES	108
APPENDIX 1 DESCRIPTION OF FIELD WORK FOR STUDY	117
1.1 Description of all quarterly field days / Data collection	117
1.1.1 10/23/2017	117
1.1.2 02/12/2018	118
1.1.3 06/14/2018	121
1.1.4 08/15-17/2018	123
1.1.5 12/17/2018	126
1.1.6 02/04/2019	128
1.2 Three-day field experiment and GNSS corrections used.....	130
1.2.1 Field work/data collection.....	130
APPENDIX 2 COVER PAGE OF BEST PRACTICES GUIDELINES CREATED FOR THE TGLO INCONJUNCION WITH WRITING THIS THESIS	139
APPENDIX 3 CODE SCRIPT	141
3.1 Code to Calculate the RMSE from a DoD.....	141

LIST OF FIGURES

	Page
Figure 1. SCAT process flow chart.....	4
Figure 2. SfM workflow to process UAS image sequences into densified 3D point cloud, DSM, and orthomosaic. Example here is from Packery Channel; an open-water inlet located along the Texas Gulf coast (Starek et al., 2019).....	20
Figure 3. The extent of the test area, comprising the beach from the Fish Pass jetties at the south end to Beach Access Road No 2. at the north end.	25
Figure 4. eBee Plus equipped with dual frequency GNSS receiver (left). Author launching the system (right).	26
Figure 5. DJI Phantom 4 Pro with remote controller and tablet.	27
Figure 6. Altus APS-3 logging static observations upon an iron rod during the field experiment phase of the study.....	29
Figure 7. Aerial targets used in the study, in detail and as seen from the eBee Plus.....	30
Figure 8. Calendar showing dates of quarterly surveys and 3-day field experiment.....	31
Figure 9. 22 GCPs, this geometry utilized all targets not used as rubric for comparison. The check points shown here in red are the ones compared from every geometry examined. This geometry of control would be considered extremely rigorous for an ordinary survey.....	34
Figure 10. 11 staggered GCPs, this geometry was considered in comparison of the more traditional pair set geometry.	34
Figure 11. 10 GCPs, this geometry consists of point pairs at either end of the survey, the center of the survey, and additional pairs bisecting each half of the survey. This would be considered rigorous for a typical beach survey.....	35

Figure 12. 6 GCPs, this geometry consists of point pairs at either end and the center of the survey. This would be considered a normal geometry for a typical beach survey.	35
Figure 13. 1 GCP, this geometry consists of a single control target in the center of the survey. .	35
Figure 14. 0 GCPs, this final geometry uses no GCPs for constraint of the survey and serves to highlight the higher accuracies of differentially corrected geotags.	35
Figure 15. Oblique view of video flight path.	47
Figure 16. Graph of Z residuals on same 10 check points resulting from separate processing runs utilizing different control geometries, shown in section 4.2.2.4, and image location accuracies PPK vs. Autonomous. Flights were performed with the eBee Plus on 8/16/2018.	49
Figure 17. Day 1 TLS derived DSM.	52
Figure 18. Day 2 TLS derived DSM.	52
Figure 19. Day 3 TLS derived DSM.	52
Figure 20. Day 2 TLS -Day 1 TLS DoD, statistics, and histogram.	53
Figure 21. Day 3 TLS -Day 2 TLS DoD, statistics, and histogram.	54
Figure 22. Day 1 UAS derived DSM.	55
Figure 23. Day 2 UAS derived DSM.	55
Figure 24. Day 3 UAS derived DSM.	55
Figure 25. Day 2 UAS - Day 1 UAS DoD, statistics, and histogram.	56
Figure 26. Day 3 UAS - Day 2 UAS DoD, statistics, and histogram.	57
Figure 27. Day 1 UAS - TLS DoD, statistics, and histogram.	58
Figure 28. Day 2 UAS - TLS DoD, statistics, and histogram.	59
Figure 29. Day 3 UAS - TLS DoD, statistics, and histogram.	60

Figure 30. Metashape generated DSM, and Orthomosaic over base map of 02/04/2019 Phantom 4 Pro Beach Survey with proportional symbols of absolute value of topo point residual.....	63
Figure 31. View of single transect from 02/04/2019 beach survey with DSM, hill shade, orthomosaic, and proportional symbols of absolute value of topo point residual.	64
Figure 32. Day 2 minus day 1 DSM masked for values between -2.06 cm and 2.06 cm.	67
Figure 33. Day 3 minus day 2 DSM masked for values between -4.18 cm and 4.18 cm.	67
Figure 34. Core-Envelope profile 1.	68
Figure 35. Core-Envelope profile 2.	69
Figure 36. Core-Envelope profile 3.	69
Figure 37. Core-Envelope profile 4.	70
Figure 38. Core-Envelope profile 5.	70
Figure 39. Core-Envelope profile 6.	71
Figure 40. Nadir 40-meter imagery with no control.	72
Figure 41. Nadir 40-meter imagery with control.	72
Figure 42. Nadir 40-meter and 55-meter imagery with no control.	72
Figure 43. Nadir 40-meter and 55-meter imagery with control.	72
Figure 44. 10° 40-meter imagery with no control.	72
Figure 45. 10° 40-meter imagery with control.	72
Figure 46. 10° 40-meter and 55-meter imagery with no control.	73
Figure 47. 10° 40-meter and 55-meter imagery with control.	73
Figure 48. 15° 40-meter imagery with no control.	73
Figure 49. 15° 40-meter imagery with control.	73
Figure 50. 15° 40-meter and 55-meter imagery with no control.	73

Figure 51. 15° 40-meter and 55-meter imagery with control. 73

Figure 52. Graph showing K1, radial distortion, and Focal length percentage of difference from camera parameters solution of model with all images and control..... 75

Figure 53. Error profile of Check points showing nadir image data set with and without control. 76

Figure 54. Metashape generated DSM from process with no control. 77

Figure 55. Metashape generated DSM created from process using control. 78

Figure 56. Tommy Nobel Agisoft workflow. 85

Figure 57. DoD showing the micrometer level differences between two very similar processing runs shows texture and elevation relief similar to a hill shade and is included here for novelty. Created by subtracting the unadjusted elevation DSM from the adjusted elevation DSM discussed in Section 5.3. 87

Figure 58. Example of a UAS orthomosaic at 0.45 cm GSD zoomed in at different geographic scales showing the appearance of different size oiling features. The orthomosaic was generated from images captured over a 1-mile section of beach on Mustang Island north of the Fish Pass Jetties. The imagery was acquired on 10/23/2017 between 5:05 and 6:45 pm. This was approximately 73.5 hours after the explosion onboard the Buster Bouchard Barge No. 255, which occurred ~3.25 miles off Port Aransas, Texas. 93

Figure 59. Rapid orthomosaic check point locations..... 97

Figure 60. North end of survey with rapid orthomosaic showing a shift to the Southeast. 98

Figure 61. Center of Survey with Rapid Orthomosaic showing a slight shift to the Southwest. . 98

Figure 62. South end of survey with rapid orthomosaic showing a shift to the Northwest..... 99

Figure 63. Attempted scene reconstruction from video stills with no geotags using rapid processing settings.	101
Figure 64. Attempted scene recreation from video stills with no geotags using medium rapid/accurate processing settings.....	101
Figure 65. Attempted scene recreation from video stills with no geotags using slowest/most accurate processing settings.	102
Figure 66. Attempted Scene Recreation from video stills with no geotags using slowest/most accurate processing settings and minimal control.	102
Figure 67. The aerial target network and Orthomosaic from Day 1, August 15th, showing the control geometry used that gave the lowest residuals on the check points.....	132
Figure 68. The aerial target network and Orthomosaic from Day 2, August 16th, showing the control geometry used that gave the lowest residuals on the check points.....	132
Figure 69. The aerial target network and Orthomosaic from Day 3, August 17th, showing the control geometry used that gave the lowest residuals on the check points.....	132
Figure 70. Day 1 8/15/2018 scanner locations and control target network for the TLS overlaid on a clipped DSM created from the TLS data.	133
Figure 71. Day 2 8/16/2018 scanner locations and control target network for the TLS overlaid on a clipped DSM created from the TLS data.	133
Figure 72. Day 3 8/17/2018 scanner locations and control target network for the TLS overlaid on a clipped DSM created from the TLS data.	133

LIST OF TABLES

	Page
Table 1. Table of UAS flights performed for this study.	32
Table 2. Day 1 Check Point Residuals from the Metashape processing report.	61
Table 3. Day 2 Check Point Residuals from the Metashape processing report.	61
Table 4. Day 3 Check Point Residuals from the Metashape processing report.	61
Table 5. Control Point RMSE for 02/04/2019 DJI Phantom 4 Pro Flight.....	62
Table 6. Check Point RMSE for 02/04/2019 DJI Phantom 4 Pro Flight.....	62
Table 7. Statistics for the two classes of topo points and of all points from DSM value minus topo point value.....	64
Table 8. Metashape processing report check point residuals from process with no control.	77
Table 9. Metashape processing report check point residuals from process with no control.	78
Table 10. Adjusted geotag elevation processing run residuals.	86
Table 11. Unadjusted geotag elevation processing run residuals.	86
Table 12. Adjusted geotag elevation residuals minus unadjusted geotag elevation residuals.....	86
Table 13. Blanket elevation adjustments applied per flight.....	87
Table 14. Adjusted Elevations Average Camera Location Error.	88
Table 15. Unadjusted Elevations Average Camera Location Error.....	88
Table 16. Metashape processing time with normal settings.	95
Table 17. Metashape processing times with most rapid settings.....	95
Table 18. Total RMSE from all check points (no GCPs) in rapid orthomosaic.	96
Table 19. Rapid orthomosaic check point (no GCPs) residuals showing error variance in magnitude and direction.....	97

CHAPTER I :

Introduction

1.1 Problem Area

Shoreline Cleanup and Assessment Technique (SCAT) is a systematic method for surveying an affected shoreline after an oil spill (NOAA, Office of Response and Restoration, 2021). The surveying for SCAT response can be improved with UAS coupled with SfM (UAS-SfM). The capabilities and limits of UAS-SfM surveying on sandy beaches are not well defined.

1.1.1 Oil Spills on Sandy Beaches

2.67 spills of over 1000 barrels occurred annually for each billion barrels of crude oil handled in the United States over the years 1996 to 2010 (Anderson et al., 2012). In 2017, the U.S. consumed 7.26 billion barrels of petroleum products (U.S. Energy Information Administration, 2021). This amounts to at least 19,384 barrels (814,128 gallons) of petroleum products annually ending up in U.S waters, a conservative estimate, as the available statistics are of spills of *at least* 1000 barrels. One article claims the U.S. Department of Energy states the annual figure is 1.3 million gallons annually (Thompson, 2010). Because of the impact to coastal environments due to these spills, the National Oceanic and Atmospheric Administration (NOAA) Office of Response and Restoration (OR&R) has a set of guidelines in place to respond to and mitigate spills. Named the Shoreline Cleanup Assessment Technique or SCAT, the guidelines guide in assessing the many variables such as shoreline qualities, oil type, social and environmental factors then planning cleanup efforts (NOAA, 2013). While a response team is made up of members from many different organizations, SCAT is an integral component of the response effort.

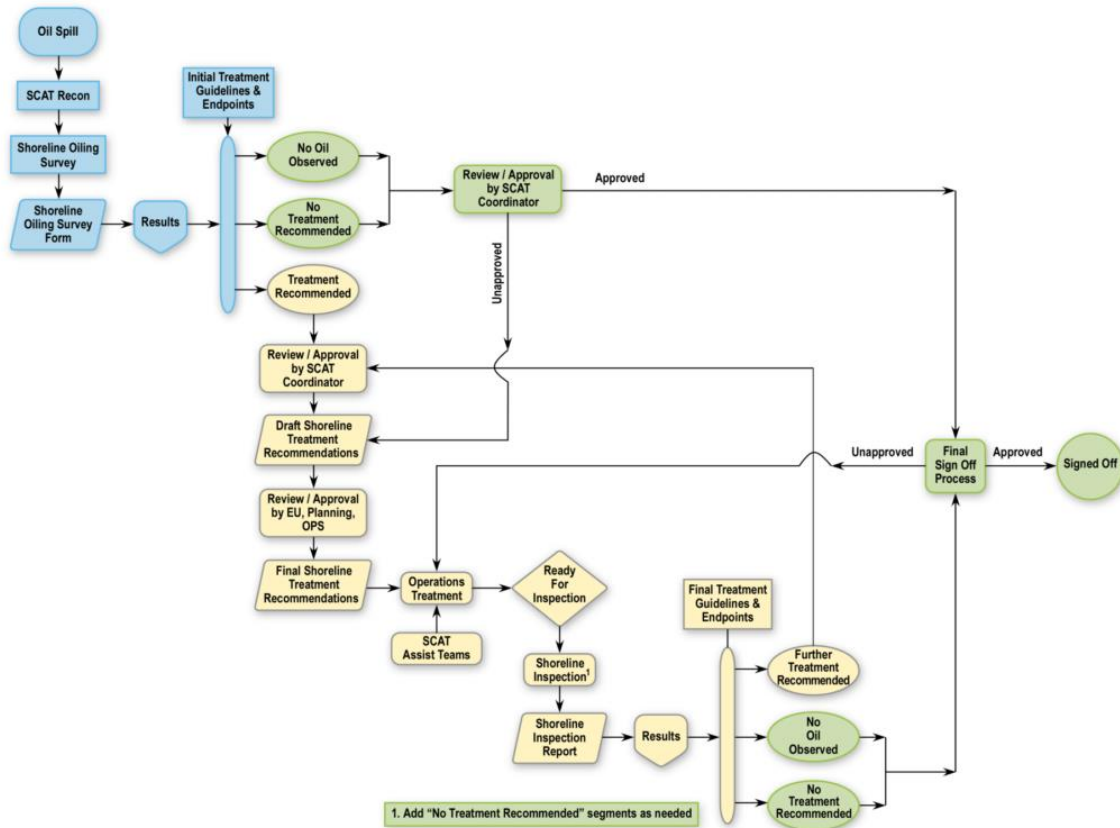
This study focuses on the spill incidents that occur upon sandy beach environments. When spilled oil contaminates shoreline habitats, responders must survey the affected areas to determine the appropriate response. Although general approvals or decision making tools for choosing shoreline cleanup methods can be developed during pre-spill planning stages, responders' specific treatment recommendations must integrate field data on shoreline habitats, oil type, degree of shoreline contamination, spill-specific physical processes, and ecological and cultural resource issues. Cleanup endpoints (when treatment operations can be terminated) must be established early so that appropriate cleanup methods can be selected to meet the cleanup objectives. Shoreline surveys must be conducted systematically because they are crucial components of effective decisions. Also, repeated surveys are needed to monitor the effectiveness and effects of ongoing treatment methods (changes in shoreline oiling conditions, as well as natural recovery), so that the need for changes in methodology, additional treatment, or constraints can be evaluated (NOAA, 2013).

1.2 Current State of SCAT Surveys

The following discussion outlines the basic SCAT process (Figure 1), keeping in mind each component is scalable to meet the needs of the incident. The SCAT process begins as soon as the threat of shoreline oiling is identified. Reconnaissance, by ground, watercraft, or aircraft where appropriate, is conducted to identify the shoreline types, extent (both along-shore and cross-shore) of oiling, and logistical requirements for deploying field teams. Teams are organized and trained, maps and spatial data on sensitive resources and shorelines are compiled and initial cleanup guidelines and endpoints are developed. Based on the priorities to support Planning and Operations Sections, SCAT teams conduct the initial shoreline survey and complete the Shoreline Oiling Survey (SOS) forms. SOS forms are a principal part of the

information chain, conducting information about the shoreline and oiling qualities (such as if oiling was covered by sediment since the spill) and the field team's clean up method recommendations up the chain of command (NOAA, 2013).

The results are evaluated using the cleanup guidelines (allowable shoreline treatment methods for different shoreline types and degree of oiling) and cleanup endpoints (when treatment operations can be terminated), and each shoreline segment is assigned one of three categories: 1) No Oil Observed (NOO); 2) No Further Treatment (NFT) recommended; and 3) Treatment Recommended (TR), which results in the preparation of a Shoreline Treatment Recommendation (STR). STRs consist of a myriad of oil clean up techniques, from manual removal with shovels, rakes and buckets to high tech methods such as steam cleaning or the use of elasticity modifiers, surface collection agents, solidifiers, or biostimulation. Cleanup endpoints should be included as part of the STR. The draft STR is reviewed by appropriate agencies and stakeholders, including required consultations under federal regulations, and submitted for final approval by the Unified Command (UC) before submittal to the Planning Section for issuance to the Operations Section as part of the Incident Action Plan (NOAA, 2013).



SCAT process flow chart.

Figure 1. SCAT process flow chart.

1.3 UAS-SfM Surveying

Unmanned Aircraft Systems (UAS) equipped with digital cameras and sensors are becoming more prolific in the mapping and geomatics world. A number of products can be generated with the data collected by a variety of available sensors. Digital Surface Models (DSMs) and orthorectified image mosaics (orthomosaics) are two of the most common deliverables created from a UAS photogrammetric survey (Starek et al., 2014; Chu et al., 2017). The UAS mapping phenomenon has been gaining momentum in recent years due to advancements in technology and the offering of economical airframes from numerous companies.

The basics of UAS mapping consists of three main steps as summarized below:

Step one is normally laying out a georeferencing control network in the study area. These are typically objects designed to be used as aerial targets and will be visible in the UAS's images at a resolution that allows identification of a specific point in said images. That point is surveyed into a desired coordinate system usually with survey grade GNSS equipment at high precision and accuracy. This step allows for the final map products to be georeferenced to the targets providing data that is spatially accurate to a high degree (Starek et al., 2014). However, this step may be omitted if a high order of georeferencing accuracy is not desired. Omitting step one will result in a product that relies on the geotagging coordinates of the image locations as recorded by the GNSS receiver onboard the UAS. The positional accuracy in a global frame of the final products will typically be a lower order of accuracy with this method compared to using a control network because most UASs rely on a single frequency GNSS unit, similar to the ones in smart phones, to navigate and obtain their positions. In projects that do not require high orders of accuracy this may be acceptable or even desirable as it reduces the survey time greatly by eliminating the need to lay out and measure target positions. There are, however, UASs that utilize dual frequency GNSS receivers that when used in conjunction with corrections from a base station or network can yield accuracies on par with controlled flights without using control (Fazeli et al., 2016). Investigation into the use of said receivers will be a part of this study.

Step two is the flight and image collection. Large areas may be broken up into multiple flights to fit the endurance limitations of the airframe in use. The method of image acquisition is similar to manned Photogrammetry and Remote Sensing (PaRS), bathymetric sonar surveys, or mowing one's lawn. The basic idea is to fly in a back-and-forth grid pattern that will give complete coverage of the target area with the appropriate amount of image overlap (Chang et al., 2017; Gindraux et al., 2017). Ground Sample Distance (GSD) is determined by sensor properties

and flying height Above Ground Level (AGL), or $GSD = (\text{pixel size} \times \text{height above ground level}) / \text{focal length}$ (Greenwood, 2015), with the tradeoff being greater coverage area in a shorter time at higher altitudes but with lower GSD and higher GSD of a smaller coverage area in the same amount of time at lower altitudes. A balance between GSD and flight time is an important consideration for any flight plan.

Step three is the processing of the collected images into a suite of geospatial data products. These normally include a densified three-dimensional (3D) point cloud, DSMs, and orthomosaic when using typical three band RGB cameras. Band specific reflectance maps may be generated when using multispectral sensors that collect light not in the visible range and provided for projects that require them such as agricultural studies, thermography, and other specialized surveys. Normally specific purpose-built commercial software is used for this processing. In general, UAS mapping uses an emergent technique called Structure-from-Motion (SfM) photogrammetry, which exploits information from multiple overlapping images to extract 3D object information and negates the need for precise camera calibration. Topographic SfM is rapidly emerging as a powerful tool for geomorphology applications (Westoby et al., 2012). The UAS-SfM image processing workflow is summarized as follows (Stretcha et al., 2012; Starek et al., 2014; Starek et al., 2019):

1. Image sequences are input into the software and a keypoint detection algorithm, such as the scale invariant feature transform (SIFT), is used to automatically extract features and find keypoint correspondences between overlapping images using keypoint descriptors. SIFT is a well-known computer vision algorithm that allows for feature detection regardless of scale, camera rotations, camera perspectives, and changes in illumination (Lowe, 2004).

2. A least squares bundle block adjustment is performed to minimize the errors in the correspondences by simultaneously solving for camera interior and exterior orientation. Based on this reconstruction, the matching points are verified, and their 3D coordinates calculated to generate a sparse point cloud. Without any additional information, the coordinate system is arbitrary in translation and rotation and has inaccurate scale (Slocum and Parrish, 2017).
3. To further constrain the problem and develop a georectified point cloud, Ground Control Points (GCPs) and/or initial camera positions (e.g., from onboard GNSS) are introduced to constrain the solution. The input GCPs can be used to transform the point coordinates to a real-world coordinate system and to “optimize” rectification.
4. Finally, the interior and exterior orientations for each image are used as input into a Multi-View Stereo (MVS) algorithm, which attempts to densify the point cloud by projecting every image pixel, at a complete or reduced scale. This so called “dense matching” phase can be highly impacted by variations in surface texture as well as MVS algorithm utilized.

While UAS photogrammetry and remote sensing is a relatively young method, it is currently being applied successfully to many problems and gathering spatial information of a higher density and at a lower cost than traditional survey methods (Starek et al., 2019; Stanton et al., 2017; Chu et al., 2017; Zarco-Tejada et al., 2014).

1.4 UAS PaRS for Oil Spill Monitoring

Some works have been published to date that explore the use of light weight consumer UAS during oil spill events. A study by Al-Shammari focuses on detection and mapping of oiling on open water bodies using thermal sensors (Al-Shammari et al., 2018). Another study

that focused on open ocean spills and mapping using UAS systems explored novel methods of swarm coordination, using multiple UAS in cooperation for mapping spill events (Odonkor et al.). A paper that focuses on automatic detection of oil spill using a combination of deep learning and traditional algorithms on UAS images that shows promise in reducing costs when compared to manual inspection methods (Jiao et al.). These works focus on detection and mapping in open waters but do not apply to oiling on sandy beaches. Several works have been published on the subject of UAS-SfM for change detection mapping in geomorphologically active areas such as debris-flow torrents in the Swiss Alps (Tjalling et al.) and rocky coast erosion in Japan (Yuichi et al.). Little work, to date, has been done on evaluating the effectiveness of UAS-SfM for application to SCAT on sandy beaches subject to high frequency wave action and tidal flux, such as those found along the Texas Gulf Coast.

CHAPTER II:

Study Purpose and Objectives

2.1 Oil Spill Response Benefit from UAS-SfM

As can be seen in the discussion of the basic SCAT process (Section 1.2), oil spill response has three main stages that involve surveying. Each of these would benefit from the implementation of UAS-SfM. The first stage, called the SCAT Recon, is a reconnoiter survey that involves quickly discerning the extent of the spill and to aid in planning for the second survey stage. The second stage, called the Shoreline Oiling Survey is a detailed spatial analysis of the location, quantity, and type of oiling as well as the determination of geographical features such as soil types and geomorphological concerns, as well as environmental, ecological, and cultural factors present in the area. This survey and subsequent forms filled out from it are the most important factor in determining all efforts that succeed this point. The third SCAT system survey is the monitoring of cleanup efforts. It is used to evaluate progress, qualify completion, expand operations, and to track oiling movement.

All three of these survey stages are currently performed with traditional survey methods and visual observation. Field sketches are used to record and convey the state of oiling in the areas. Diagnosis of oiling extent is limited to line-of-sight observations on the ground or by expensive manned aircraft operations. UAS provides an alternative method for aerial assessment of oiling extent and monitoring its changes over time, such as due to cleanup activities or natural events.

At any time during the SCAT process, natural events (e.g., storms, tidal events) can deposit or remove sediment in the oiling area. These occurrences can either bury oil or wash it out to sea. Traditional SCAT techniques utilize methods such as digging test holes to determine

if oiling was buried and still present after such an event. UAS-SfM products can be of particular use at these times when used to perform change detection analysis in order to determine if an event either deposited or removed beach sediment. This approach would apply to the entire sandy beach rather than at test holes, capturing more information about the beach change and reducing manual labor.

2.2 Study Purpose and Objectives

The purpose of this study is to explore the application of UAS-SfM to current oil spill response methodology in order to determine best practices and guidelines for doing so. Evaluating UAS-SfM on typical Texas Gulf Coast sandy beach environments to monitor oiling events; and specifically determine how accurate UAS-SfM can be when used to monitor beach surface elevation or topography to then track changes in beach surface elevation over time to assess oil burying or removal due to natural events. In support of this overarching goal, the following are the study's research objectives:

Objective 1. Evaluate UAS-SfM vertical accuracy and change detection error on sandy beaches (i.e., signal to noise).

Objective 2. Evaluate SfM processing workflows and GIS analyses for improving surveying and change detection on sandy beaches with UAS.

Objective 3. Evaluate UAS for rapid response and monitoring of oiling events on sandy beaches.

Objective 4. Develop a set of guidelines for surveying of oil spill events on sandy beaches with UAS.

CHAPTER III:

Background

3.1 Data Acquisition for UAS-SfM Surveying

The first step in performing a UAS-SfM survey is to acquire data of the subject area to be modeled. The data needed comes in three types: imagery, imagery identifiable control point data, and vertical accuracy assessment point data. The main considerations when acquiring data are mission planning, laying or marking control targets, measuring control target locations, flying the UAS and obtaining imagery, and if needed retrieving control targets. The following two sections outline the main steps and concerns of data acquisition.

3.1.1 Acquiring Imagery

3D models of landscapes or objects may be produced using SfM photogrammetry on images acquired from terrestrial based cameras. However, the scope of this research focuses on using aerial imagery acquired by UASs. Utilizing a mobile aerial camera platform allows significantly more freedom of the viewpoints needed to create spatial products of stretches of beaches. There are four main considerations when planning a mission for imagery acquisition: the area of interest, the takeoff/landing location, flight line endlap and sidelap, and the flight altitude. All four of these considerations are interrelated and should be considered together when creating a mission plan.

The area of interest (AOI) refers to the specific land that is desired to be mapped. When surveying the subaerial portion of a sandy beach, this is typically the width of the beach from the water to the crest of the dunes, seawall, or structure extant. The main consideration here becomes the length of beach to map.

The takeoff/landing location refers to the place where the UAS is launched and recovered. Typically, the pilot and or observers are stationed here. Different platforms have different requirements for launch and recovery, for example rotor craft can usually utilize a small area whereas a fixed wing may need tens of meters of clear open space.

Flight line endlap and sidelap refers to how much each sequential image overlaps the previous image, and the images on adjacent flight lines, respectively. Typically, a larger amount of overlap is desirable for scene reconstruction while smaller amounts of overlap will provide more coverage while using less energy.

Altitude above ground refers to the height above the scene that the images are taken. A lower flying altitude above ground will generate a higher resolution image (i.e., smaller GSD) and point cloud that can resolve smaller features when compared to higher altitude flights. The flight altitude above the scene chosen greatly effects the amount of area that is possible to cover in a given amount of flight time.

3.1.2 Acquiring Ground Control Points and Accuracy Assessment Data

For improving georeferencing of UAS imagery or SfM products, it is often necessary to obtain real world coordinates of targets or features that can be identified in the acquired imagery. The more accurately the point can be identified in each image, the better it is for use in georeferencing. Often, purpose designed aerial targets are used, but it is possible to use any identifiable feature that can be both accurately measured in the real world and located in the imagery, for example, while not often present on a beach, the corner of a sidewalk or the point of a traffic arrow. During processing, it is possible to constrain one's solution to these Ground Control Points (GCPs) for georeferencing or to utilize them as check points for evaluating the vertical and horizontal accuracies of the model.

Topo points may be obtained within the scene in order to check vertical accuracies of the UAS-SfM produced products, such as a DEM or DSM. These points may be differenced to a generated surface model to compare elevation measurements. In this study a survey grade GNSS system was used to obtain such point data, but the measurements may be acquired by any reliable survey means, such as a total station referenced to a known mark.

3.2 SfM Processing

As briefly described in Section 1.3, the act of transforming an image dataset into a three-dimensional digital model is referred to as SfM/MVS processing or SfM for short. The following eight sections, while not exhaustive, aim to outline the SfM photogrammetry process in some detail.

3.2.1 Feature Detection

Feature detection is a method of extracting descriptions of local points in a way that allows the correct identification of correspondences between those points, often from a large data set of such points, but that is insensitive to changes in orientation, scale, illumination or 3D position (Carrivick et al., 2016). Keypoints are common points that have been identified on several different photographs which allow the different images to be matched and the scene geometrically reconstructed. Locating keypoints within an image set is the goal of the feature detection step in SfM. While there are several methods for locating these keypoints the most commonly used is the SIFT (Scale-Invariant feature transform). The SIFT algorithm follows four major steps which are summarized below. This summary is taken directly from the introduction in Lowe's 2004 paper titled Distinctive Image Features from Scale-Invariant Keypoints.

1. **Scale-space extrema detection:** The first stage of computation searches over all scales and image locations. It is implemented efficiently by using a difference-of-Gaussian

function to identify potential interest points that are invariant to scale and orientation.

2. **Keypoint localization:** At each candidate location, a detailed model is fit to determine location and scale. Keypoints are selected based on measures of their stability.
3. **Orientation assignment:** One or more orientations are assigned to each keypoint location based on local image gradient directions. All future operations are performed on image data that has been transformed relative to the assigned orientation, scale, and location for each feature, thereby providing invariance to these transformations.
4. **Keypoint descriptor:** The local image gradients are measured at the selected scale in the region around each keypoint. These are transformed into a representation that allows for significant levels of local shape distortion and change in illumination.

At this stage, the identified keypoints each have their own multidimensional descriptor. In Lowe's paper the descriptor has 128 elements or features, but varying software and processing settings may lead to descriptors with a different number of elements (Lowe, 2004).

3.2.2 Keypoint Correspondence

The purpose of the keypoint correspondence step is to identify keypoints in different images whose descriptors are similar and therefore likely to represent the same real-world feature. The keypoints are examined in feature space and by using an optimized Euclidean nearest neighbor function, the majority of keypoints with no match in other images are discarded (Lowe, 2004). The remaining keypoints now have a high likelihood of matching with keypoints from other images.

3.2.3 Identifying Geometrically Consistent Matches

The goal of this stage of the process is to ensure that the remaining keypoints are truly representative of the same feature in multiple images and not erroneous due to noise or any other

factor that may have caused a false match. A fundamental matrix (f-matrix), a 3x3 matrix like the essential matrix but for uncalibrated cameras, is calculated for each pair of images that contain multiple keypoints from the same scene (Carrivick et al., 2016). The exact method of its creation will be specific to individual software, but it will apply the principle of collinearity and epipolar geometry. Typically, the f-matrix is created by using the eight-point algorithm (Carrivick et al., 2016; Longuet-Higgins, 1981). To reduce error due to noise, the image keypoints are normalized before solving the linear equations (Hartley & Sturm, 1997). The F-matrices are then solved using an iterative method. The method used will vary by software, but some of the common methods are least median of squares, the random sample consensus (RANSAC) method, the Levenberg-Marquardt (LM) algorithm, and the Hough transform (Carrivick et al., 2016). The keypoints that do not fit within a specified threshold of a matrices' linear solution are then discarded from the set of valid keypoints. Finally, the links between the remaining coincident keypoints in every image pair are organized into tracks. Tracks are defined as connected sets of matching keypoints through the library of images used in the reconstruction (Snavely et al., 2008). Maps of these tracks are made that identify the connectivity of each image (Carrivick et al., 2016).

3.2.4 Structure-from-Motion (SfM)

Structure-from-Motion or SfM is the single process of simultaneously estimating the 3D geometry (structure) of a scene and the different camera poses using a bundle adjustment procedure (Ullman, 1979). The goal of SfM is to simultaneously reconstruct the structure of the scene in 3D, the camera's external parameters, and the camera's internal parameters. The external parameters are the positions and orientations of the images. The internal parameters are the camera calibration values that model the way light moves through the camera onto its sensor.

While many different camera models exist, one of the most commonly used is the pinhole camera model (Carrivicket et al., 2016). Common parameters solved for are focal length, the principal points X and Y, the skew, the tangential, and several radial distortion parameters. Different software uses different camera models with varying amounts of parameters. The internal and external parameters of the cameras are solved in an iterative process called bundle adjustment. Bundle adjustment is the problem of refining a visual reconstruction to produce *jointly optimal* 3D structure and viewing parameter (camera pose and/or calibration) estimates. The parameter estimates that apply to both the structure of the scene and all camera parameters are made by minimizing the value of a cost function that quantifies the model fitting error (Triggs et al., 2000).

An initial estimate of parameter values must be made on a single pair of images before the bundle adjustment procedure can begin. In cases where the parameters are entirely unknown, they may be estimated from a small subset of images using a self-calibration method. In cases where some of the parameters are known, commonly gleaned from image EXIF data such as focal length and location coordinates, they can be incorporated into the initial estimate (Carrivicket et al., 2016). Reprojection error between the projections of each track and their corresponding keypoints is minimized using an iterative bundle adjustment process. As usual, different software have different ways of performing this process. For more information on the process and math involved (Triggs et al., 2000; Zach, 2014) provides a detailed overview.

Once the minimal value of reprojection error is achieved between the two images, one or more cameras are added to the optimization. First, the external camera parameters for the new camera are estimated using various methods like a direct linear transform technique, which is solved iteratively (Abdel-Aziz et al., 2015; Carrivick et al., 2016). Then, a bundle adjustment is

run on this new set of images with the initial pair's parameters and points remaining fixed, allowing the calibration of the new image, and rejecting any keypoints within it that are above a specified error threshold. Next, a global bundle adjustment is performed iteratively on this new set again with the goal of minimizing the value of a cost function. Outlier tracks with keypoints having a high reprojection error are removed after every iteration of the bundle adjustment. New cameras are then added sequentially to the model and the steps repeated until all cameras with an adequate amount of reconstructed 3D points are included in the solution (Carrivick et al., 2016).

This process produces a sparse point cloud and reconstructed camera poses, all in 3D cartesian space. These camera locations and orientations are the basis for all products generated afterwards. This fact emphasizes the importance of achieving a high-quality initial solution for the camera internal and external parameters.

3.2.5 Scale and Georeferencing

If the camera locations are not geotagged in a known coordinate system, the sparse point cloud and camera poses generated so far are in an arbitrary coordinate system since SfM-MVS can only provide relative camera locations and scene geometry (Szeliski, 2011). Typically, users of the data prefer it to be in a known coordinate system to allow aligning it with other spatial data. In the case that the images have lower accuracy autonomous GNSS geotags or none at all, higher order coordinate control in the model is necessary to accurately bring it into a desired coordinate system by performing a coordinate transformation. A commonly used transformation method is the linear similarity transformation that utilizes three global parameters, three rotational parameters, and one scale parameter (Carrivick et al., 2016). Bringing known control points into the model is typically done in either or both of two ways. First is with (GCPs) which are points within the scene possessing known coordinates that can be identified within the model.

This is usually performed by way of aerial targets that can be identified within the image set by the user, allowing the corresponding sparse cloud points to be tracked by the software then used for the transformation (James & Robson, 2012). Alternatively, direct georeferencing is possible if the location of the cameras is known (Turner et al., 2014). Typically, a combination of both methods is used with direct georeferencing providing approximate camera locations when initializing the bundle adjustment and then utilizing control targets to further constrain the solution. In the case that differentially corrected GNSS geotags are available, a higher weight can be given to them during the bundle block adjustment allowing for accurate georeferencing when GCPs are not used (Ryan et al., 2015).

3.2.6 Optimization of Image Alignment

Due to error present in the external and internal camera parameter estimations, non-linear deformations may be present in the model at this stage. The inclusion of control points in the previous stage provides additional estimates of point error that can be used in the minimization of the non-linear cost function as part of an additional bundle adjustment. (Carrivick et al., 2016). Different software have different workflows leaving the performance of this step not always apparent. Furthermore, ground control points of low quality or bad geometry may degrade the accuracy of the survey (Sanz-Ablanedo et al., 2018).

3.2.7 MVS Image Matching Algorithms

With the geometry of the scene and the camera parameters established by generating the sparse point cloud, a Multi-View Stereo (MVS) algorithm is used to create a much denser point cloud. The purpose of MVS is to create a comprehensive 3D scene reconstruction from a set of images having known internal and external parameters. The dense point cloud created by MVS has a greater point density than the sparse cloud by at least two orders of magnitude (Carrivick et

al, 2016). Many types of MVS algorithms exist (Seitz et al., 2006) that are commonly split into four classes: cost function voxel based methods, iterative surface evolution based methods, image space depth map merging methods, and feature point surface fitting methods, also referred to as patch-based methods by Carrivick et al. Who also describes patch based MVS as performing well compared against other MVS methods and notes the widespread use of a method described by Furukawa and Ponce (Carrivick et al., 2016; Furukawa & Ponce, 2010). Regardless of the method implemented by the software used, the dense point cloud generated in the MVS stage of processing is the main product created from the entire SfM-MVS workflow. Subsequent derivative products such as digital surface models or orthomosaics depend on the dense point cloud during some point of their creation.

3.3 Spatial Product Generation

Most SfM software allows for the generation of various spatial products derived from the created model. The most common and useful are the DSM and orthomosaic.

Once a dense point cloud is generated, several spatial products are commonly derived from it. A DSM is a raster on the x-y plane with each cell representing a z value. The DSM is interpolated or gridded from the dense point cloud at a resolution equal to or lower than the GSD of the flight imagery. Some software also allows for the creation of a 3D polygonal mesh, which is a collection of vertices, edges and faces that defines the shape of the modeled scene.

An orthomosaic is a mosaic of the flight images that has been orthorectified. Software uses the elevation data from the DSM or Mesh to warp and skew the mosaiced images in a manner that creates the orthomosaic. An orthomosaic is uniform in scale and has the same lack of distortion as a map and therefore can be used to measure true horizontal distances as it has been adjusted for topographic relief, lens distortion, and camera tilt (Starek et al., 2019).

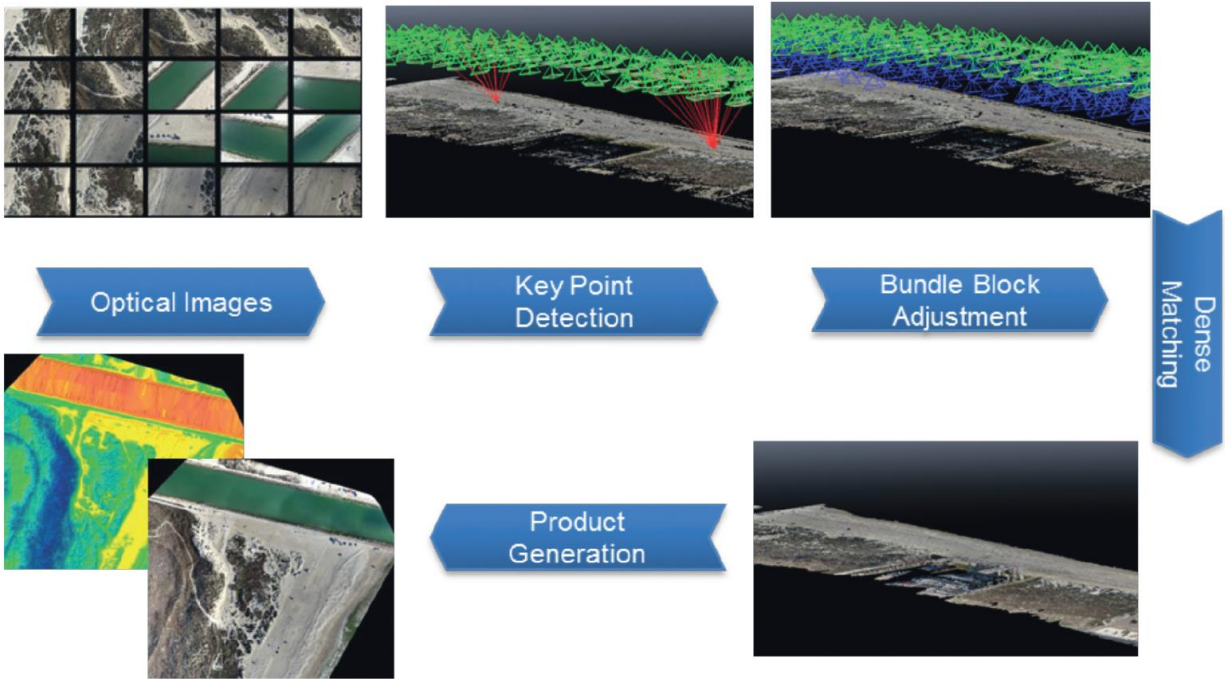


Figure 2. SfM workflow to process UAS image sequences into densified 3D point cloud, DSM, and orthomosaic. Example here is from Packery Channel; an open-water inlet located along the Texas Gulf coast (Starek et al., 2019).

3.4 Common Problems and Sources of Error

Sources of error in UAS-SfM derived spatial data are numerous and sometimes out of control of the surveyor. Things like image texture and color contrast of the scene, ambient lighting, and non-static features can affect the processes’ ability to correctly match points in the image set and lead to error in the camera calibration parameters, estimation of camera exterior orientation, and in point cloud generation (Fonstad et al., 2013). Any deviation from the unknown true camera parameters will subsequently cause error in the data derived from them. Additionally, any errors in image geotags or GCP positional errors, such as due to GNSS error, will propagate directly into the absolute positional error, horizontal and vertical, of the derived coordinates. Since it is impossible to truly know all the parameters from a survey, quantifying

this error is a difficult task and done by way of comparison of the SfM MVS derived data against other survey methods, in the case of this study, against survey grade GNSS collected point data as well as Terrestrial Laser Scanner (TLS) data.

A common and particularly problematic type of miscalibration error effect is known as the “Bowl Effect” (i.e., bowling, doming or dome effect). Corridor surveys such as beaches are more prone to experience this effect than larger rectangular surveys. This is a distortion of the photogrammetric products characterized by a parabolic drift of the model profile and generally caused by unstable and inaccurate internal camera geometries, inaccurate lens radial distortion calibration, overlapping parallel image orientations, low overlap between photographs and large error propagation from GCPs (James & Robson, 2014; Tournadre et al., 2015; Wu, 2014). Unless camera parameters accurately model distortion, particularly in the radial components, a systematic distribution of vertical error can occur (Javernick et al., 2014). Bowling is usually accredited to a lack of strong geometric features within the scene which are important for the self-calibration of the camera model causing systematic distortion (Wackrow & Chandler, 2011). The occurrence of the bowl effect occurred in some UAS-SfM data sets collected in this study and as such, ways to prevent it were investigated and discussed later in this document.

3.5 Benefits of Using UAS-SfM with SCAT

3.5.1 Accuracy Improvements and Cost Efficiency

UAS could be an invaluable addition to the SCAT process in terms of efficiency, accuracy, and level of detail. Using a UAS equipped with a digital camera, a SCAT recon surveyor could have his/her line of sight increased by kilometers. The shoreline oiling survey could take advantage of an accurately georeferenced photo record of the oiling, allowing much more accurate calculations of oiling extent. Furthermore, repeat surveys could allow the tracing

of oiling migration on sandy beaches. Repeat surveys could monitor material accretion (i.e., sediment on sandy beaches) upon the oiling thereby burying it, or oiled surface erosion as the oiling has flowed back into the water. Measurements of the processes are possible and should be investigated as UAS-SfM has the potential to greatly advance the quality, efficiency, and speed of the SCAT process.

For the cost of 3D data, UAS-SfM is relatively inexpensive compared with the only other alternative at similar resolutions, light detection and ranging (lidar). The ease of data acquisition and processing using commercial or open-source software paired with careful application and expert knowledge of total station or differential GNSS surveying, for GCPs, makes UAS-SfM surveying a relatively low overhead addition at local scales to any organization with the goal of mapping accurately and densely sections of coastline (Carrivick et al., 2016). However, presently UAS-SfM is restricted to localized geographic scales due to regulations and restrictions from the Federal Aviation Administration (FAA) in performing beyond-line-of-sight flights. There are several other regulations that a UAS operator must be aware of, which is beyond the scope of discussion here.

3.5.2 UAS-SfM Vertical Errors and DEM-Based Change Detection

Topographic change detection with digital elevation models (DEMs) is the act of comparing DEMs (or DSMs) derived from surveys performed of the same area at different times to create DEM of Difference (DoD) maps and estimate the change in elevation between two overlying grid cells, and net change of the topographic surface. Estimates of net change are inherently controlled by DEM quality, which is in itself dependent on the quality of the survey it was derived from, such as UAS-SfM (Wheaton et al., 2009). A commonly used method for managing DEM uncertainties involves specifying a minimum level of detection threshold to

distinguish actual surface changes (i.e., statistically significant) from vertical change due to measurement error/noise caused by the inaccuracy of the survey. Changes below this threshold can be masked or discarded with changes above this level considered significant (i.e., real). This threshold can be determined as the square root of the sum of the squares of the uncertainties of the DEMs as derived from check data in the form of topo points or check points. Therefore, the use of UAS-SfM derived data for detecting change is only as good as the accuracies in the surveys. Ground truthing data, of higher order accuracy, is needed to quantify the errors of a DEM, which is typically done by calculating the root mean square error (RMSE) of the difference between the elevation of the ground truth points and the DEM at their location.

The American Society for Photogrammetry and Remote Sensing (ASPRS) Positional Accuracy Standards for Digital Geospatial Data (ASPRS, 2014) recommends a minimum of 20 checkpoints to conduct a statistical evaluation of absolute positional errors of point cloud or elevation data derived from photogrammetry. ASPRS also recommends that the survey accuracy of the checkpoints be at least three times more accurate than the data they are evaluating. However, meeting this level of accuracy is not always practical. For example, RTK GNSS is a commonly accepted method for field validation of UAS-SfM accuracy, which may not meet this requirement in the vertical dimension for some UAS-SfM survey scenarios.

When paired with UAS-SfM, the described methods of understanding the limits of temporal surveys could allow for a greater understanding of oiling migration during SCAT response.

CHAPTER IV:

Methods

4.1 Study Area and Equipment

The following sections outline the experiment study area and equipment used.

4.1.1 Study Area

The selected study area is a section of beach on Mustang Island in the Gulf of Mexico near Corpus Christi, Texas. Located inside Mustang Island State Park, Fish Pass was a channel dredged in 1972 but silted in by the early 80s, a set of jetties protrude about 170 meters from the beach at 27°40'36" N, 97°09'55" W. The beach varies in width with the tides, sometimes the water is up to the dunes and sometimes the beach is over 100 meters wide in sections.

The area surveyed is a 3.5 km long tract of beach to the north of and including the north side of the Fish Pass jetties (Figure 3). This area was selected due to the amount of historic data gathered here by this lab from other projects. The site contains jetty blocks that provide stable features, as well as sections of beaches that have different types of maintenance performed. The Southern roughly three quarters of the test site is maintained by the State Park while the remaining Northern section is maintained by the county. These variations throughout the site help to ensure that it serves as a decent analogue for any ocean facing beach in Texas.



Figure 3. The extent of the test area, comprising the beach from the Fish Pass jetties at the south end to Beach Access Road No 2. at the north end.

4.1.2 Data Collection Equipment: UAS

Two fixed wing, small UAS systems were used in this study. First one used was a fixed wing UAS called a Sensefly eBee Plus equipped with an RTK/PPK enabled GNSS. The system has a weight of 1.1kg, a wingspan of 110 cm, and a Sensefly S.O.D.A. camera. The craft has the capability of obtaining differentially corrected GNSS coordinates of each camera position. The Sensefly S.O.D.A. is an RGB, 20-megapixel (5,472 x 3648 pixels) camera that utilizes a 1-inch (13.2 x 8.8 mm) CMOS sensor and a global shutter (SenseFly, n.d.).



Figure 4. eBee Plus equipped with dual frequency GNSS receiver (left). Author launching the system (right).

The second fixed wing system used was a Sensefly eBee, which is similar to the one above but without the differential correction capabilities. It carries the same Sensefly S.O.D.A. camera as the eBee Plus. The craft utilizes an autonomous GNSS for obtaining camera

coordinate positions (SenseFly, n.d.). Both the eBee and the eBee Plus were found to have a maximum flight time of around 55 minutes depending on wind.

Both systems utilize Sensefly's emotion3 flight control software that runs off of a laptop and connects to the airframe via a USB plug in UHF antenna.

The rotor craft used was a DJI Phantom 4 Pro, a 1.39 kg quad rotor equipped with 1 inch 20 megapixel (5,472 x 3648 pixels), global shutter, CMOS camera. The Phantom 4 Pro is equipped with a single frequency GNSS receiver (DJI, n.d.). The flight control software used with the Phantom 4 Pro was DJI's Ground Station Pro which connects to the remote controller with a USB cable.



Figure 5. DJI Phantom 4 Pro with remote controller and tablet.

4.1.3 Data Collection Equipment: Ground Control

The point surveys (e.g., aerial targets, topo points) were conducted with an Altus APS-3 receiver set, operated with a Leica data collector running Carlson SurvCE v5. The Altus APS-3 is a survey grade GNSS receiver using the GPS and GLONASS constellations (ALTUS Positioning Systems, 2013, 2015). For ease of operation a data collector was used. Doing so allows point storage, raw data collection, stake out functions, coordinate geometry calculations and instant application of a geoid model if desired. The device used was a Leica CS-10 running Carlson SurvCE v5 (Leica, n.d.; Carlson, 2016). The same Altus APS-3 receivers were used to log static observations used for the PPK solution of image locations for the eBee Plus. When doing so, the static observation was logged during the UAS's flight. If occupying an unknown point the receiver was left to log a minimum of 2 hours required to get a precise ephemeris solution from the NGS's Online Positioning User Service or OPUS.



Figure 6. Altus APS-3 logging static observations upon an iron rod during the field experiment phase of the study.

The ground control targets used were 61 cm x 61 cm pieces of $\frac{1}{4}$ inch plywood coated in an outdoor oil-based matte paint. Made by the author, the targets were painted with a black base coat upon which a white cross comprised of 10 cm wide strips was stenciled and painted. A 4 cm black circle was left around the dead center of the cross on which a small indentation was made on which a survey pole tip could be easily and repeatedly placed for measurement.



Figure 7. Aerial targets used in the study, in detail and as seen from the eBee Plus.

For a field experiment phase of the project, described in more detail below (see SECTION 4.2.2), a RIEGL VZ-400 was used to collect ground truth data. The RIEGL is a survey grade terrestrial laser scanner that utilizes a laser in the near infrared wavelength and has a range of up to 400 meters. The one used was equipped with a DSLR camera for point cloud coloring (Riegl, 2017). With its RiSCAN Pro software, the collected point clouds can be georeferenced using a variety of methods and used to create a 3D model of the imaged scene.

4.1.4. Data Processing: Resources and Software

For data processing of the image sets a purpose-built Puget Systems computer running windows was used. The machine is equipped with a 12 core Intel CPU, dual Nvidia GTX 1080ti GPUs, a quality solid state hard drive with a pcie M.2 connection, and 128 Gb of ram. For SfM processing, Pix4Dmapper was evaluated, but Metashape was used for all data in the study.

4.2 UAS Surveys

To evaluate the aforementioned study objectives, UAS surveys at the study site were conducted on a routine basis (roughly quarterly) over an approximate 1.5-year period. The

purpose in so doing was to evaluate UAS-SfM processing workflows and application of UAS-SfM for elevation change detection in support of SCAT on sandy beaches. As part of that effort, a three-day field experiment was also conducted where several UAS flights were performed to evaluate influence of different GNSS georeferencing methods on the image locations and impact of GCP network design, on quality and accuracy of UAS-SfM generated survey products. Various platforms were tested and used during these field campaigns. Below are more details on the UAS surveys conducted for these campaigns referred to as Monitoring Campaign and Field Experiment, respectively.

UAS Surveys Performed

- October 23rd, 2017
- February 12th, 2018
- June 14th, 2018
- August 15th-17th, 2018 (3-day)
- December 17th, 2018
- February 4th, 2019



Figure 8. Calendar showing dates of quarterly surveys and 3-day field experiment.

Table 1. Table of UAS flights performed for this study.

Date	Quarter	UAS	Altitude (ATO)	Side lap	End Lap	GSD cm/pix	Geotag Method	Main Purpose	Secondary Purpose	Target #
10/23/2017	Q1	DJI Phantom 4 Pro	20 m	75%	80%	0.6	Autonomous	Bouchard Spill	Quarterly	0
2/12/2018	Q2	eBee Plus	70 m	80%	60% - 70%	1.6	Autonomous	Quarterly	Feasibility Test	10
2/12/2018	Q2	DJI Phantom 4 Pro	70 m	80%	80%	1.6	Autonomous	Quarterly	Feasibility Test	10
6/14/2018	Q3	eBee Plus	119 m	85%	60%-70%	2.8	Autonomous	Quarterly	Topo Survey	22
6/14/2018	Q3	DJI Phantom 4 Pro	100 m	80%	80%	2.53	Autonomous	Quarterly	Video	22
8/15/2018	3-Day	eBee Plus	90 m	85%	60%-70%	2	PPK	Change Detection		32
8/15/2018	3-Day	DJI Phantom 4 Pro	50 m	80%	80%	1.4	Autonomous	Change Detection	Quarterly	32
8/16/2018	Q4/3-Day	eBee Plus	80m	85%	60% - 70%	2	PPK	Change Detection	Quarterly	32
8/16/2018	3-Day	DJI Phantom 4 Pro	Multiple	80%	80%	Multiple	Autonomous	Change Detection	Doming/bowling	32
8/17/2018	3-Day	eBee Plus	80m	85%	60% - 70%	2	PPK	Change Detection		32
12/17/2018	Q5	DJI Phantom 4 Pro	Multiple	80%	80%	Multiple	Autonomous	Quarterly	Doming/bowling	
2/4/2019	Q6	DJI Phantom 4 Pro	30 m	80%	80%	0.8	Autonomous	Quarterly	Topo	26

4.2.1 Monitoring Campaign

Quarterly surveys were performed for a year and a half in support of this study. The goal of this campaign was to gather data for use in exploring and evaluating methods for mapping and visualizing dynamics of sediment movement and topographic change in a sandy beach environment over a prolonged period of time, in order to provide novel options for decision makers during long term oiling treatment and cleanup projects. For detailed information about the individual quarterly surveys see Appendix 1 at the end of this paper.

4.2.2 Field Experiment

A 3-day field experiment was performed that included rigorous ground truthing methods (e.g., TLS, extensive GCP network) to evaluate methods for performing high accuracy georeferencing of UAS-SfM surveys. Three consecutive days were chosen for the surveys to aid in examining detection of change at small levels. The premise being that the sandy beach would not differ greatly from one day to the next. In this manner it was hoped to determine a maximum accuracy achievable and the procedures that allow it. For detailed information about the 3-day experiment surveys see Appendix 1 at the end of this paper.

4.3 Objective 1. Evaluate UAS-SfM Vertical Accuracy and Change Detection Error

This objective evaluated the impact of GCP control network design and accuracy of image geotags derived from the onboard GNSS on UAS-SfM solutions, specifically for monitoring change in sandy beach elevation/sediment. Additionally, this objective examined influence of UAS flight design on the bowing effect, which is often observed in densified point clouds generated from UAS-SfM surveys conducted along linear corridors, such as beaches.

4.3.1 Assessment of Control Network Geometry and Image Location Accuracy

This assessment was performed using UAS surveys performed by the eBee Plus platform conducted over the course of the three-day field experiment (see Table 1). A total of 32 aerial targets, also referred to as GCPs, were laid out for each of the UAS surveys in order to examine how differences in GCP control geometry affects survey accuracy. These coordinates were obtained from the survey grade GNSS equipment using a local base station on a known point, the same station antenna was used to log the static observations used in the PPK processing of the eBee Plus RTK/PPK image locations. Ten of the targets were reserved to be used as check points on each processing run. During SfM processing, the coordinates of the aerial targets are entered

into the software. With the GCP coordinates listed in the software, each target is assigned a location within the images that it appears in. This is done by visually identifying and clicking on the target's center point in each image that contains it. Once the target locations are identified within the images the software can determine their location in the model generated. Each target can then be designated as either a GCP or a check point. When used as a GCP, the point is used to constrain the solution of the model in the SfM software. When used as a check point, the software will give you the residuals from the entered coordinates to the coordinates in the model where the designated location was generated. When used as a check point the software does not constrain to the target's location.

The ten reserved check points' residuals, whose locations can be seen in Figure 9, were examined for six different control network geometries for both the autonomous and PPK corrected image geotags for each of the three days. Examples of the geometries examined are shown below in Figure 9 through Figure 13 using data from day two of the field experiment.

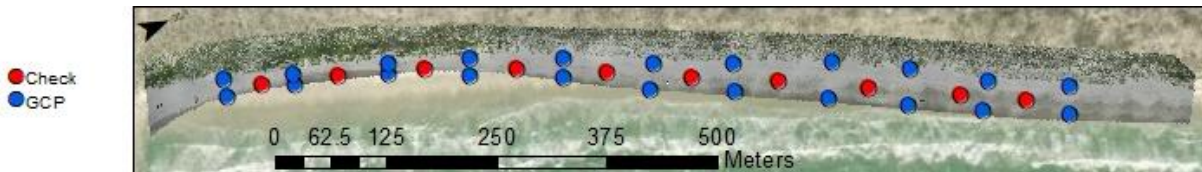


Figure 9. 22 GCPs, this geometry utilized all targets not used as rubric for comparison. The check points shown here in red are the ones compared from every geometry examined. This geometry of control would be considered extremely rigorous for an ordinary survey.

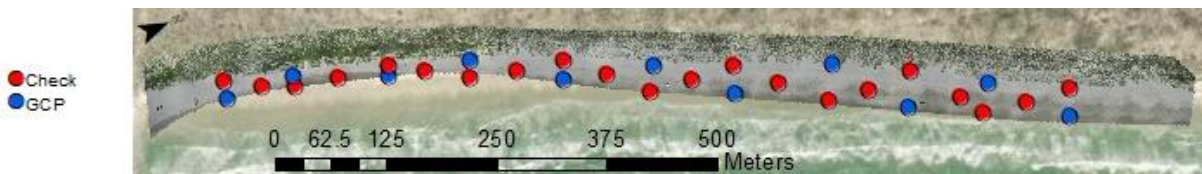


Figure 10. 11 staggered GCPs, this geometry was considered in comparison of the more traditional pair set geometry.

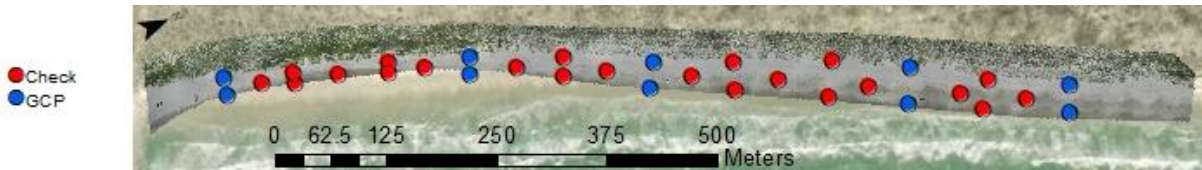


Figure 11. 10 GCPs, this geometry consists of point pairs at either end of the survey, the center of the survey, and additional pairs bisecting each half of the survey. This would be considered rigorous for a typical beach survey.

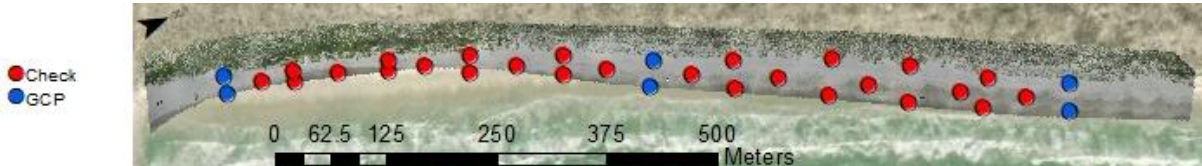


Figure 12. 6 GCPs, this geometry consists of point pairs at either end and the center of the survey. This would be considered a normal geometry for a typical beach survey.

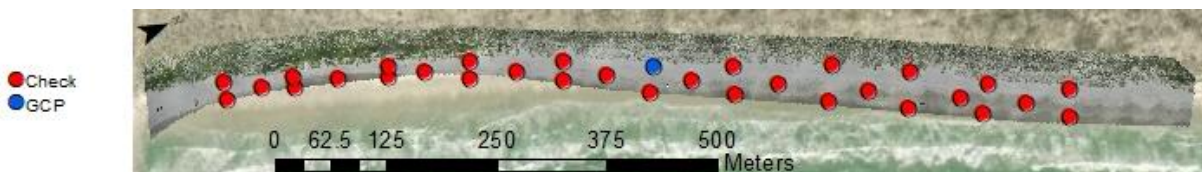


Figure 13. 1 GCP, this geometry consists of a single control target in the center of the survey.

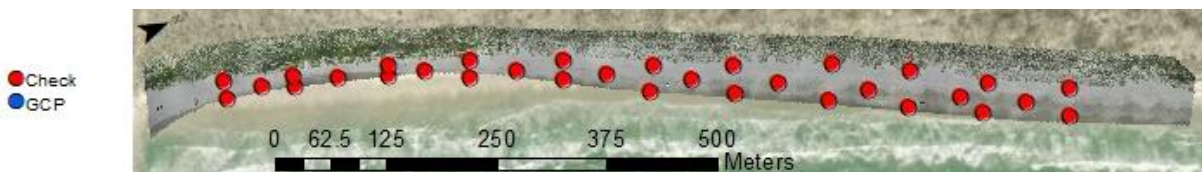


Figure 14. 0 GCPs, this final geometry uses no GCPs for constraint of the survey and serves to highlight the higher accuracies of differentially corrected geotags.

The eBee Plus RTK/PPK utilizes its software, emotion 3, to generate the image locations from its flights. A flight log of the craft's location, attitude, and camera trigger times is generated during flight and stored in memory. After the flight, the flight log is used to create a file of locations that correspond to the images taken. One may either write the image locations, or geotags, to the EXIF data of the images themselves or create a text file of the image names and associated locations for import into processing software. If one has a rinex observation file from a dual frequency static GNSS observation of a known location taken during the flight, it may be

used in conjunction with the flight log to generate differentially corrected image locations. The described method is known as Post Processed Kinematic (PPK). The software, emotion 3, requires the flightlog which contains the rinex observations recorded onboard the UAS during the flight, the rinex file from the static observation, the rinex navigation files for GPS and GLONASS, and the coordinates of the static observation. Once the differential processing is complete the geotags may be written to image exif data or a text file can be created. For the purpose of this study both methods were used. Text files of the image locations were created for both autonomous and PPK solutions for the same set of images. These dual location files were made for the eBee Plus RTK/PPK flights performed each of the three days of the field experiment conducted on August 15th, 16th, and 17th 2018.

The surveys were all processed normally in Agisoft Metashape using the USGS Tommy Noble workflow (described in detail further below), six geometries using autonomous geotags and then the same six geometries using the PPK geotags. These processes were performed for each day of the experiment comprising a total of 36 processes. It is important to note that once the target locations were marked in the images, they were unchanged and used in all processes for that day, for both the autonomous and PPK geotag data. This provided a consistency of target image locations when comparing residuals.

To compare the residuals for each geometry and geotagging method, the residuals were graphed for each geometry and geotagging method from each day.

4.3.2 Bowling Effect Observed in UAS Flights

As described above in Section 3.4, the bowl effect is described as a distortion of the photogrammetric products characterized by a parabolic drift of the model profile and generally caused by unstable and inaccurate internal camera geometries, inaccurate lens radial distortion

calibration, overlapping parallel image orientations, low overlap between photographs and large error propagation from GCPs (James & Robson, 2014; Tournadre et al., 2015; Wu, 2014).

Typically, a bowl effect in data is unexpected and undesired. The effect occurred twice in this study, within the quarter 2 survey data flown on 2/12/2018, and within the day 1 of the 3-day experiment flown on 8/15/2018 survey data both occurred with image sets from the DJI Phantom 4 Pro (see Table 1). During the quarter 2 flight on 2/12/2018 some of the GCP aerial targets were moved by beach goers which exasperated the problem. The ones moved were at the southern end of the survey near the jetty.

While a doming of the survey was present in the stages of processing before adding the ground control, the ground control remedied the problem in the parts where it was present. Unfortunately, with no ground control at the southern end of the survey the model drops significantly in elevation there. No method was found to correct this aberration in the data.

In the Phantom 4 Pro data from day one of the three-day experiment, 8/15/2018, doming was present in the model when no control was used while using the control points fixed the issue, this lead to the decision to explore methods to alleviate this problem.

4.3.3 Assessing Impacts of Flight Design and GCPs on Bowling Effect

The quarter 5 survey performed on 12/17/18 (see Table 1) was specifically designed to create a doming/bowling issue and evaluate ways to eliminate it using varying flight design and GCPs. Using the Phantom 4 Pro three missions were flown over the northern half of the study area at 40 meters Above Take Off (ATO) with an estimated GSD of 1 cm/px each at different obliquities; nadir, 10°, and 15°. An additional mission was flown over the area at 55 meters ATO with an estimated GSD of 1.25 cm/px. This was done per the recommendations in James and Robson's paper "Mitigating systematic error in topographic models derived from UAS and

ground-based image networks (James & Robson, 2014). They show that when an exact camera model is not known, the doming effect can be prevented by obtaining oblique imagery of the scene and or by flying at multiple altitudes. Both of which improve the geometry of the scene when calculating the internal camera parameters, particularly for solving the radial distortion parameters.

The processing of these data was done in three main groups based upon the incident angle of the 40-meter imagery: nadir, 10°, and 15°. Each group was processed four ways: using only the 40-meter imagery both with and without control, and then processing the 40-meter and 55-meter imagery together both with and without control.

The internal camera parameters from each process were examined and compared. Another model was then generated as a rubric. Processed using all images in the dataset, with the reason being that the more cameras that features fall within, the more information the bundle-block adjustment will have to use to solve for the camera parameters. Regardless, a comparator was needed to contrast the parameters of the twelve processes against, and a process including the total sum of images was decided to be used.

The entirety of parameters from each process was differenced to the parameter solution of the total sum process, these differences were then divided by their respective rubric parameter giving a percent difference from the rubric. A graph was made showing the results from each process of the focal length and the first radial parameter, k_1 .

4.4 Objective 2. Evaluate SfM Workflows and GIS Analyses for Change Detection

4.4.1 SfM Processing Workflows

The methods for evaluating SfM processing boil down to countless hours of use. For this study the author looked at what worked the best for work on sandy beaches. A direct software

comparison or shoot out is beyond the scope of this work but has been performed by others (Schwind, 2016). The largest concern for this study was the ability to produce noise free elevation models, and accuracy of the SfM products as residuals to check points. The author is familiar with and had access to two popular commercial software suites for SfM-MVS processing, Metashape and Pix4Dmapper. Both software are capable of generating all typical survey products including: point clouds, orthomosaics, digital elevation models (DEMs), and meshes. The workflows for the software have several differences throughout the SfM-MVS process, as described in SECTION 3.2. A discussion of the use of the separate SfM software is presented in the results section of this study. It is important to note here that Agisoft's Metashape was used for all SfM processing of the data in this study.

4.4.2 Image Altitude Rectification for UAS Equipped with Autonomous GNSS

Some consumer UASs, such as the DJI Phantom 4 Pro that is used in this study, sometimes record wildly erratic altitude values in the image geotags. This can lead to difficulty when processing the image data, particularly when locating aerial targets in the images for marking. Processing software generally has methods to increase the efficiency of locating said targets in the image set. This involves generating a sparse cloud and establishing external camera parameters and scene geometry. This allows the software to calculate the field of view of each image and determine which images contain the coordinates entered for the aerial targets. For this process to work smoothly, the image locations need to be accurate relative to the target coordinates. The erratic altitude problems mentioned can impede this process. For example, if a flight records altitudes near -55 meters but the target elevations are near 1 meter, the software will be unable to automatically determine which images should contain the aerial targets as their elevations will be well above the image locations. Typically, this is rectified by manually sorting

through the images to locate and identify the aerial targets. Fortunately, once a target is identified and located within at least two images, the software can determine which other images should contain the target. This extra step can be time consuming and confusing for the processing technician and is a potential source of error if the wrong aerial target is assigned to an entered target location. Furthermore, if the image altitude values are so far off their true altitudes, a very low vertical accuracy must be assigned to the geotags, while being the appropriate procedure in such a case it is not ideal.

A method to rectify this situation and alleviate some of the burden of aerial target identification within an image set was explored. An image was captured right before takeoff and immediately after landing, the purpose of which was to record the multirotor's elevation measurement at this point. The landing pad was also measured with the survey grade GNSS to obtain a real elevation that is aligned with all the aerial targets on the ground. The target altitude above takeoff as denoted in the flight control software was also carefully noted. Once the image set for the flight was entered into the SfM software, the geotags were exported as a .csv and brought into Excel. The altitude values from the two images taken on the landing pad before and after the flight were averaged and compared to the value recorded by the survey grade GNSS. The difference between these two values was then added to, or subtracted from, all of the flight image elevation values as appropriate. If the craft's elevation reading on the pad was lower than recorded by the GNSS, the value was added, while if it was higher, the values were subtracted. An alternative method for when images weren't taken on the landing pad, or if a survey grade GNSS isn't used, one or the other, would be to utilize the target altitude above take off from the flight controller. By averaging all the flight image altitudes, calculating the target altitude above the landing pad altitude, then applying the difference between the two as an adjustment to the

individual flight image altitudes. It is important to note that either adjustment method must be done separately for each flight or battery. As anytime the UAS is turned off then back on, it reinitializes its GNSS position and due to the low accuracies of the single frequency GNSS receiver, the initial altitude can vary a large amount between instances.

An additional problem of differentiating between flights was present as the DJI only names images 0000 – 0999. During the quarter 6 flight on 02/04/2019 (see Table 1) using the DJI Phantom 4 Pro, 1657 images were captured creating several duplicate names. When the geotags are listed in the processing software for export, there is no way to sort them by individual flight. To remedy this problem a short script was written to rename the images by flight while keeping their exif data.

The quarter 6 missions performed on 02/04/2019 using the DJI Phantom 4 pro, were used to analyze the benefit of adjusting the image altitudes. The same 1657 images were processed with their altitudes adjusted and without. The resultant check point residuals were then compared.

4.4.3 DoD Creation for GIS Analyses

A quick description of nomenclature is given here to avoid confusion when describing methods. A Digital Elevation Model (DEM) will be used when talking about any a raster whose cell values contain a number that represents a height or elevation value in a known unit. A Digital Surface Model (DSM) will be used when referring to a raster data product that represents a scene as recorded by a survey. This includes manmade objects and vegetation. If used in this paper a Digital Terrain Model (DTM) will refer to a DSM that has had terrain filtering performed showing the ground with manmade objects and vegetation removed. So, it can be considered that DSMs and DTMs are both just types of DEMs here.

4.4.3.1 DSM Differencing

A DEM of Difference (DOD) is created by taking the difference of two DEMs, each representing the area of interest at a different point in time. In this study DSMs were used. Typically, the older DSM is subtracted from the newer DSM giving positive values for elevation gain over time and negative values for elevation loss over time. Typically, rasters of equal cell size and extent are used when performing the differencing, which for UAS-SfM products mean generating the DSMs accordingly. It can be noted that most GIS software is able to perform types of interpolation when performing this operation, alleviating this need at a cost of accuracy.

4.4.3.2 Calculation of DoD Uncertainty Mask

Quantifying the uncertainty of each DSM is a necessary requisite in interpreting the DOD. As depending on a number of error sources within the survey method, in this case UAS-SfM photogrammetric surveying, the true elevation value of a DSM is equal to the raster cell value plus or minus the DSM uncertainty. (Wheaton et al., 2009) A common method for quantifying the uncertainty of a DSM is to calculate the RMSE of the Z value, of the higher order of accuracy check point residuals used in the survey (James et al., 2017). For features such as aerial targets identified in the imagery and assigned a coordinate value, the Z RMSE is stated in the processing report of the SfM software. This can be considered error in the georeferencing and SfM processing. For other methods of ground truthing, e.g., topo surveys or lidar, the residuals must be calculated by differencing the points to the DSM.

Propagating the uncertainty of the DSMs into the DOD can be performed as:

Equation 1. DOD error propagation.

$$\delta u_{DOD} = \sqrt{(\delta z_{new})^2 + (\delta z_{old})^2}$$

Where δu_{DOD} is the propagated error in the DOD, and δz_{new} and δz_{old} are the individual errors in the more recent and older DSM, respectively (Wheaton et al., 2009; Brasington et al., 2003). Once the uncertainty value is determined for a DoD each cell with an absolute value less than the uncertainty value can be masked or otherwise denoted as below the threshold of certainty. This is the method used in this study as described in the following section, however other methods exist.

Multiple methods for propagating uncertainty into a DoD exist and may be used. These methods are generally more work than the method presented above but may provide useful information. For example, Wheaton et al. (2009) outlines a method of probabilistic thresholding using a user-defined confidence interval. This method involves calculating a T-score for the cells of a DoD and then converting them to probability estimates of whether or not the change shown in the DoD is real. In the same paper Wheaton also describes an involved method of spatially variable uncertainty quantification that uses a Fuzzy inference system to assign elevation uncertainty to each cell in a DoD. A software package named GCD, that includes an add on for ArcMap GIS, has been developed based on Wheaton's methods and is available at <http://gcd.riverscapes.xyz/>. This add on has been used by the author with some success and can be used to provide particularly visually pleasing DoDs, while condensing the workflow of doing so into a few simpler steps.

4.4.3.3 Evaluation of DoD Uncertainty Mask for UAS-SfM

For evaluation of the uncertainty masking approach, UAS-SfM generated DSMs from dates 8/15/2018 – 8/17/2018 were used to create two DoDs with uncertainty masks showing the UAS survey derived change between days one and two and days two and three of the three-day experiment. The UAS used was the eBee Plus with PPK geotags using a local base station. The

DSMs were generated in Metashape from the dense point cloud via inverse distance weighting at a GSD of 2 cm.

4.4.4 Core-Envelope Surface Approach for Repeat Topographic UAS-SfM Surveys

Another approach for examining topographic change using a time series of DSMs/DEMs is referred to as core and envelope surface approach (Mitasova et al., 2011; Starek et al., 2011). The method involves using a time series of stacked DSMs from which several new rasters are created based on per-cell statistical analysis. Before creation of these products, it is necessary that the DSMs share a cell size and alignment. The new raster products generated each represent a particular statistical relationship between each cell value from the DSMs in the time series. Chosen for this study was a core raster that represents the minimum elevation/height value for that grid cell location across the time series of DSMs, an envelope raster that represents the maximum value, and a range raster that contains the maximum minus the minimum value and shows the greatest amount of change measured throughout the time series at that grid cell location. Once calculated, profiles can be taken that show each raster value along a line as a cross section. Such profiles provide insight into the dynamics of the change within the time series. Also, contours can be drawn on the core and envelope rasters that show the horizontal locations of a particular elevation over the area at its elevation minimum and maximum, for example the most seaward mean high-water location from the core and the most landward mean high-water location from the envelope.

This method was employed using quarterly surveys performed for this study from the following dates: 6/14/2018, 8/16/2018, 12/17/2018, and 2/4/2019 (see Table 1) (see Appendix 1 for flight details). The flight from the 8/16/2018 survey had the lowest residuals to its check points across the chosen surveys. Therefore, the DSMs from the other dates were reinterpolated

to align and match the cells from it. Any necessary clipping was performed to ensure that all DSMs covered the same area. The above stated rasters were generated and six profiles taken throughout the study site.

4.5 Objective 3. Evaluate UAS for Rapid Response and Monitoring

4.5.1 Rapid Processing from a Standard Flight Plan

There may arise a time in a spill situation where an orthomosaic of a sandy beach area is needed as quickly as possible for use in planning or other decision-making regarding spill response. As part of this study, an attempt to examine the rapid generation of an orthomosaic from a typical UAS mapping flight was made. Flight imagery from the 6/14/2018 collected via DJI Phantom 4 Pro flight was chosen as it covers the entire 3.2 km of the test area and was performed with a UAS similar to the DJI Mavic series platforms used by the Texas General Land Office (TGLO). The data acquisition itself was performed in three separate flights and took around an hour and fifteen minutes to complete. For complete details of the flight see Appendix 1, Section 1.1.3. Although control targets were present and surveyed, they were not used as control in this rapid processing examination. The targets were, however, identified in the imagery and utilized as check points to facilitate accuracy assessment of this process. In this manner, the flight data is a reasonable stand in for data from a real event that contains no control network.

Metashape was used for this process and the workflow was performed using the batch process GUI. The batch process workflow took about 10 minutes to set up but once created it could be reused. The only products generated were the ones necessary for orthomosaic creation, and the only products saved to disk were the orthomosaic itself and the processing report. In the processing the settings that most affect the processing time is the image scale used in feature

extraction and the density target of the dense point cloud. These were both tuned to the lowest/fastest setting possible. The processing time and check point residuals were recorded in the generated report, and the orthomosaic was saved as a file for examination.

4.5.2 Producing an Ortho from UAS Videography

An experiment of rapidly producing an orthomosaic from a UAS video flight was performed. The idea being that if time constraints were too tight to perform a proper mapping flight, that a video recording of the subject area could be used to generate an orthomosaic. Being a 2D image file, the orthomosaic may be easier to share quickly, and take precursory measurements from, as opposed to just viewing and sharing the video itself. The video used was taken on 12/17/2018 with the DJI Phantom 4 Pro (see Table 1), covered the entire 3.2 km of the test area and took about ten minutes to perform. The flight was flown manually, without the use of any auto pilot or flight control software. The flight path was determined in real time by observing the camera feed and keeping the appropriate scene in frame. This was done by launching from the ground control station in the center of the test area, flying to the North end, then to the South end and back to the launch site. On the North bound legs of the flight the UAS was kept more toward the water side of the beach, while on the South bound leg the UAS was kept toward the dune side of the beach. When flying both directions the entire beach was kept in frame. This was done to create stereo overlap of captured areas. This could be done by someone not familiar with flight control software necessary for performing mapping flights.

The processing was performed in Metashape. The video was filmed at 30 frames per second in 4K resolution. Still images were extracted from every 30th frame of the video giving 565 images. The end lap is estimated to be about 90% and the side lap varying from 50% to

70%, the speed of the craft was near 10 m/s for the majority of the flight. A flight path generated from the UAS's log is shown in Figure 15.



Figure 15. Oblique view of video flight path.

4.5.3 Video Documentation of Spills

The quarter 5 field day of 12/17/2018 (see Table 1) saw the recording of a video to document the study area. With the idea that the video file could be shared with decision makers for them to view, as opposed to generating an orthomosaic as discussed in the previous section. The entire 3.2 km was videoed in about ten minutes. A UAS with video capabilities is necessary for this task, as the commercial mapping UASs used in this study are not designed to or capable of easily capturing video footage of an area. Using the DJI Phantom 4 Pro, the desired video settings were selected, utilizing the highest resolution to capture the most detail. Then the UAS

was brought to an altitude that brought the width of the beach into frame. The pilot started recording and flew up and down the beach while a visual observer kept watch on the UAS. The pilot used a tablet attached to the remote controller to keep a constant view of what the camera was seeing and thereby kept the area of interest in frame. When the beach was documented the UAS was landed.

4.6 Objective 4. Guidelines for Surveying of Spill Events on Sandy Beaches with UAS

Based on the UAS surveys and field experiments conducted in this work, as well as data processing investigations, the fourth objective of this thesis is the compilation of a set of guidelines for surveying of oil spill events on sandy beaches with UAS for delivery to the TGLO. The document provides an overview on UAS and discusses in detail equipment considerations, mission considerations, such as weather, mission planning and execution, and data processing, and other uses of UAS for oil spill response. The citation of the work is provided here:

Starek, M.J., Berryhill, J.B., (2020). Guidelines and considerations for Surveying of Oil spill Events on Sandy Beaches with UAS. (TGLO Technical Report, Contract No. 18-140-000-A683)

The document's cover sheet is included in Appendix 2 and the report is available for review online or by request to the authors or TGLO.

CHAPTER V:

Results and Discussion

5.1 UAS-SfM Vertical Accuracy and Change Detection Error

5.1.1 Assessment of Control Network Geometry and Image Location Accuracy

As discussed in Section 4.3, multiple processing runs were completed using different amounts of control with both differentially corrected GNSS, in this case PPK, and autonomous GNSS collected during the three-day field experiment. Using the eBee Plus, these tests utilized the same images, the same image coordinates for the GCP/checkpoint locations, and the same processing settings. This was a test of GCP geometry/amount and image location accuracy. The same ten check points were used to measure residuals in all processing runs. A graph of these results from 8/16/2018 field data is shown in Figure 16 below.

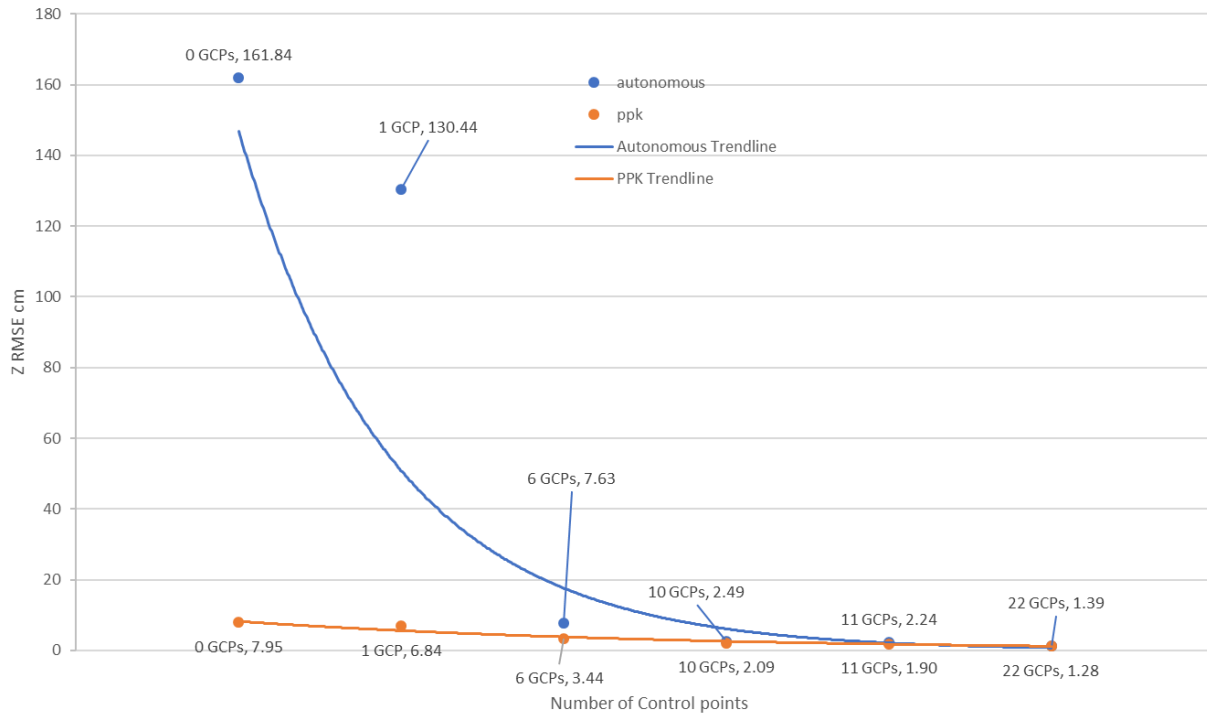


Figure 16. Graph of Z residuals on same 10 check points resulting from separate processing runs utilizing different control geometries, shown in section 4.2.2.4, and image location accuracies PPK vs. Autonomous. Flights were performed with the eBee Plus on 8/16/2018.

The number of GCPs used here is not a hard-fast rule for every situation and may be misleading. The different number of control targets utilized are more representative of control network strength with six being weak, ten and eleven being normal or reasonable, and twenty-two being rigorous. The amount and geometry of GCPs used for any given survey is dependent on the shape of the subject area, with equal interval pairs appearing to be best practice for linear stretches of sandy beach. Best practices recommend not exceeding roughly 300 meters between GCPs in a survey (Starek et al., 2020).

It can be seen that when using autonomous GNSS for image locations that the resultant survey is highly dependent on accurate control for achieving reasonable accuracies. It may be concluded that when rigorous control is being used that the addition of differentially corrected GNSS may not add significantly to the quality of survey results, and therefore may not be worth the extra effort or cost.

It can also be seen that when using PPK differentially corrected GNSS for image locations that the resultant survey can produce survey data with reasonable accuracies with little to no control present, based on the UAS platform, camera, and SfM processing workflow tested. If such accuracies are acceptable, much time and labor may be saved when performing the field work using PPK based approaches for correction of UAS image geotags.

5.1.2 Assessment of UAS-SfM DSMs Relative to TLS DSMs

Described in Section 4.2.2, the phase of this study referred to as the three-day experiment yielded copious amounts of data among which is three separate TLS-derived DSMs of a portion of the study site across the three days of the experiment. The measured TLS point clouds were filtered then used to interpolate DSMs via LAStools. They were generated with the same 2 cm cell size as the DSMs derived from the eBee Plus PPK/RTK. The projected coordinate system

used was NAD83(2011) / UTM zone 14N (EPSG::6343) all elevations were relative to the ellipsoid. The intended use of the TLS DSMs was for comparison via DoDs to the UAS-SfM derived DSMs. The UAS data set chosen for this comparison from each day was the eBee Plus PPK/RTK image set utilizing the PPK derived image locations and 22 GCPs. This data set was chosen as it presented the lowest check point residuals and represents the highest accuracy UAS work achieved during this study.

When examining the datasets for analysis, the DSM products were first used to produce DoDs between days and the same survey methods; yielding two TLS derived DoDs: day 3 minus day 2, and day 2 minus day 1; and also yielding two UAS-SfM DoDs: day 3 minus day 2, and day 2 minus day 1. This was done to check the consistency of the data before comparative analysis and ensure that the surveys were congruent to themselves. Outlier values in both the DSMs and DoDs represented a small portion of the data sets, at worse 0.1% for the TLS DoDs, as such the DoDs and DSMs are all visualized using a percent clip linear stretch set to 0.1% for both the minimums and maximums. All rasters used in this phase of analysis have a working cell size of 24,854,231 cells. The DoD rasters were converted to ascii format, and a python script was written to calculate mean, minimum, maximum, standard deviation, and RMSE. The resultant DSMs (Figure 17, Figure 18, and Figure 19) and DoDs (Figure 20 and Figure 21) for the TLS surveys are shown below.

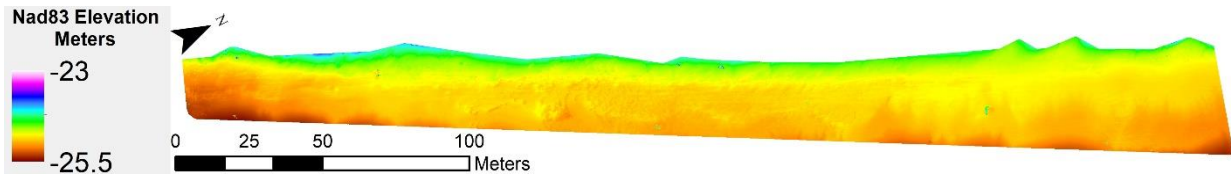


Figure 17. Day 1 TLS derived DSM.

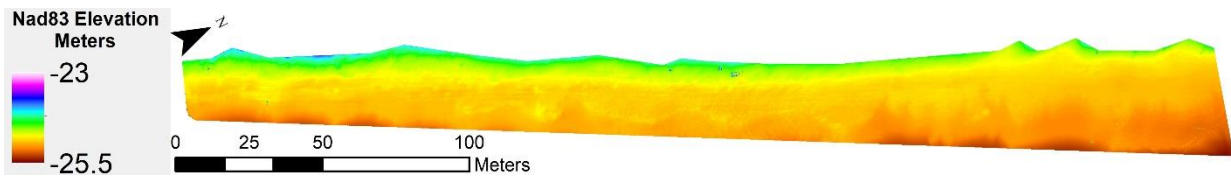


Figure 18. Day 2 TLS derived DSM.

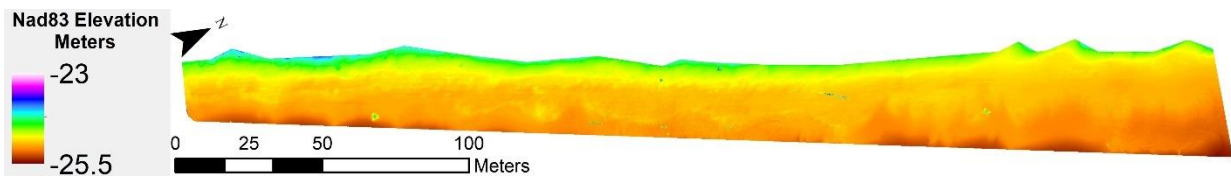


Figure 19. Day 3 TLS derived DSM.

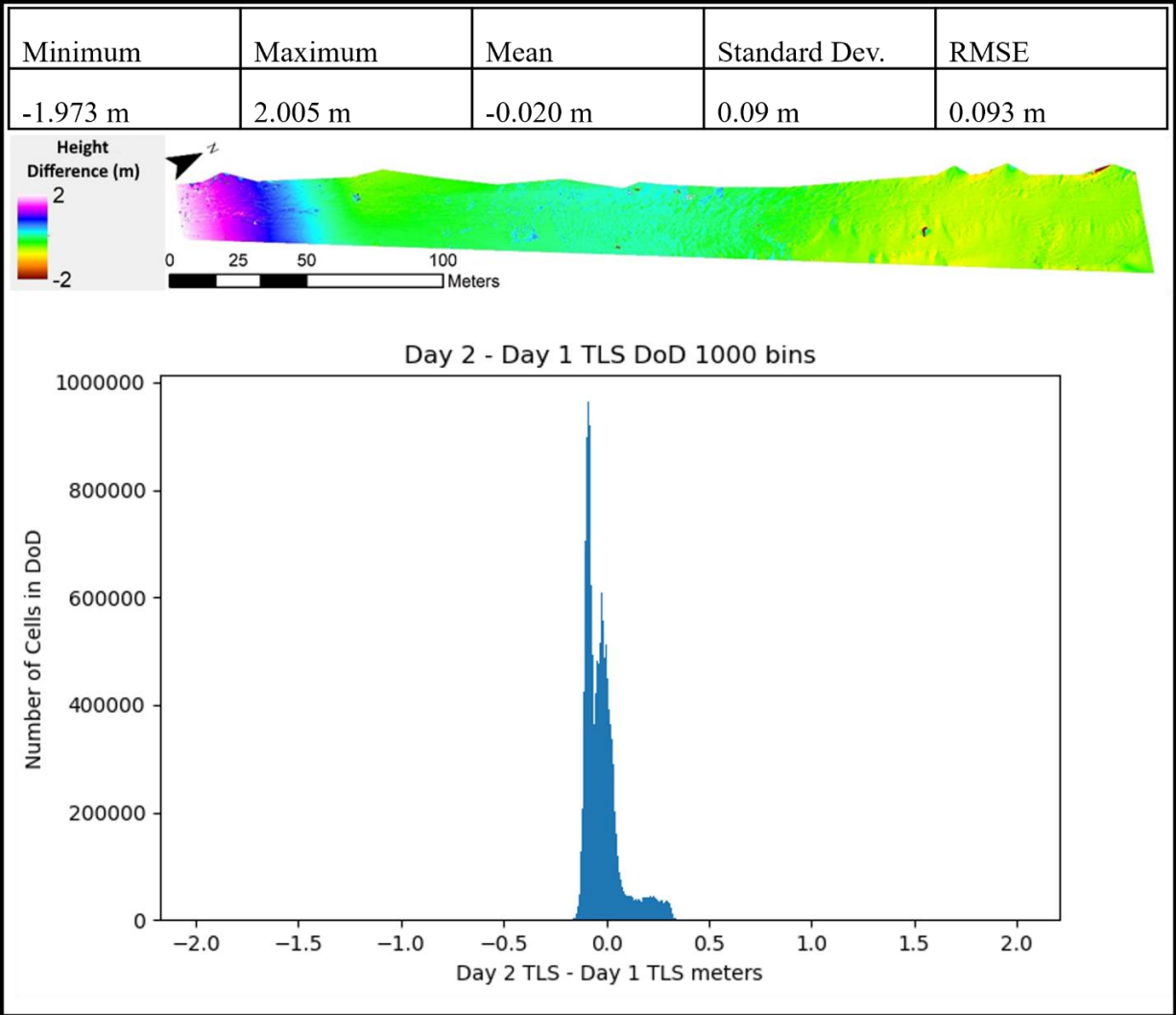


Figure 20. Day 2 TLS -Day 1 TLS DoD, statistics, and histogram.

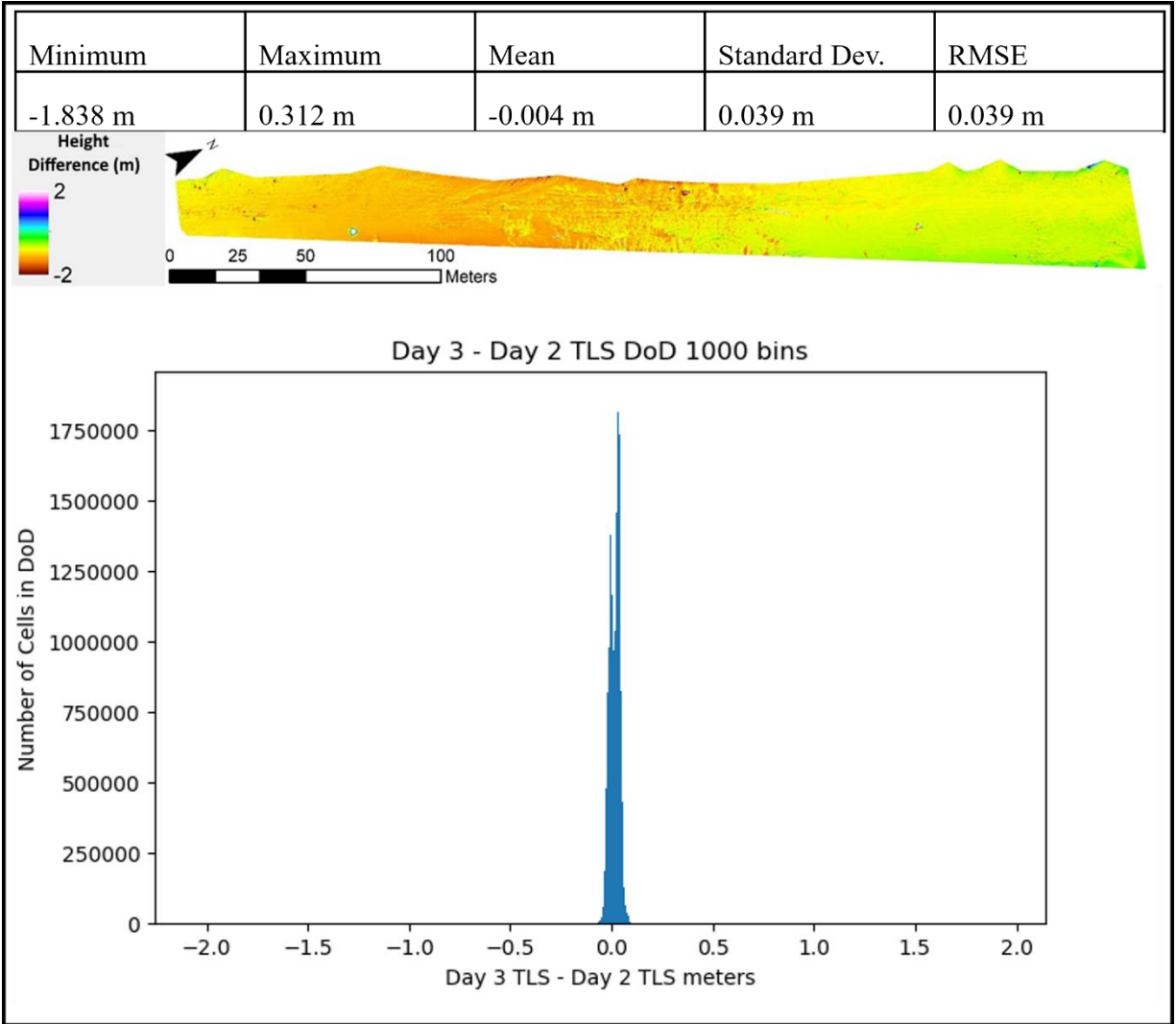


Figure 21. Day 3 TLS -Day 2 TLS DoD, statistics, and histogram.

Referring to figures above, there are clearly georeferencing issues with the TLS surveys, especially in the day 1 data set. While the difference between day 3 and day 2 does show a tilt in one of the day’s scan positions, it is of a small magnitude and is magnified by the contrast stretch in the display symbology; the mean, and vertical RMSE indicate that the two surveys are very close to each other. The 3.9 cm RMSE is a reasonable number given the numerous tire tracks and other environmental changes of the sand over roughly 24 hours. However, the drop in elevation at the Southern end of the study site in the day 1 DSM, and the 9.3 cm vertical RMSE between

days 2 and 1 lead the author to believe that more serious problems were present during the day 1 TLS survey. The individual scans per day utilized numerous canister targets to determine the attitude and location of the scanner. Errors in the GNSS measurements on these targets could lead to tilts in the point clouds as seen above. Other causes could be unstable tripods under the targets or scanner, cloud registration errors, and/or user error. The author thought it prudent to investigate if any such daily biases were present in the UAS-SfM derived surface models. UAS-SfM DSMs with a GSD of 2 cm (see Figure 22, Figure 23, and Figure 24) and DoDs (Figure 25 and Figure 26) were generated between consecutive days for the UAS surveys as described above, are shown below.

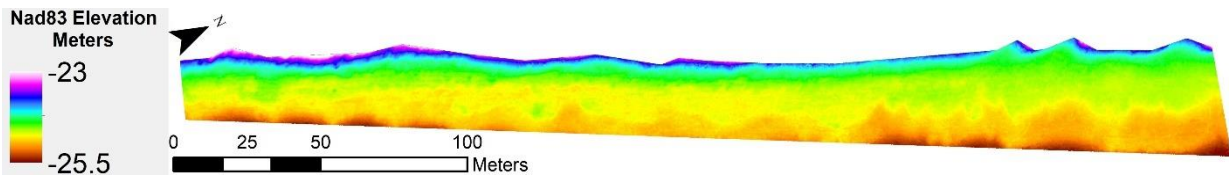


Figure 22. Day 1 UAS derived DSM.

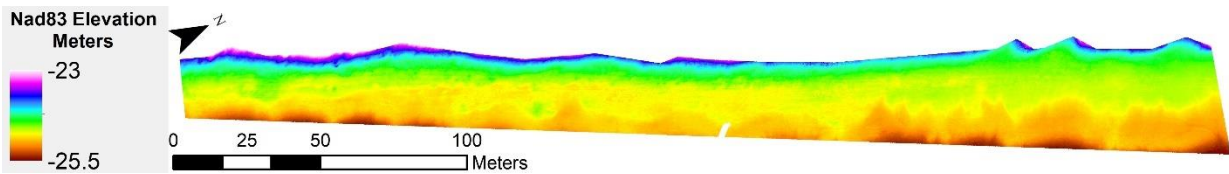


Figure 23. Day 2 UAS derived DSM.

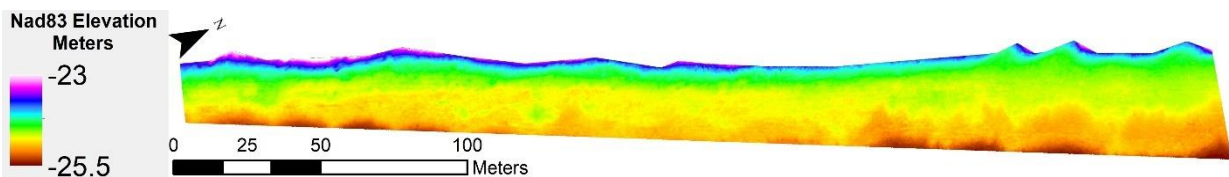


Figure 24. Day 3 UAS derived DSM.

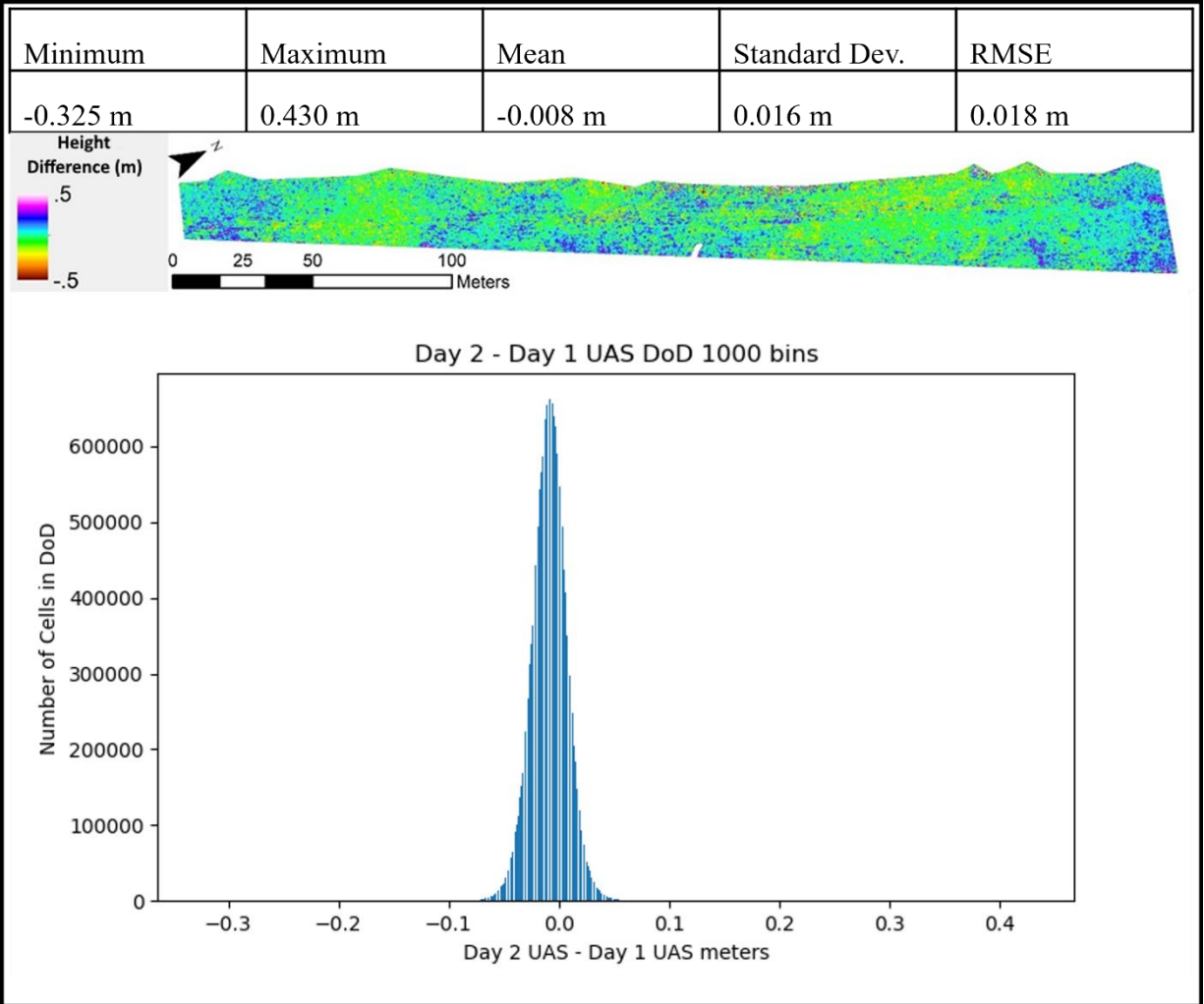


Figure 25. Day 2 UAS - Day 1 UAS DoD, statistics, and histogram.

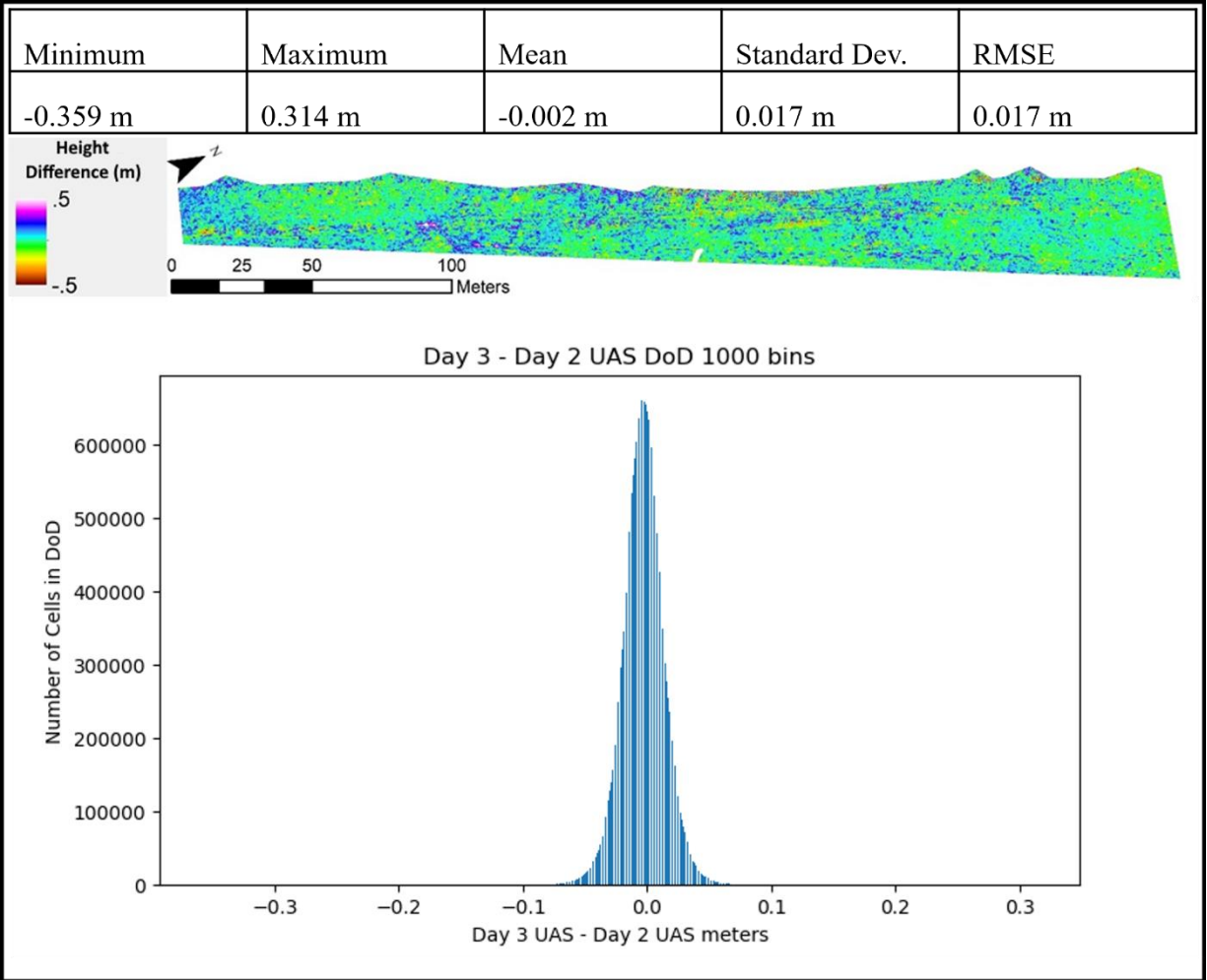


Figure 26. Day 3 UAS - Day 2 UAS DoD, statistics, and histogram.

There is not a significant surface bias present in the UAS-SfM data as seen in the TLS data. The RMSE of the UAS-SfM DoDs is under 2 cm showing a greater consistency in their georeferencing from day to day. The comparison between the UAS and the TLS data is shown below as DoDs from each day and was created by subtracting the TLS data from the UAS data.

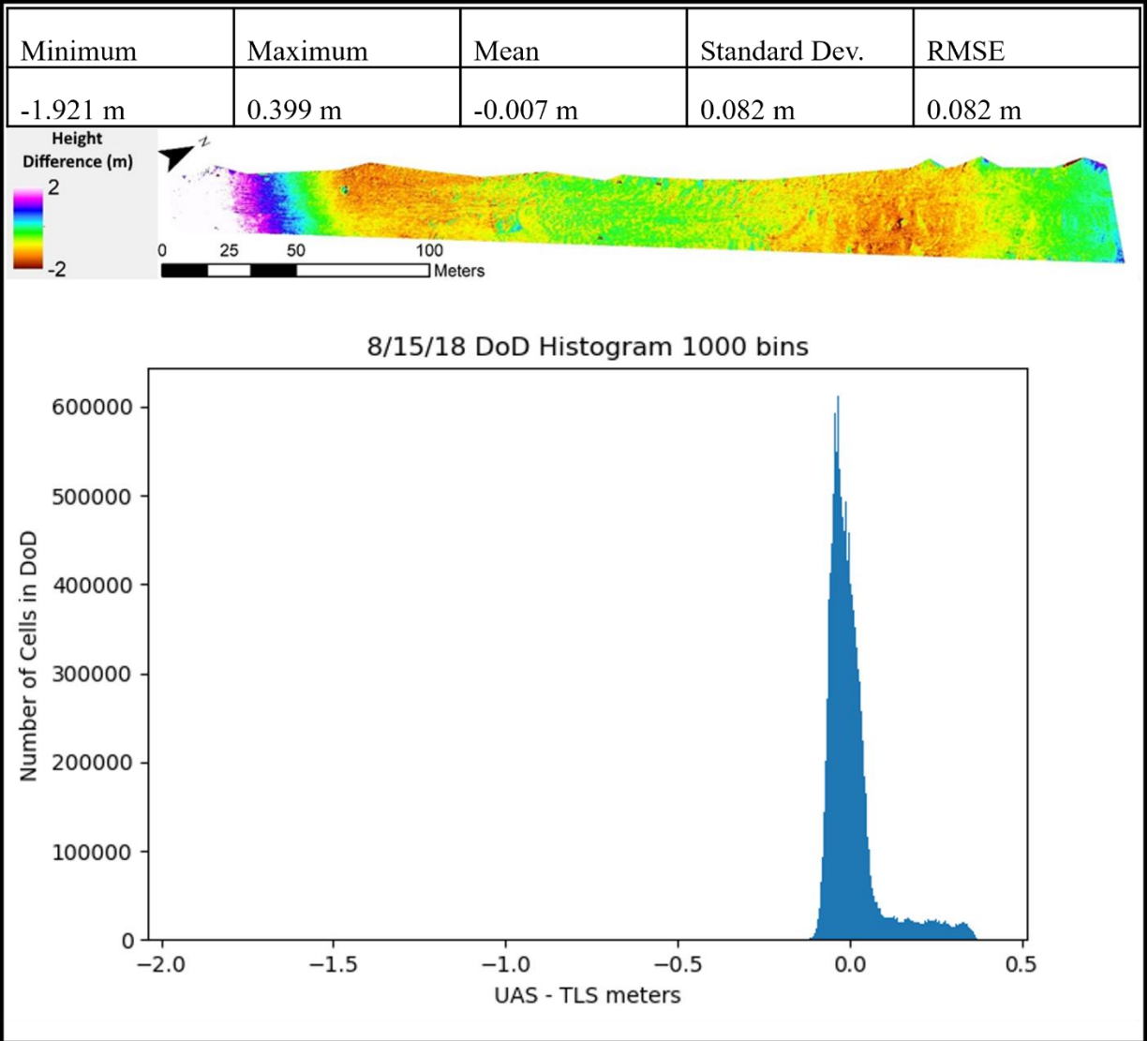


Figure 27. Day 1 UAS - TLS DoD, statistics, and histogram.

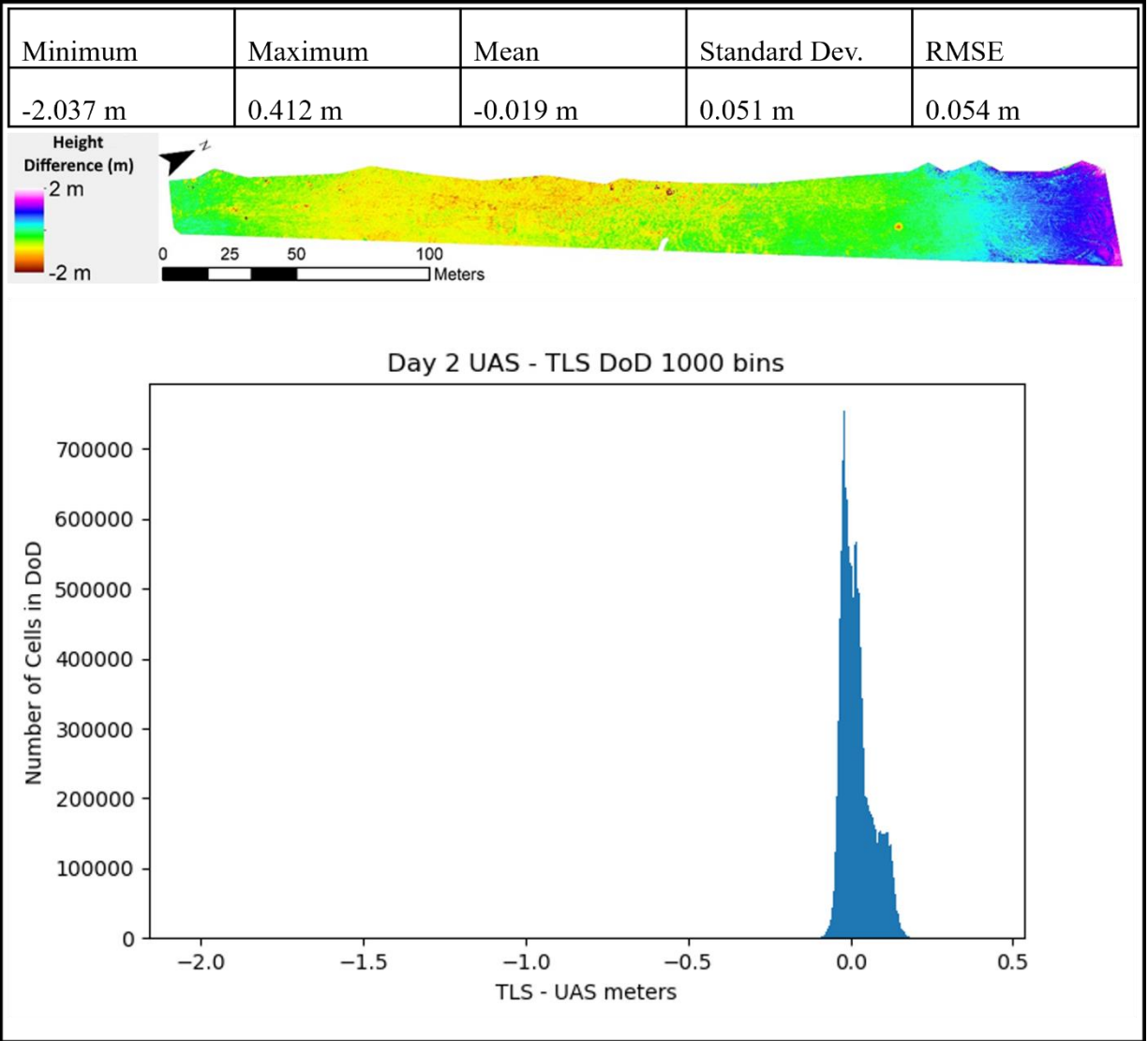


Figure 28. Day 2 UAS - TLS DoD, statistics, and histogram.

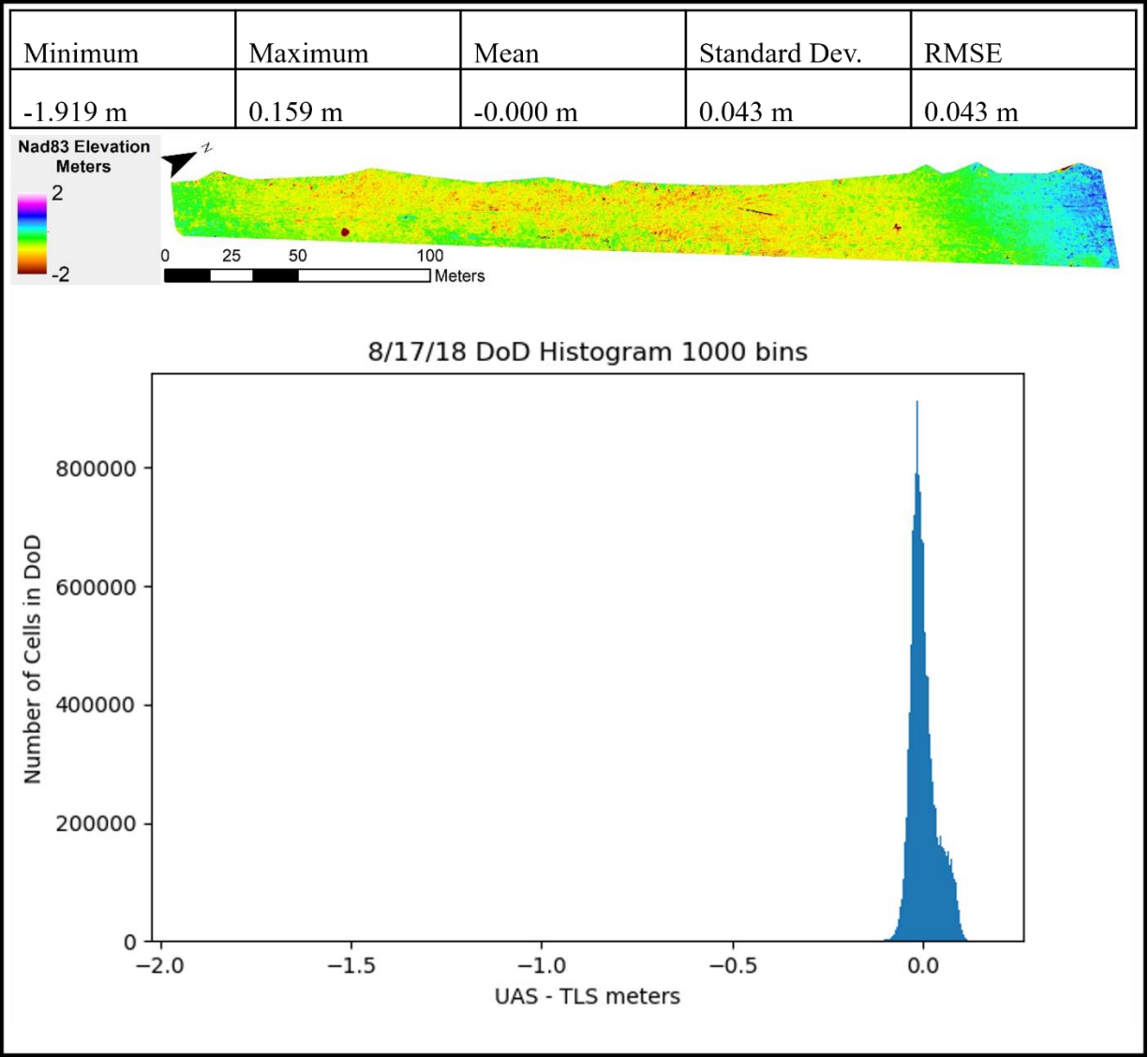


Figure 29. Day 3 UAS - TLS DoD, statistics, and histogram.

If one assumes that the UAS-SfM DSMs are uniform in elevation consistency, as their DoDs suggest, the apparent tilt within the TLS data becomes visible. The tilt is more pronounced on day one and improves for day two and three. The uncertainty of the elevation consistency of the TLS-derived DSMs based on the DoDs, leads this author to conclude that, for this case study, variability in scan registration and georeferencing potentially resulted in minor, systematic tilts in the TLS data. As such, caution must be taken when employing the TLS data as a ground truth for judging the accuracy of the UAS-SfM DSMs in this case study.

5.1.3 Assessment of UAS-SfM relative to RTK GNSS Check Points

The Z residuals of the check points from the Metashape processing reports for each of the UAS-SfM eBee Plus surveys discussed above are shown in the tables below.

Table 2. Day 1 Check Point Residuals from the Metashape processing report.

Count	X error (cm)	Y error (cm)	Z error (cm)	XY error (cm)	Total (cm)
10	1.4	1.2	1.6	1.8	2.4

Table 3. Day 2 Check Point Residuals from the Metashape processing report.

Count	X error (cm)	Y error (cm)	Z error (cm)	XY error (cm)	Total (cm)
10	1.4	1.1	1.2	1.8	2.2

Table 4. Day 3 Check Point Residuals from the Metashape processing report.

Count	X error (cm)	Y error (cm)	Z error (cm)	XY error (cm)	Total (cm)
10	1.0	1.4	3.9	1.8	4.3

As can be seen, even with the visible errors in the lidar data, the differences between the Z residuals from the UAS minus TLS DoDs and the Z residuals in the check points from the Metashape processing report are within 10 cm of each other, with day one being 8.2 cm lidar and 1.6cm check points, day two being 5.4 cm lidar and 1.2 cm check points, and day three being 4.3 cm lidar and 3.9 cm check points.

5.1.4 Assessment of UAS-SfM DSM Relative to RTK GNSS Topo Transects

As described in Section 4.2.1., during the quarter 6 survey on 2/4/2019, in which the Phantom 4 Pro was flown due to weather conditions, a group of undergraduate students were able to perform some topo surveying of the beach at the time of the flight. They collected 264 points and labeled with a descriptor of either NG for natural ground or Veg for vegetation.

Twenty-six aerial targets were also used for SfM in Metashape processing allowing for 10 control targets and 16 check points. As stated in the flight description, a sea fog was present during the flight significantly limiting visibility. This likely contributed to worse than normal internal calibration parameters and lead to poorer than normal residuals. The residuals for the control points and check points from the Metashape processing report are shown below in Table 5 and Table 6.

Table 5. Control Point RMSE for 02/04/2019 DJI Phantom 4 Pro Flight

Count	X error (cm)	Y error (cm)	Z error (cm)	XY error (cm)	Total 3d (cm)
10	1.9	2.1	5.5	2.9	6.2

Table 6. Check Point RMSE for 02/04/2019 DJI Phantom 4 Pro Flight

Count	X error (cm)	Y error (cm)	Z error (cm)	XY error (cm)	Total 3d (cm)
16	2.0	2.5	12.4	3.2	12.8

The 12.5 cm RMSE in Z on the check points is higher than expected and higher than most previous and subsequent flights with the particular UAS. These results are comparable to the topo points differenced to the Metashape generated DSM as shown in below (see Figure 30 and Figure 31). It is notable that the residuals are better near the center of the beach and worse towards the water and in the dunes and vegetation. There is possible sinkage of the survey pole in the sand lending to discrepancies from the UAS data, and the data is expected to be lower in the vegetation where the topo point is measured on the ground and the UAS DSM is measuring to the top of the vegetation. This being said, it appears that a warpage on the order of 10 cm is present throughout the DSM against both the topo points and the aerial target check points.

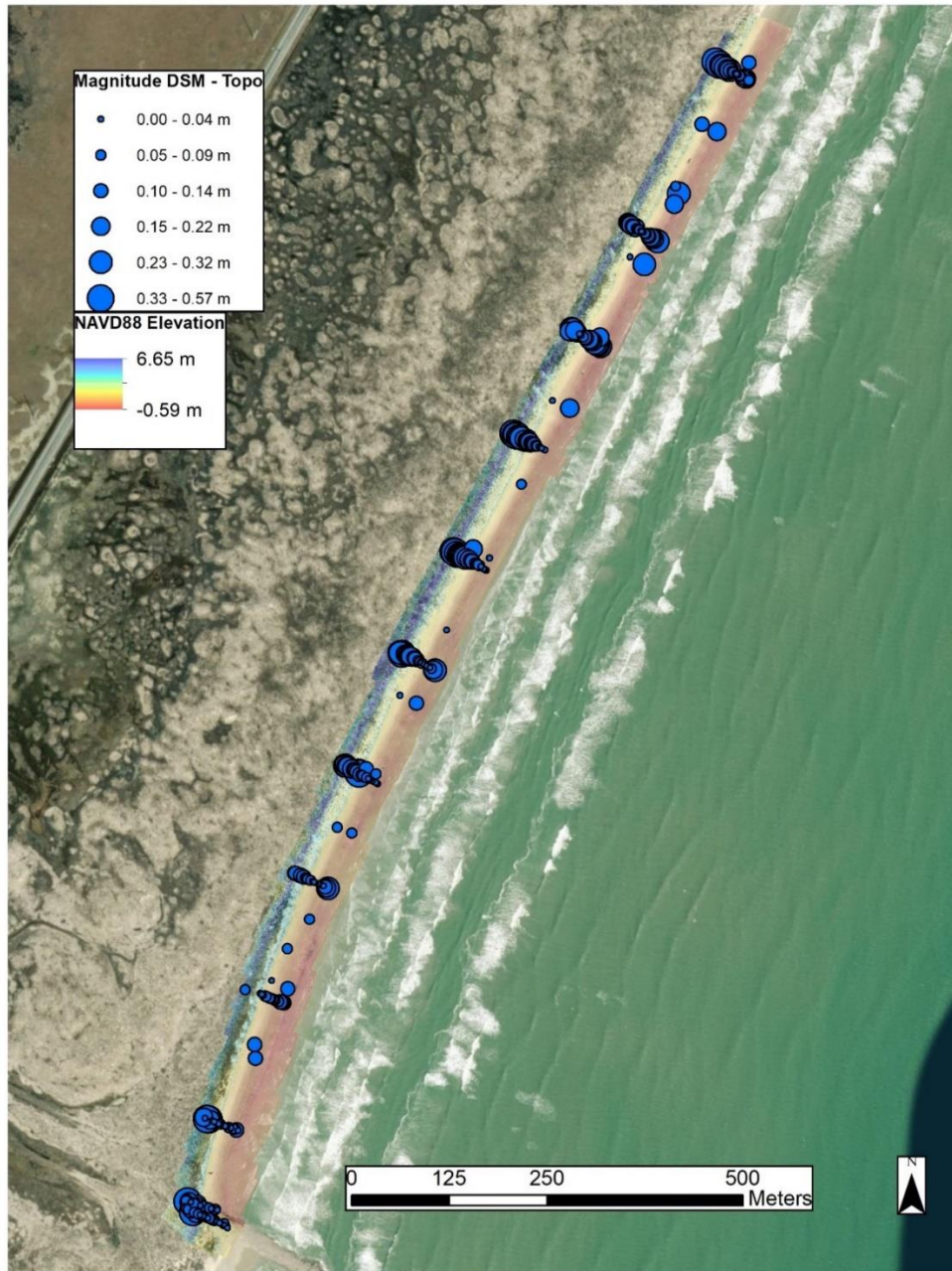


Figure 30. Metashape generated DSM, and Orthomosaic over base map of 02/04/2019 Phantom 4 Pro Beach Survey with proportional symbols of absolute value of topo point residual.



Figure 31. View of single transect from 02/04/2019 beach survey with DSM, hill shade, orthomosaic, and proportional symbols of absolute value of topo point residual.

Table 7. Statistics for the two classes of topo points and of all points from DSM value minus topo point value.

<i>Units = Centimeters</i>	All Points	Natural Ground	Vegetation
RMSE	10.5	10.5	22.8
Mean	6.5	10.1	18.6
Min	-30.3	-30.3	-10.5
Max	56.6	24.9	56.6

5.1.5 Best achieved Accuracy from Field Campaigns

The best achieved accuracies throughout the entire study period based on the set of UAS surveys occurred on 08/16/2018, day 2 of the 3-day (see Table 1) experiment while utilizing PPK differential image locations, a very rigorous control network and the eBee Plus UAS. The accuracy assessment is based on the residuals to check points given in the Metashape processing report. The aerial targets were surveyed using the survey grade GNSS equipment utilizing RTK from the local base station. The static observations from the said base station were used for the PPK processing of the image locations. The same survey and processing methods were also used

on days 1 and 3 of the 3-day experiment, yet they yielded slightly higher residuals (see Table 2, Table 3, and Table 4).

5.1.6 PPK vs. Autonomous GNSS Onboard UAS with Control

As shown in Section 5.1.1., using PPK differential GNSS image locations results in superior accuracies when using minimal to no control network over autonomous GNSS image locations. This would allow much less labor in the field if accuracies of this order are acceptable, as setting up a base station and surveying only a few targets is significantly less work than laying out even a minimally rigorous control network. However, if the highest accuracies possible are the goal, then the combination of PPK differential GNSS image locations and a rigorous control network are shown to be slightly better than autonomous GNSS image locations and a rigorous control network. If initial cost is a large limiting factor and rigorous control networks are planned to be used, the advantage of PPK differential GNSS image locations over autonomous is minute.

As shown in Section 5.1.1., the sweet spot for labor vs. accuracy when utilizing PPK differential image locations is when using a minimally rigorous control network, in the case of this study on a sandy beach survey 3.5 km in length, this involved three pairs of targets, one pair at each end of the beach and one pair near the center.

5.1.7 Example of UAS-SfM Change Detection Uncertainty with DoDs

In Section 4.4.3.2, error masking for DoDs was discussed. Such masks are applied here to the UAS DoDs, with a 2 cm GSD, derived from the three-day experiment eBee Plus data shown in Section 5.1.1. (see Figure 25 and Figure 26). Using the formula:

Equation 1. DOD error propagation.

$$\delta u_{DOD} = \sqrt{(\delta z_{new})^2 + (\delta z_{old})^2}$$

with the check point Z residual values shown in Table 2, Table 3, and Table 4 being 1.62 cm, 1.28 cm, and 3.98 cm for UAS-SfM DSMs from days 1, 2 and 3 of the 3-day field experiment, respectively.

Portions of the DoDs within the range of propagated uncertainty are masked out of the rasters in Figure 32 and Figure 33. It should be noted that no vehicles or manmade objects were present in the scenes during the surveys, therefore filtering out of such objects was not necessary in this case. If a vehicle or some other large object was present in one survey but not the other a large change would be present at its location. Since the surveys were performed on consecutive days and no major weather events took place between them the change to the section of beach was minimal. This shows that to detect small levels of elevation change between survey dates georeferencing of the data is paramount. Using methods such as a rigorous GCP network and additionally differentially corrected image locations if available, are necessary to achieve low residuals to check points. Check points of a higher order must be present to quantify the uncertainty of a survey in the first place. This may not always be feasible during time critical surveys for beach oiling and is a major consideration when employing this method. However, the method provides valuable information about the reliability of the change detected, and if employed could be useful in prioritizing the search for buried oiling after a major weather event impacts a spill cleanup in progress.

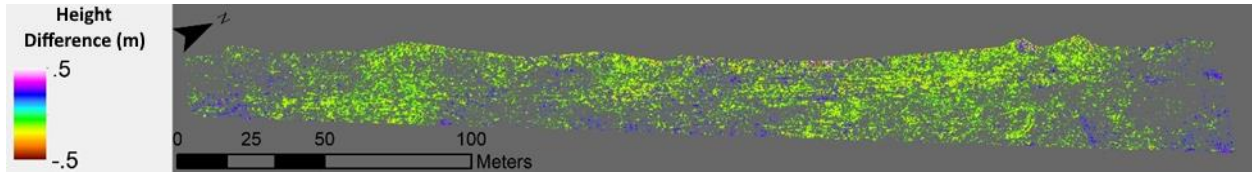


Figure 32. Day 2 minus day 1 DSM masked for values between -2.06 cm and 2.06 cm.

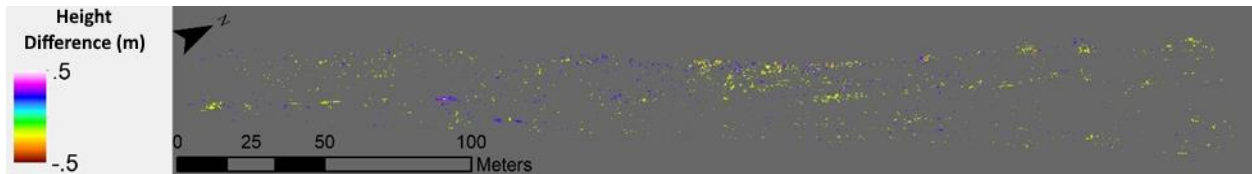


Figure 33. Day 3 minus day 2 DSM masked for values between -4.18 cm and 4.18 cm.

5.2 Core-Envelope Results

A time series of quarterly surveys from this study were used to generate a core-envelope data set. Quarters 3, 4, 5 and 6 flown on 6/14/2018, 8/16/2018, 12/17/2018, and 2/4/2019 were chosen for this while quarters 1 and 2 were left out due to their georeferencing problems. The survey data chosen was flown by both the eBee plus and the Phantom 4 Pro, yielding DSMs of various GSD. The 4th quarter flight, which was part of the 3-day experiment, was chosen as the standard with which to align and resample the other data sets to due to it having the lowest check point residuals. Once the data sets had a common cell size and alignment, three new rasters were generated from them. The core raster contains the minimum value for a given cell across the four data sets. The envelope raster contains the maximum value for a given cell across the four data sets. The range raster contains the value of maximum raster minus the minimum raster, showing the greatest amount of change for each cell throughout the time series. Profiles were taken from the core, envelope, and all four survey DSMs. These profiles were then graphed together while their horizontal location was shown upon both an orthomosaic of the area for reference and upon the range raster to help visualize the areas of the beach that showed the most change across the

dataset. This core-envelope technique is presented in this study as it has potential for understanding beach sediment migration during a long-term oiling cleanup effort.

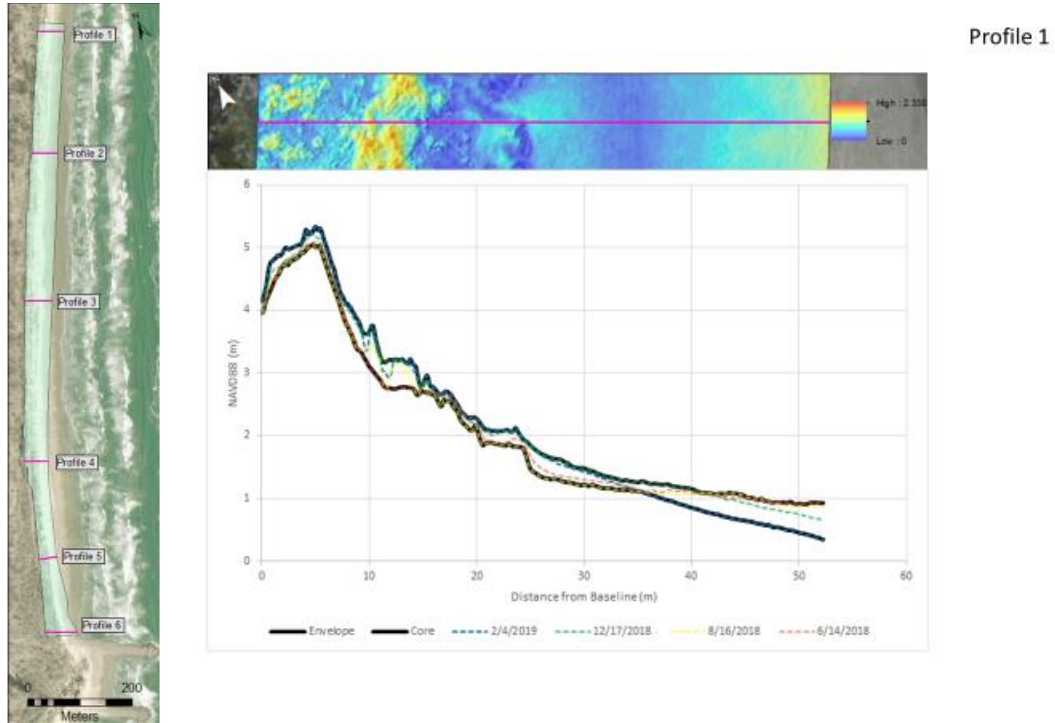
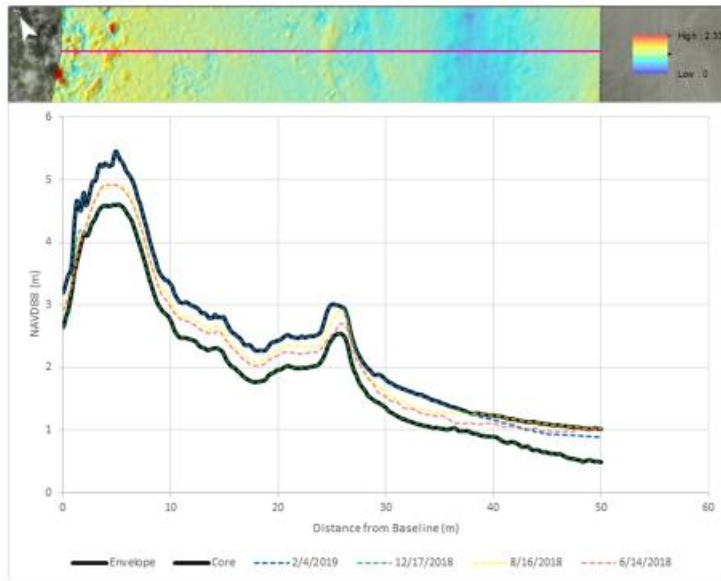
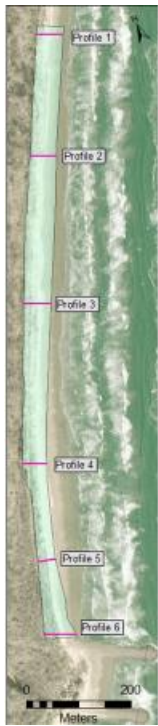
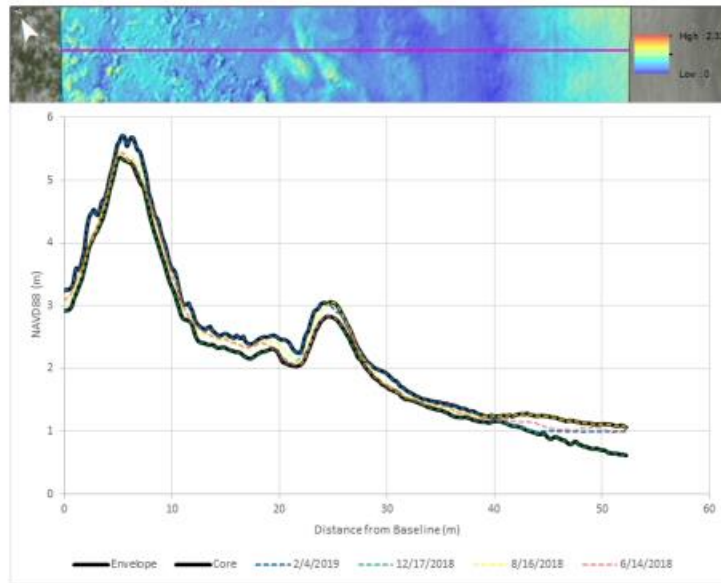
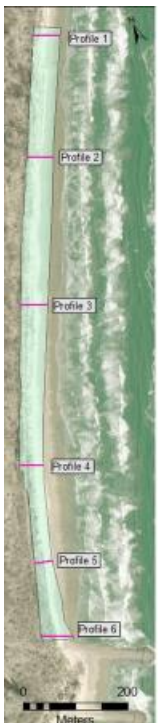


Figure 34. Core-Envelope profile 1.



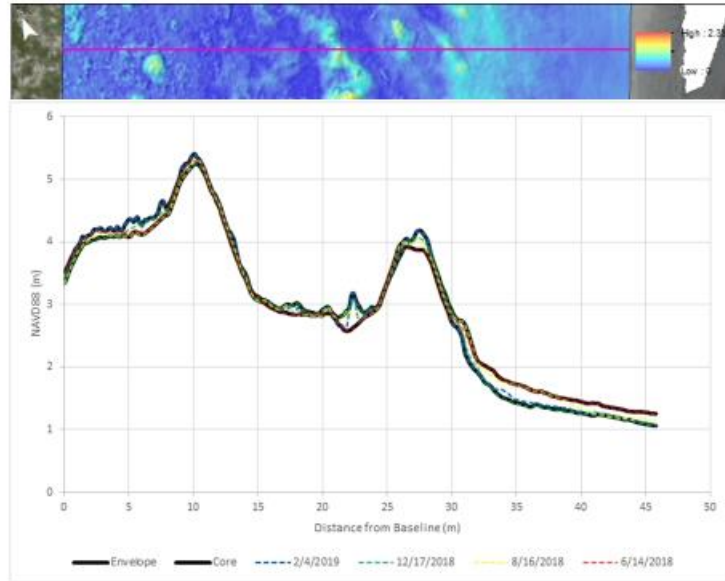
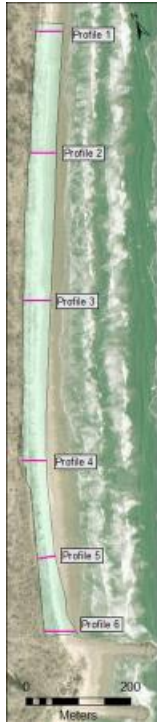
Profile 2

Figure 35. Core-Envelope profile 2.



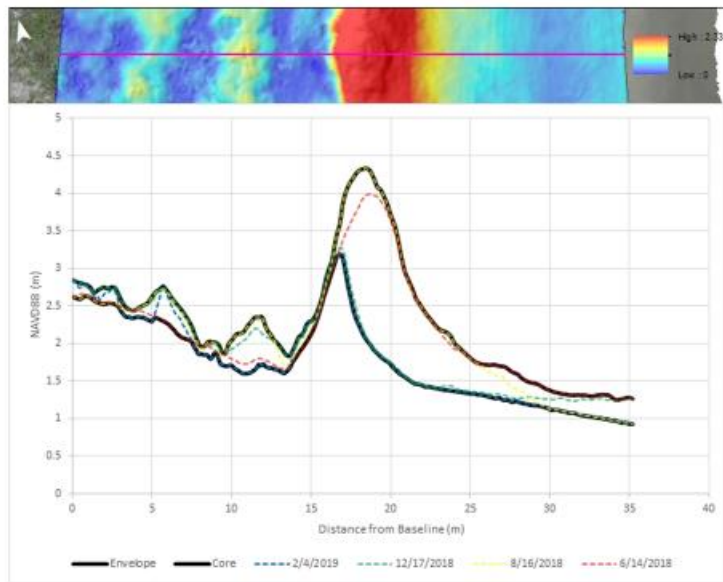
Profile 3

Figure 36. Core-Envelope profile 3.



Profile 4

Figure 37. Core-Envelope profile 4.



Profile 5

Figure 38. Core-Envelope profile 5.

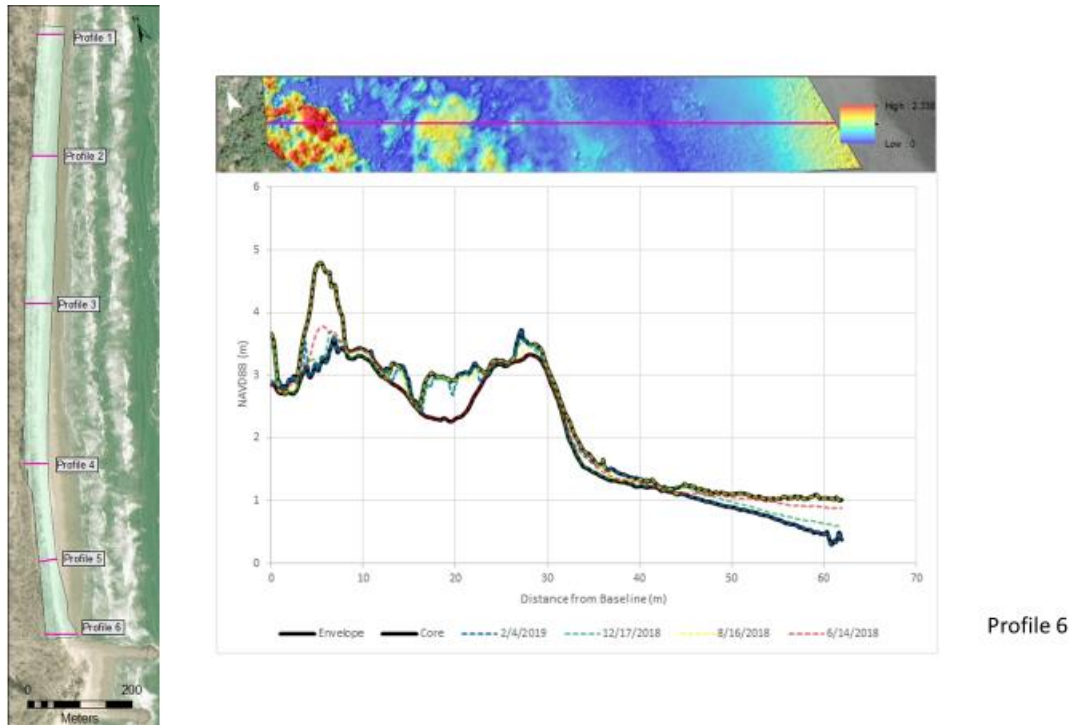


Figure 39. Core-Envelope profile 6.

5.3 Flight Design Impacts for Reducing Bowling Effect

5.3.1 Multi-Altitude Flights and Oblique Imagery

As described in Section 4.3.2, the Q5 12/17/2018 survey included flights with the DJI Phantom 4 pro designed to induce the bowling effect and flights designed to mitigate it. The premise being that single altitude flights with parallel nadir images exasperates the camera calibration errors that lead to the bowling effect and that utilizing multi-altitude image sets or non-parallel oblique images reduces such errors.

A visual comparison of the finished point clouds and external camera orientations/locations show a significant amount of doming in the model generated from the 40-meter nadir imagery with no control used. All other models showed no visual signs of doming/bowling. The following Figures 40 through 51 are screen shots of the sparse point clouds and image locations described in Section 4.3.2. They show that the doming effect was apparent

only in the process run that included the 40-meter ATO nadir images with no GCPs used but, when multi altitude, non-parallel oblique image sets, or an adequate GCP network were used, the bowling problem was resolved.



Figure 40. Nadir 40-meter imagery with no control.

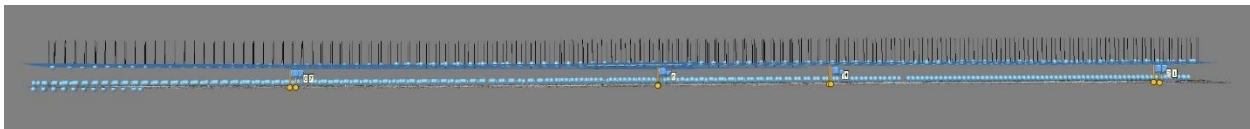


Figure 41. Nadir 40-meter imagery with control.

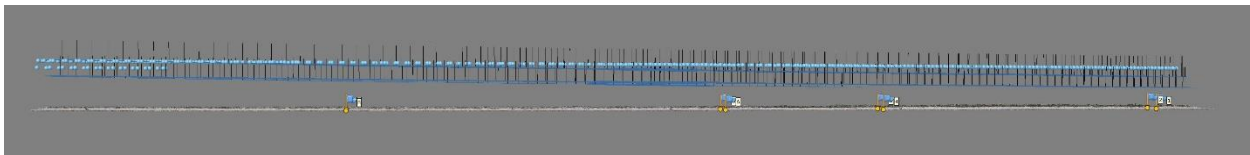


Figure 42. Nadir 40-meter and 55-meter imagery with no control.

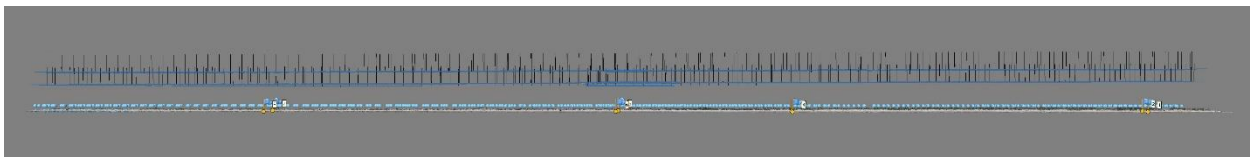


Figure 43. Nadir 40-meter and 55-meter imagery with control.

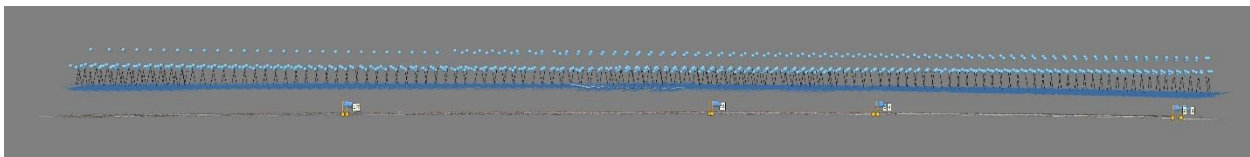


Figure 44. 10° 40-meter imagery with no control.

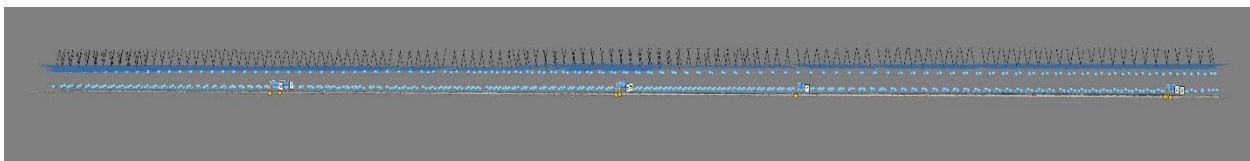


Figure 45. 10° 40-meter imagery with control.

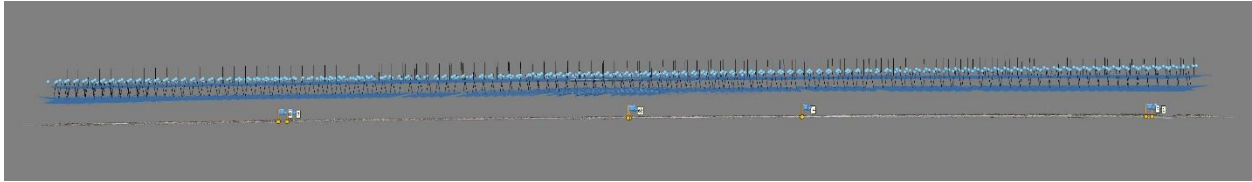


Figure 46. 10° 40-meter and 55-meter imagery with no control.

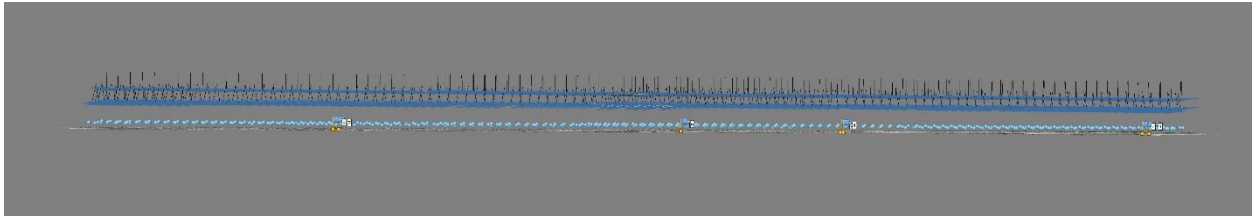


Figure 47. 10° 40-meter and 55-meter imagery with control.

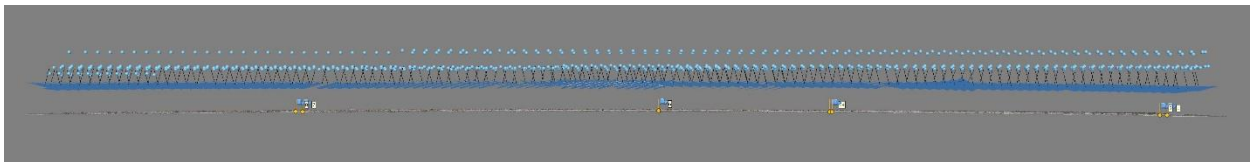


Figure 48. 15° 40-meter imagery with no control.

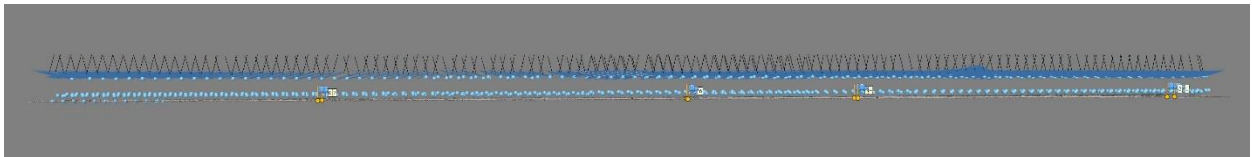


Figure 49. 15° 40-meter imagery with control.

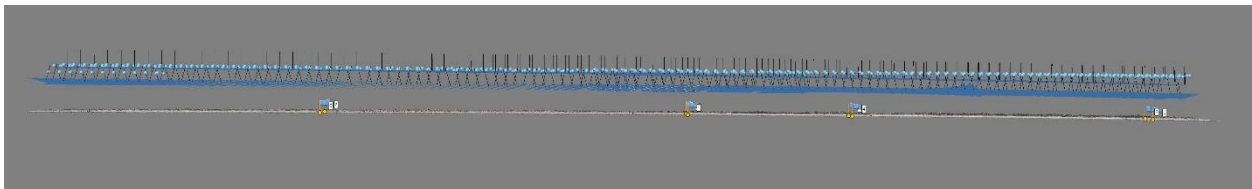


Figure 50. 15° 40-meter and 55-meter imagery with no control.

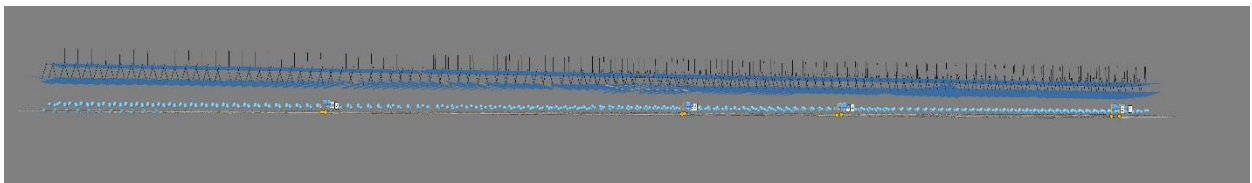


Figure 51. 15° 40-meter and 55-meter imagery with control.

A graph and table were created showing two of the internal camera parameter solutions of the above processes, the first radial parameter, $K1$, and the focal length (see Figure 52.). It was found that the first radial distortion parameter, $K1$, in the model with doming present, nadir with no control, deviated significantly from the range of all other models. This falls in line with the conclusions of James et al. (2014), Wu (2014), and Tournadre et al. (2015) that data sets of parallel images and low numbers of strong features can suffer from the bowing/doming effects of inaccurate radial parameter solutions (see Figure 40). In this case, inclusion of GCPs was able to rectify the problem although the $K1$ parameter of the process of 40-meter nadir images with control is still more deviant than processes that include multiple heights or oblique images.

It can be concluded that missions that utilize high overlap oblique imagery and also include multi-elevation coverage will best serve to eliminate the doming/bowling effect. If multi elevation coverage is not possible, for example due to time or battery constraints, obliques from multiple directions should be utilized. If such obliques are not possible, for example if using a fixed wing craft only capable of nadir imaging, multiple altitude flights are recommended. It may be noted from past experience that fix wing craft flown in high winds tend to capture somewhat oblique images compared to when flown on perfectly calm days.

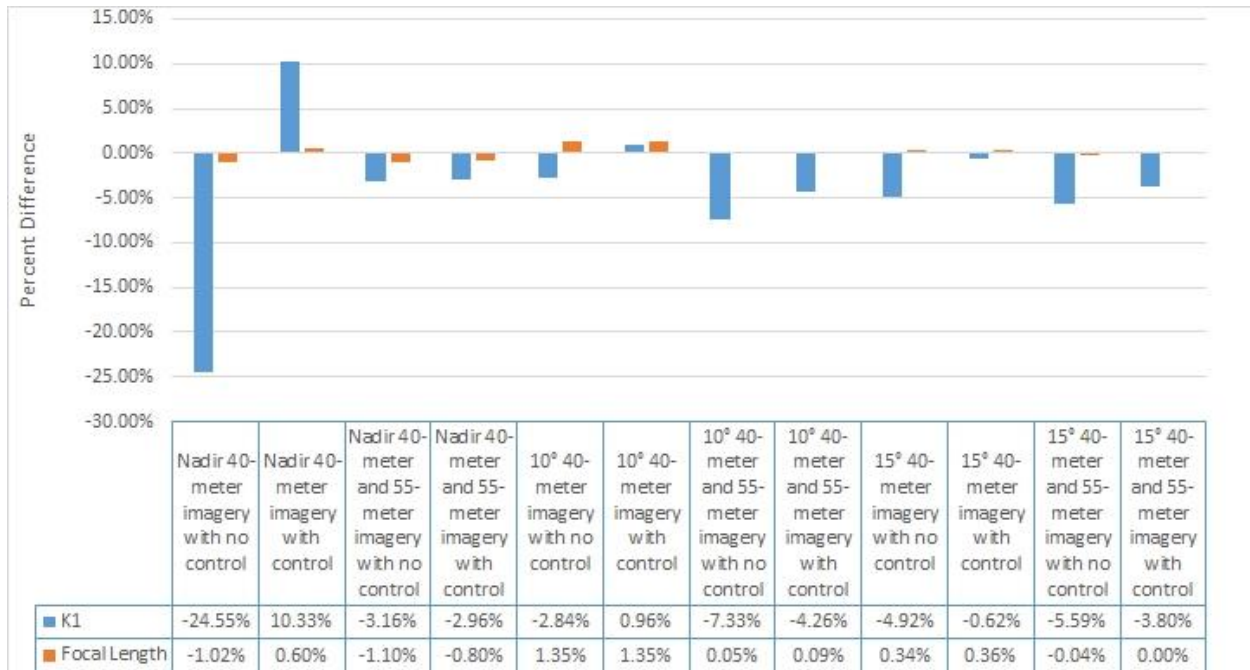


Figure 52. Graph showing K1, radial distortion, and Focal length percentage of difference from camera parameters solution of model with all images and control.

5.3.2 Rigorous Ground Control Network

A second case of undesirable bowing occurred on 08/15/2018 when a flight was performed with the DJI Phantom 4 Pro at 50-meters, utilizing 80% side and end lap, all at nadir camera orientation for a GSD of about 1.4 cm/px. The data was processed normally without control and with control examining how the use of control can rectify the doming effect. This data showed significant doming when no control was used in its processing. The inclusion of control subsequently fixed the issue.

For UAS datasets with only nadir images, rigorous control can alleviate the doming/bowing problem observed in SfM solutions. Vertical check point error for two solutions of the same nadir image set from 8/15/18 is shown. While the model without control had a severe amount of doming, the model created with rigorous control had vertical accuracies relative to the RTK check points in the centimeter range (see Figure 53).

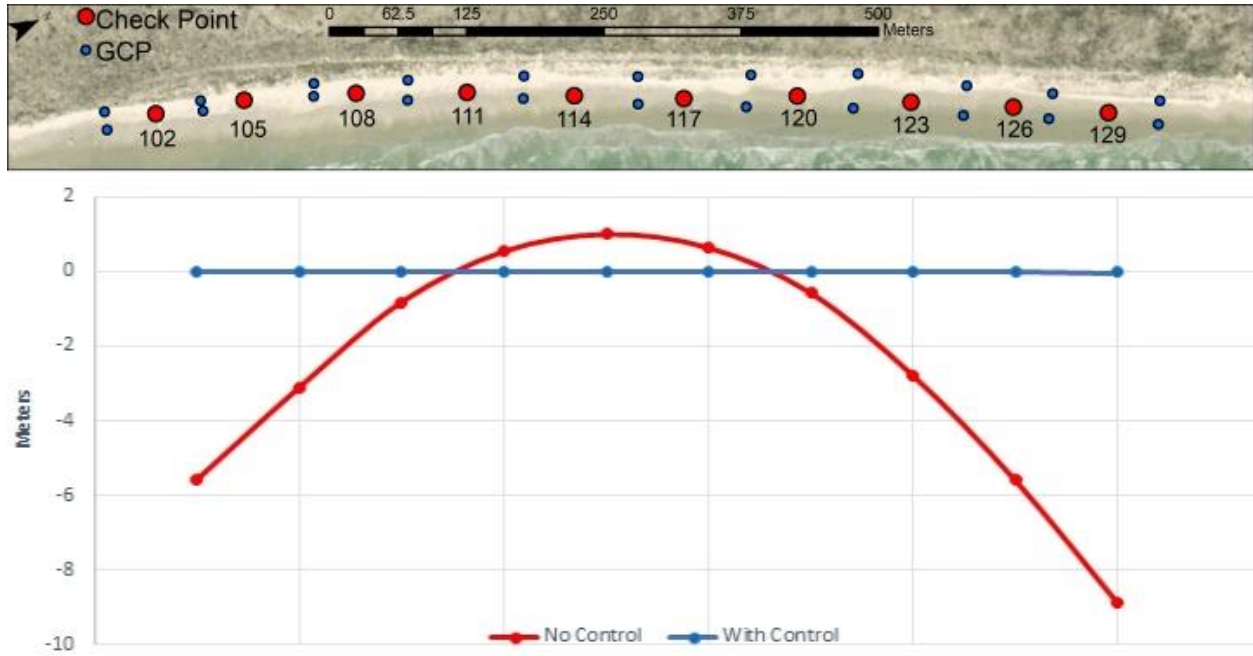


Figure 53. Error profile of Check points showing nadir image data set with and without control.

Figure 54. and Table 8. were generated from the process with no control, the parabolic distortion is easily visible in the DSM. The large Z residuals are apparent in the table as well with elevation being high in the middle and low at the ends.

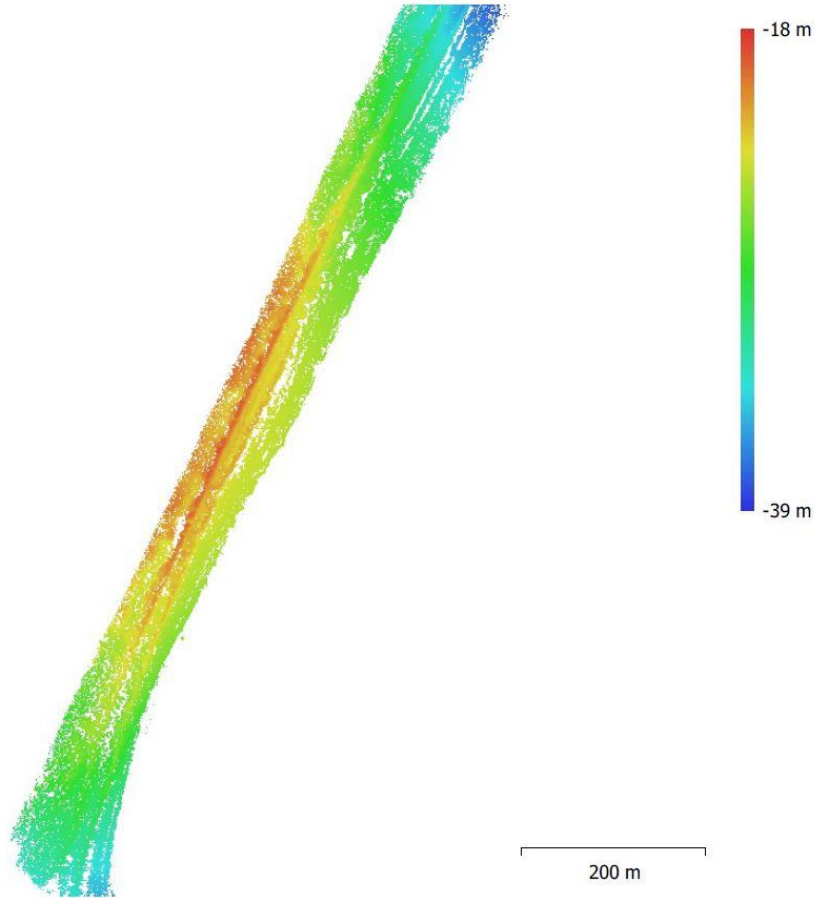


Figure 54. Metashape generated DSM from process with no control.

Table 8. Metashape processing report check point residuals from process with no control.

Label	X error m	Y error m	Z error m	3d error m	Pix error	No. Images
102	-1.677	8.252	-5.576	10.100	0.414	34
105	-1.725	7.050	-3.111	7.897	0.405	32
108	-1.958	5.709	-0.828	6.092	0.240	25
111	-2.291	4.631	0.529	5.194	0.284	27
114	-2.644	3.811	0.988	4.742	0.385	27
117	-3.011	3.180	0.633	4.425	0.284	26
120	-3.370	2.716	-0.577	4.366	0.232	25
123	-3.774	2.495	-2.782	5.311	0.354	26
126	-4.157	2.472	-5.580	7.384	0.312	25
129	-4.536	2.586	-8.858	10.282	0.369	25
Total	3.072	4.721	4.010	6.914	0.334	

Figure 55 and Table 9 were generated from the process using control, the DSM is even and sensible. The large Z residuals are reduced to the centimeter level when using control and can be seen in the table of check point residuals.

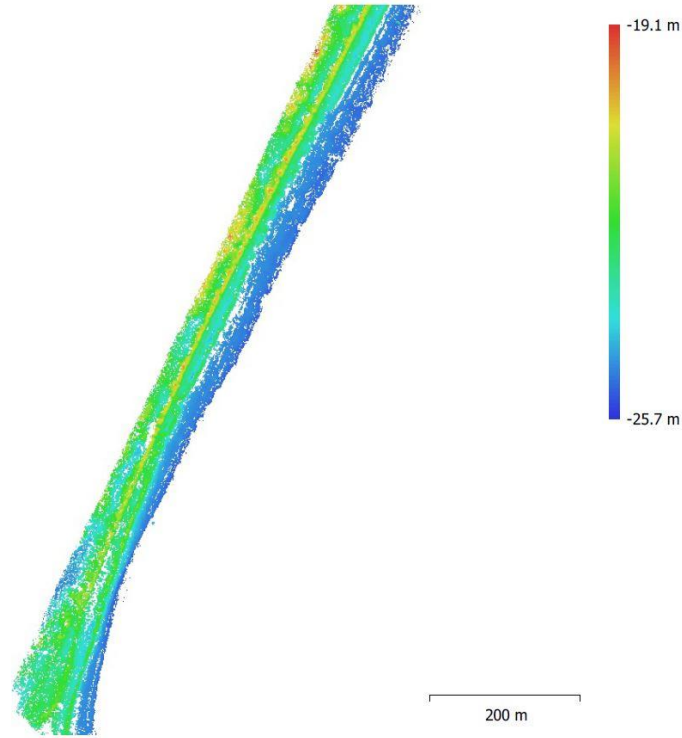


Figure 55. Metashape generated DSM created from process using control.

Table 9. Metashape processing report check point residuals from process with no control.

Label	X error cm	Y error cm	Z error cm	3d error cm	Pix error	No. Images
102	0.22	0.92	0.99	1.37	0.421	34
105	0.66	1.45	-0.21	2.70	0.413	32
108	1.00	0.38	-0.20	2.32	0.238	25
111	-0.15	-0.49	-0.10	1.20	0.292	27
114	-0.34	-1.05	-0.73	1.33	0.39	27
117	-1.12	-0.72	-0.87	1.59	0.289	26
120	-0.38	-1.07	-0.57	1.27	0.232	25
123	1.08	-0.42	0.15	1.89	0.357	26
126	1.51	0.79	0.37	1.74	0.317	25
129	0.45	1.03	-1.19	1.64	0.368	25
Total	0.81	0.89	1.29	1.77	0.343	

While strictly nadir flights are not of an ideal geometry for self-calibrated SfM solutions, the use of rigorous control can be used to prevent doming/bowling issues as results have shown here.

5.4 SfM Workflows and Processing

5.4.1 General SfM-MVS Workflow

A more detailed description of the SfM-MVS process is described in Section 3.2, here an attempt will be made to provide a general description of the workflow when using SfM software.

The first step is to import the images and their locations into the project. The image locations or geotags may be read from the image EXIF data or brought in separately via a text file. The next step is to generate the first sparse point cloud, that is performing the feature extraction, feature matching and a bundle adjustment while using faster lower accuracy settings. This will provide an initial estimation of image positions and scene geometry and a sparse point cloud. Generally, the next step would be to import any GCP/checkpoint coordinates. It is important at this stage to rectify all coordinate systems, being sure either all coordinate systems are either converted to the same system or labeled appropriately so the software can handle the relationships correctly. The next task is to identify all aerial target locations within the imagery. While this can be done before an initial bundle adjustment and sparse cloud generation, it is generally faster and less work to do so now that some initial geometries have been established. This is due to most software having some method of speeding up the target location identification within the image set and requires an initial estimation of geometries to do so. If the software supports masking certain areas of the image set, this can also be done at this point. In Metashape this is greatly accelerated by generating a mesh and then removing any portions of the mesh that represent areas of the photos that should be masked. Metashape can then use these

edits to create masks within your images by back solving the portions of the mesh that the user removed to the parts of the images used to generate them. Pix4D has its own methods of masking images. If GCPs are not used or there are no areas to be masked this initial step may be omitted.

Once the GCPs have been identified and denoted as constraints and/or check points, the process can begin in earnest. The feature extraction, feature matching, bundle adjustment and sparse point cloud generation can now be performed using the appropriate settings for the required accuracy and optimized with the control target network. This step will create the final geometries of the scene and all achieved accuracies will be reflected in any products generated afterwards. This step should include calculating the internal camera parameters, in Pix4Dmapper this is done automatically when the sparse cloud is generated while in Metashape it is a separate operation.

Once the sparse cloud is generated and the user is satisfied with the accuracies achieved, what follows is the generation of the dense point cloud. This is done via the MVS phase of the processing. The user should choose the appropriate settings that will determine the density and number of points in the cloud.

From the dense point cloud, it is necessary to create an elevation model in order to subsequently generate an orthomosaic. This can be a mesh or a raster DSM. To then generate the orthomosaic the software will mosaic the image set and use the elevation model to orthorectify the image. Orthorectification is the process of distorting the image so that each pixel is represented in a way as if viewed directly from nadir. This provides an image that is at a uniform scale that can be used for extracting horizontal measurements.

The final step is to generate a processing report. Such reports typically include the residuals to GCPs and check points, residuals from geotags to external camera parameter

estimations, quantify the image overlap throughout the scene, record the camera internal parameters estimation, and record all setting used throughout the project.

5.4.2 SfM Workflows Evaluated

The author is familiar with two popular commercial software suites for SfM-MVS processing, Agisoft's Metashape and Pix4Dmapper. Both software are capable of generating all typical survey products including point clouds, orthomosaics, digital elevation models (DEMs), and meshes. The workflows for the software have several differences throughout the SfM-MVS process, as described in SECTION 3.2, that will briefly be discussed here.

Both software suites are proprietary and hence the detailed workings of the various parts of their workflows are unavailable. That being stated it is possible to note a few observations gained from using both software packages.

Pix4Dmapper has the more streamlined lined workflow of the two suites. The software has fewer settings than Metashape and approaches the task of SfM-MVS product generation in a sequential series of steps. Those steps being: 1) project set up, which involves importing images, GCP coordinates, and setting of the three coordinate systems; image, GCP, and output. 2) Initial processing, in this step Pix4D mapper creates the sparse point cloud by performing the feature extraction, feature matching, and bundle block adjustment. 3) Point Cloud and Mesh, this is the MVS phase of the process, if the user desires a 3D mesh it is denoted and created here. 4) DSM, Orthomosaic and Index, this step is the creation of the DSM and Orthomosaic. If orthorectified mosaiced rasters of individual camera bands are desired, it is denoted here, also any index created are also specified here.

Steps two, three and four are the only places where processing can be initiated, and all previous results are over written. If one would like to compare results using different settings it is

necessary to copy them to a separate file location before rerunning anything. Any settings or options desired must be selected before processing of the step is started.

Pix4D seems to be designed primarily for UAS-SfM-MVS mapping and offers several “templates” which are preselected settings the user can choose before starting the process.

In the authors opinion Pix4d is a “black box” style software that is designed to simplify the SfM-MVS process for use by the everyday user. The software works very well and provides good accurate results when normal flight data is used. The author feels that Pix4D is a good choice in software for regular use with data from well-designed flights and surveys, particularly if the processing technician does not have an extensive background in photogrammetry and the principles there of.

Some notable disadvantages of Pix4D, in the authors opinion, are the inability to create DSMs and orthomosaics at different resolutions simultaneously, the inability to manually remove points from the sparse point cloud, and as of writing this, no support for multiple GPUs and less efficient use of GPU processing than Metashape.

The workflow of Agisoft’s Metashape is more open ended than that of Pix4Dmapper’s. In that once a project is opened the user may perform a myriad of operations if the requisite data has been generated previously. Generally working in Metashape is a more involved experience for the user. This has some advantages and disadvantages. Due to its open-ended design the user must be familiar with the SfM-MVS workflow to know what order to perform the various operations. While the learning curve may be fairly steep for the inexperienced, Metashape does have a decent help section that a new user can utilize to navigate through the proper procedures.

A large advantage Metashape has over Pix4D is that it can properly handle combined horizontal and vertical coordinate systems through the assignment of Geoid models. This allows

one to utilize control points that have orthometric heights, as well as output products directly to vertical datums that require a Geoid model. Pix4D mapper does not currently have this ability and uses a work around by letting a user apply a height shift factor to data's coordinate systems. While this is acceptable for small area surveys, larger areas need to be processed in ellipsoid heights and the data transformed to orthometric heights in some other software after output. Pix4D has released a new product called Pix4Dmatic that addresses this issue but as of writing the author has not investigated it.

Another example of the extra complexity involved in Metashape processing over Pix4D is the camera calibration. In Pix4D the calibration is performed automatically along with the bundle block adjustment during its initial processing step, while in Metashape the bundle block adjustment is performed initially utilizing only an initial set of fixed parameters based on values from its database, then additional bundle block adjustments may be performed that include camera internal parameter solutions. The user may choose which parameters he or she would like to solve for, which allows an iterative approach to reaching the final calibration values. During such an approach Metashape allows for the removal of points from the sparse point cloud by either manually selection or gradual selection via a set of quality metrics. This is useful as the tie points present in the sparse cloud are used when calculating the camera parameters. As it sounds, this is a more in-depth process than the one used by Pix4D, but the author feels that this allows much more customization or tailoring to individual sets of data.

While the data processing in Metashape does require more input from the user, it does allow several ways to accelerate the workflow. One is through the use of the GUI operated batch processing menu. This menu provides a simple way to order a list of operations and then run them sequentially. For example, once the sparse cloud is finished and all camera parameters and

accuracies are to the users liking, one could make a batch file for sequential generation of the dense point cloud, DSM, 3D mesh, and orthomosaic then export each one in a chosen file type and coordinate system. In the authors opinion Metashape's code takes advantage of GPU processing much more efficiently than Pix4Dmapper, similar operations take much less run time on the same machine when working with Metashape. Metashape allows for the use of multiple GPUs. Metashape has a python terminal built into its GUI and all operations may be scripted and run using python and Metashape's python library. And lastly Metashape allows for network processing that can utilize multiple machines for faster calculations. While the author has no personal experience with this network processing, colleges have implemented it and described it with praise.

In the author's opinion the main advantages of Metashape are its freedom, customizability, and rapid processing speeds. While the main disadvantages are a steeper learning curve than Pix4D, more involved user effort when using it, and more chances to make mistakes than when using Pix4D.

5.4.3 Tommy Nobel Workflow in Agisoft

The author's preferred processing workflow for use in Agisoft comes from the USGS. Written by Tommy Nobel, the workflow focuses on creating a consistent and accurate model by removing uncertainty from poor geometry, bad pixel matching and poor residual errors. Released in March 2017 by the USGS National Unmanned Aircraft Systems (UAS) Project Office, the method was provided as an introductory training class (USGS, 2017). The author has found this workflow to achieve the most noise free point clouds and lowest residuals of any processing workflow explored. The accompanying workflow pdf is shown here in Figure 56.

Agisoft PhotoScan Workflow

Steps	Menu	Function	Action
Photo Setup, Alignment, Adjustment			
1	Main Menu - Workflow	Add Photos	Navigate to directory with photos. Select and add all necessary photos for project
2	Reference Panel - Settings	Set Coordinate/Projection	Select the Coordinate System (Local, Geographic, Projected) and Select Projection (i.e. WGS84)
3	Main Menu - Tools	Camera Calibration	Check to make sure that all the photos with the same focal distance/parameters are grouped together
4	Main Menu - Workflow	Align Photos	Settings: high, generic or referenced, 60,000, 0
5	Reference Panel - Optimize	Initial Bundle Adjustment	<input checked="" type="checkbox"/> Check on: f, cx, cy, k1, k2, k3, p1, p2
Error Reduction & Bundle Adjustment			
6	Main Menu - Edit Gradual Selection	Reconstruction Uncertainty (Geometry)	Set Level: 10 (if more than 50% of pts are selected, increase the level to a higher value (limit 50))
			Delete the points, Optimize
			<input checked="" type="checkbox"/> Check on: f, cx, cy, k1, k2, k3, p1, p2
			Repeat and least 2 times and continue to lower the level closer to 10 without having to delete points
			Monitor: Projections goal not less than 100, Error (pix) goal = .3, SEUW = 1.0
7	Main Menu - Edit Gradual Selection	Projection Accuracy (Pixel Matching Errors)	Set Level: 2 - 3 (if more than 50% of pts are selected, increase the level to a higher value (i.e. 3))
			Delete the points, Optimize
		Tighten Tie Point Accuracy Value	<input checked="" type="checkbox"/> Check on: f, cx, cy, k1, k2, k3, p1, p2
			Repeat and least 2 times and continue to lower the level closer to 2 without having to delete points
			Change the settings of the tie point accuracy (pix) from 1 to .1
			Optimize
			<input checked="" type="checkbox"/> Check on (all): f, cx, cy, k1, k2, k3, k4, b1, b2, p1, p, p3, p4
			Monitor: Projections goal not less than 100, Error (pix) goal = .3, SEUW = 1.0
8	Main Menu - Photo Edit Markers	Add Control Points (Markers)	Import in the ground control points (if available), manually select or use autodetection on individual images
		Add Scale Bars	Select the Coordinate System (Local, Geographic, Projected) and Select Projection (i.e. WGS84)
9	Main Menu - Edit Gradual Selection	Reprojection Error (Pixel Residual Errors)	Set Level: .3 (if more than 10% of pts are selected, increase the level to a higher value)
			Delete the points, Optimize
			<input checked="" type="checkbox"/> Check on (all): f, cx, cy, k1, k2, k3, k4, b1, b2, p1, p, p3, p4
			Repeat until reaching the .3 level without having to delete points
			Monitor: Projections goal not less than 100, Error (pix) goal = .3, SEUW = 1.0
Build Dense Point Cloud, Mesh, Texture, DEM, Orthomosaic			
10	Main Menu - Workflow	Build Dense Cloud	Quality: High, Med, Low Depth Filtering: Aggressive
		Build Mesh	Height Field, Dense cloud, High Interpolation: Enabled
		Build Texture (optional)	Orthophoto, Mosaic
		Build DEM	Set Coordinate System/Projection, Dense Cloud, Enabled
		Build Orthomosaic	Geographic, Set Coordinate System/Projection, Mesh, Mosaic

USGS National UAS Project Office – March 2017

Figure 56. Tommy Nobel Agisoft workflow.

Another good source of information for UAS mapping and processing with Agisoft is a separate presentation from the USGS National Unmanned Aircraft Systems (UAS) Project Office that gives a conceptual overview is titled Processing UAS Imagery using Agisoft Photoscan (USGS, 2017). Note that both documents were written in 2017 when Agisoft’s Metashape was named Photoscan. There are some slight differences in the menu locations and options shown in the presentations, but all of the information still applies.

5.5 Autonomous GNSS Image Geotag Elevation Rectification

As discussed in section 4.3.3, methods were explored to improve erroneous image location elevation data. The data used was obtained with the Phantom 4 Pro during the quarterly

survey performed on 02/04/2019. The resultant residuals from processing runs both with and without elevation adjustments are shown in the following tables. It should be noted that Metashape reports residuals to the 5th decimal place in cm even though that level of accuracy is well below the uncertainty of the methods. They have been left in the following tables, table 10. And table 11. in order to show the difference between the run with elevation rectification and the run without. As can be seen, the application of the method does not improve the residuals in any measurable manner.

Table 10. Adjusted geotag elevation processing run residuals.

Count	X error (cm)	Y error (cm)	Z error (cm)	XY error (cm)	Total 3d (cm)
16	2.01586	2.54053	12.4479	3.24315	12.8635

Table 11. Unadjusted geotag elevation processing run residuals.

Count	X error (cm)	Y error (cm)	Z error (cm)	XY error (cm)	Total 3d (cm)
16	2.02244	2.53176	12.428	3.24038	12.8435

Table 12. Adjusted geotag elevation residuals minus unadjusted geotag elevation residuals.

A - U	X error (cm)	Y error (cm)	Z error (cm)	XY error (cm)	Total 3d (cm)
Diff	-0.00658	0.00877	0.0199	0.00277	0.02

The difference in residuals in this case was negligible and well below the uncertainty levels of the equipment used. However, when the DSMs from each of these processing runs were differenced then visualized using a percent clip stretch at 0.5% min and max, very interesting patterns appear due to the inherent noise in SfM solutions at the current time and limit of processing technology. Because the difference in the two solutions is on the order of micrometers, the resultant DoD resembles a hill shade and resolves small features such as tire tracks and other textures quite well as shown in the following image (Figure 57).

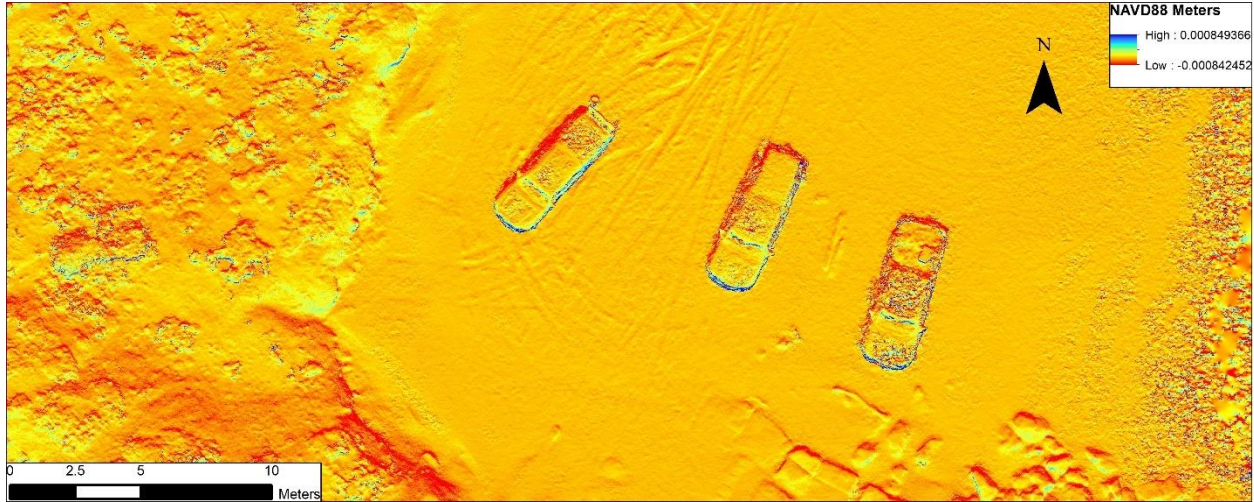


Figure 57. DoD showing the micrometer level differences between two very similar processing runs; shows texture and elevation relief similar to a hill shade and is included here for novelty. Created by subtracting the unadjusted elevation DSM from the adjusted elevation DSM discussed in Section 5.3.

The amount of adjustment applied to each flight varied as well. There were 4 flights in this survey, each requiring a different magnitude of adjustment to better align them with their altitudes above take-off. These adjustments were calculated using the method where the true ellipsoidal elevation of the takeoff point was differenced to the average of the mission image locations then checked against the intended mission height above take-off and are shown in Table 13.

Table 13. Blanket elevation adjustments applied per flight.

Flight 1	Flight 2	Flight 3	Flight 4
+ 7.81 m	+ 4.19 m	+ 1.10 m	- 3.49 m

While these are not the largest elevation discrepancies between sequential flights the author recalls witnessing, the largest discrepancy was near 11 meters. When the external camera

parameters are solved during the bundle block adjustment it is possible to difference the distance between the estimated positions and the original positions in the geotags. The following tables show the average camera location error from both processing runs.

Table 14. Adjusted Elevations Average Camera Location Error.

X error (m)	Y error (m)	Z error (m)	XY error (m)	Total error (m)
1.561	4.228	3.502	4.508	5.708

Table 15. Unadjusted Elevations Average Camera Location Error.

X error (m)	Y error (m)	Z error (m)	XY error (m)	Total error (m)
1.559	4.229	3.986	4.507	6.017

It is shown that Metashape had to relocate the camera positions 48 cm less on average in the vertical and 30 cm less on average over all for the process with adjusted elevations than the process with unadjusted elevations. It can be concluded that in this case that the adjustment of the image location elevations so that they more accurately relate to the elevations of the targets and their true altitude gains negligible accuracies and is not worth performing for the sake of increasing product accuracy.

It should be noted though that when identifying aerial target location within an image set much zooming and scanning can be involved for the processing technician. When using SfM software's built-in methods for locating aerial targets in images, the software may not be able to locate the aerial targets unaided until two have been found manually and tagged (clicked upon). Having one's image locations and target elevations presenting large elevation relationship discrepancies can exasperate this problem. In other words, having the image locations as close as possible to their true heights relative to the targets can save significant time in user input and

may sometimes be worth the effort. A situation where this can arise that should be avoided at all costs is trying to process images in ellipsoidal heights using targets with orthometric heights.

5.6 Orthometric Heights Versus Ellipsoid Heights for Control

As mentioned in the previous section, attempting to process data with relational discrepancies between image locations and target locations can impact the accuracies of the image and target positions. This subsequently impacts accuracy of UAS-SfM point cloud data. Usually, targets are denoted of having a strong positional accuracy that reflects the method used to locate them, for example, +/- 2 to 4 cm vertical for targets located with a survey grade GNSS via RTK methods. Image locations can be assigned accuracies individually if denoted by the UAS mapping system, as is the case for most commercial UASs, or assigned manually if such information is not available. Slocum et al. stresses the importance of maintaining correct image location accuracies (Slocum et al., 2019). This problem of relational discrepancies can be exasperated when image locations are available in ellipsoidal heights but GCPs are available in orthometric heights. This situation should be avoided at all costs. When utilizing differentially corrected image locations that have high accuracies, maintaining a consistent vertical datum throughout the project/SfM processing is paramount. This author has witnessed attempts to use orthometric target heights with ellipsoidal PPK derived image locations and the large errors in the sparse point cloud it incurs. Not only are the aerial targets particularly difficult to locate in this situation, the higher constraints applied to both target and image coordinates created wild artifacts in the sparse point cloud. Fortunately, the time this was witnessed the problem was corrected and processing continued as normal. Often, when using images with autonomous GNSS locations, the vertical positional accuracy is on the order of 10 or 15 meters and can be given a low weight in the bundle block adjustment to account for any geoid and ellipsoid

separation. This will allow the SfM software to constrain to the targets in orthometric heights and shift the images accordingly. This author has witnessed this approach successfully used many times, but it is not recommended as lowering the positional accuracies of the image locations may lead to a weaker external camera position solution and introduce unnecessary error into the resultant data. It is always better to keep the image location accuracies as realistic as possible and convert both image locations and target locations to the same vertical datum before processing. While Metashape has introduced the capability to handle geoid models and convert between orthometric and ellipsoidal heights, this author finds processing simpler to keep all heights ellipsoidal and convert project heights to orthometric when exporting.

This begs the question: which vertical datum should be used when processing? Most organizations and/or clients prefer their products delivered in orthometric or tidal datums. According to Slocum et al. (2019), SfM software generally converts from geodesic to ECEF coordinates in the background when processing in order to alleviate the need to account for Earth's curvature or compensates for any other distortions when working in or converting to projected coordinate systems, such as state plane or UTM. In this author's opinion, it is reasonable to assume that without a proper geoid model utilized, SfM software may not be able to correct for geoid undulations present across large distances when working with orthometric heights. For this reason, this author recommends to always work with ellipsoidal heights with all project/control data and convert finished point clouds and DSMs to orthometric heights using external software. This is deemed a best practice. The author has had success using NOAA's VDatum (NOAA, 2021) tool for this purpose although the processing of large raster data has been painstakingly slow. For this reason, the inclusion of the proper geoid model in one's chosen SfM software is important in order to work in and process directly to orthometric heights if

desiring to not convert externally. The SfM processing in this project was all performed using ellipsoidal heights and converted to orthometric heights upon export when desired. It should be noted that this is possible using Metashape, but if one is using PIX4Dmapper the conversion must be done in external software after the products are exported.

5.7 GSD and Resolving Oiling on a Beach

The ability to resolve oiling on the beach is a function of the size of the oiling to be seen and the spatial resolution of the imagery. UAS used for mapping typically use consumer-grade RGB digital cameras. A digital image comprises a two-dimensional array of individual picture elements called pixels arranged in columns and rows. Each pixel represents an area on the Earth's surface. In remote sensing, spatial resolution refers to the size of the smallest object that can be resolved in an image. It is primarily a function of the pixel size. In the practice of UAS surveying, pixel size here is denoting GSD, which is the area of the ground that each pixel represents. In a digital image, the spatial resolution is limited by the GSD, i.e. the smallest resolvable object cannot be smaller than the inherent image's GSD. A "high resolution" image refers to one with a smaller GSD (or smaller projected pixel size). Finer details can be seen in a higher-resolution image. On the other hand, a "low resolution" image is one with a larger GSD (or larger projected pixel size), i.e., only coarse features can be observed in a lower-resolution image. For example, a 2 cm GSD pixel would represent a 2 cm x 2 cm area on the ground as a single value per band, in other words a single brightness value for that wavelength or color (called a digital number). At a 2 cm GSD it would, in general, not be possible to resolve or identify a half-cm round piece of tar or oiling because its spectral reflectance would get blurred with other background reflectance inside the pixel.

Understanding the desired minimum mapping unit or size for a respective feature is an important consideration when designing flights for mapping of oiling events or detecting other objects along beaches, such as plastics and debris. One's choice in UAS flying height for a given camera setting, which impacts the GSD, will have a direct impact on the size of detectable features in the respective imagery. As a general rule of thumb, the object needs to be at minimum 4 times the size of the area represented by the GSD. So, at a 2 cm GSD, the smallest possible tar ball that could be resolved would need to be 4 cm x 4 cm in size. 2 cm was chosen for this example because it is an efficient and reasonable GSD to be obtained by UAS surveying, although smaller GSDs are quite possible. It is important to mention, however, that spatial resolution of an image is not only a function of the GSD. Digital cameras convert the light that falls on the image sensor into electrical signals for processing, which affects spatial resolution. A camera's ability to do this is impacted by the quality of the sensor, radiometric resolution, camera settings such as ISO sensitivity, and ambient conditions such as natural lighting at the time of imaging. ISO sensitivity is a measure of the camera's ability to capture light, and it can be artificially raised in a camera by amplifying the signal. Figure 58 shows an example of the relationship between GSD and visibility of different size oiling features within UAS imagery acquired along Mustang Island after the Buster Bouchard Barge No. 255 explosion that occurred off the coast of Port Aransas back in October of 2017.

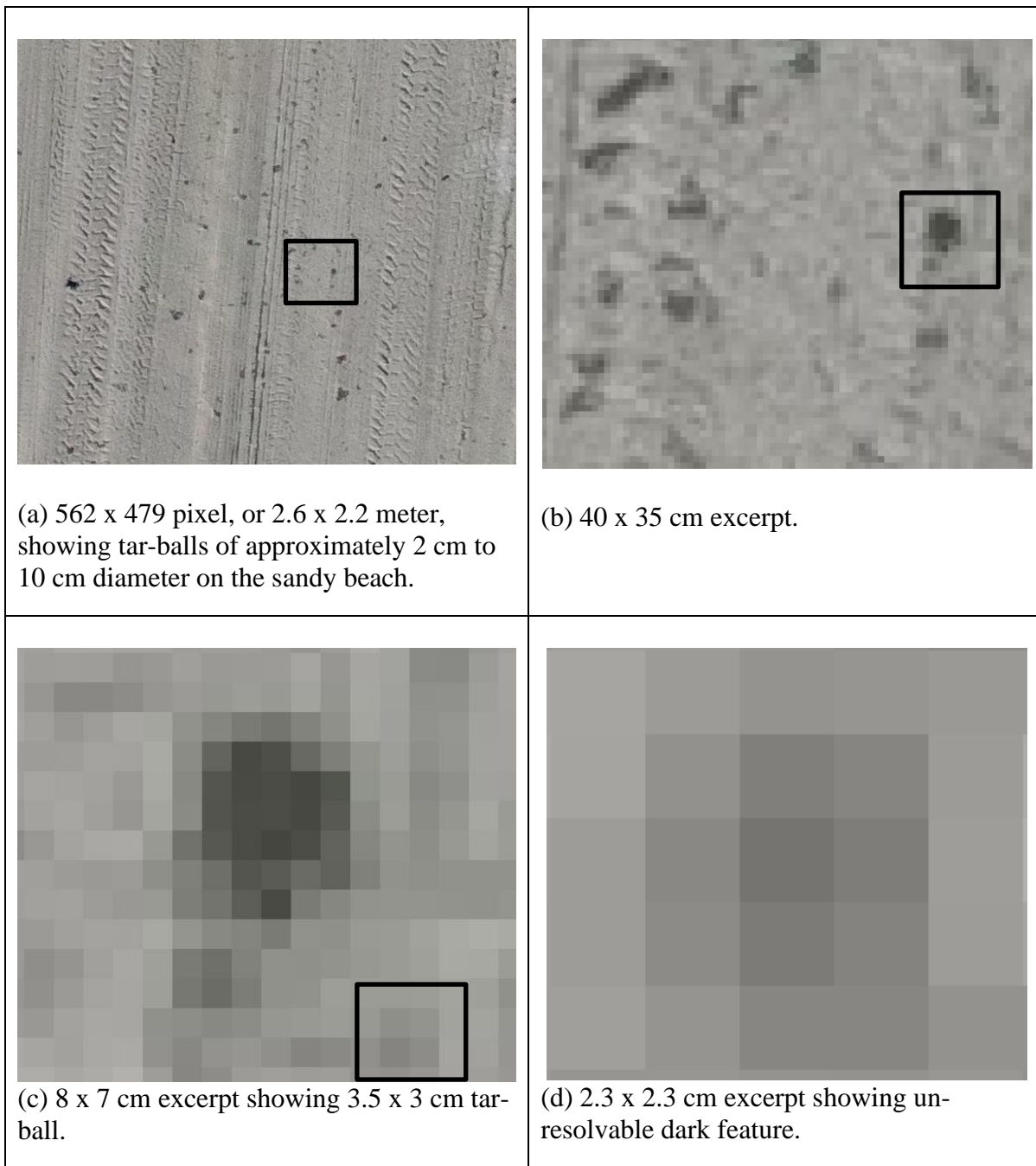


Figure 58. Example of a UAS orthomosaic at 0.45 cm GSD zoomed in at different geographic scales showing the appearance of different size oiling features. The orthomosaic was generated from images captured over a 1-mile section of beach on Mustang Island north of the Fish Pass Jetties. The imagery was acquired on 10/23/2017 between 5:05 and 6:45 pm. This was approximately 73.5 hours after the explosion onboard the Buster Bouchard Barge No. 255, which occurred ~3.25 miles off Port Aransas, Texas.

5.8 Evaluation of UAS-SfM for Rapid Response Mapping

5.8.1 Rapid SfM Processing of Still Images for Orthomosaic Generation

As discussed in Section 4.5, methods were investigated to rapidly generate orthomosaics from UAS flights in times of need such as disaster or emergency situations. The lowest quality, most rapid processing time, settings were used to generate an orthomosaic from a normal mapping flight data set and its accuracies compared to the same images processed normally. In Metashape the sparse cloud generation step was set to the lowest possible image scale, called *accuracy* in the software, with the setting named *lowest*. The dense cloud generation was also set to the lowest possible image scale, called *quality* in the software with the setting named *lowest*. The DSM was interpolated from the dense cloud at the software's standard resolution of $\frac{1}{4}$ the image GSD which was then used as the surface for orthorectification of the merged images at their full GSD. The 10/14/2019 DJI Phantom 4 Pro data set was used. It contained 974 images and covered 3.5 km of the beach study site. These processing runs were performed on the same Puget machine as described in section 4.1.3 with Metashape. It should be noted that the aerial targets were located and tagged in the images during the normal processing run which took roughly an hour to perform. Also, in the normal processing run, the Tommy Noble iterative sparse cloud generation/camera parameter calibration was performed, a time-consuming process that takes about another hour. The rest of the user input and time consumed for both runs are fairly similar and includes things like loading the images, naming the output files, and generally clicking and pushing of buttons; this time should be considered about 20 minutes for a practiced user but would vary from person to person. Also, the reports do not track the time it takes to generate and export data such as the point cloud, DSM, orthomosaic and processing report. Because the concern here is only the orthomosaic, it would be an equal export time of about 5

minutes for either process. Also, this evaluation is to gain an understanding of the general amount of time saved by using rapid settings for orthomosaic generation using the same computation resources but different SfM processing settings in the software, rapid versus normal. Lastly, this was all performed using version 1.5.2 build 7838 of Metashape, future updates could change the ratio of these comparative times. Each update seems to decrease processing time. The following table shows a breakdown of the computer processing times from the individual reports.

Table 16. Metashape processing time with normal settings.

Matching Time	1 hour 26 minutes
Alignment Time	49 minutes 36 seconds
Optimization Time (single)	16 seconds
Depth Map Generation	31 minutes 27 seconds
Dense Cloud Generation	24 minutes 32 seconds
DEM Generation	3 minutes 45 seconds
Orthomosaic Generation	18 minutes 33 seconds
Total	3 hours 34 minutes 9 seconds

Table 17. Metashape processing times with most rapid settings.

Matching Time	3 minutes 55 seconds
Alignment Time	2 minutes 10 seconds
Optimization Time (single)	21 seconds
Depth Map Generation	30 minutes 50 seconds
Dense Cloud Generation	2 minutes 31 seconds
DEM Generation	40 seconds
Orthomosaic Generation	20 minutes 27 seconds
Total	1 hour 54 seconds

The time savings solely in computer run time was 2 hours 33 minutes and 15 seconds. For the full process including target tagging and using a more accurate calibration method, the total time to produce an orthomosaic was roughly 6 hours, yet with the rapid settings, less intensive calibration, and exclusion of GCPs the time was roughly 1 hour and 20 minutes.

Generating an orthomosaic in this manner saves about 4 hours and 40 minutes in processing.

Note as shown in section 4.2.1.3 the flights to acquire the image set took slightly over an hour on site. The images consist of 7.9 GB of data. Transferring that amount via a cellular network may take some time, downloading them from the SD card to a laptop may take 20 minutes or so, both of which are beyond the scope of this investigation.

5.8.2 Comparison of Rapid Processing versus Normal Processing Accuracy

Nineteen aerial targets were present throughout the study site during the survey. All were utilized during the normal processing run in order to gain the most accurate orthomosaic possible to be used as a rubric for the rapid orthomosaic. Since elevations are not present in orthomosaic data, they will not be considered here. The XY 2D RMSE from the 19 control targets that were all used as constraints was 1.2 cm as reported in the processing report for the normal processing run (where GCPs would be used for accurate georeferencing). With the same UAS in similar flights of the study area that contain a similar number and geometry of GCPs, and include check points, the XY 2D residuals of the check points tends to be slightly larger but similar to the GCP XY 2D residuals. From experience, the author will state with confidence that if there had been check points present, the XY 2D residuals would not exceed 3 cm and would probably be less assuming the same rigorous control network and RTK accuracy for the control. That being said, the check point residuals for the rapid orthomosaic generated here are presented below in Table 18 to shown how much positional error there is based solely on the autonomous GNSS solution using rapid processing.

Table 18. Total RMSE from all check points (no GCPs) in rapid orthomosaic.

Count	X error (m)	Y error (m)	Z error (m)	XY error (m)	Total error (m)
19	2.291	4.218	8.162	4.800	9.470

Due to the errors in the autonomous GNSS on the UAS this error is not evenly distributed across the study site. The following Figure 59 and Table 19 show the check point distribution and error magnitude and direction.

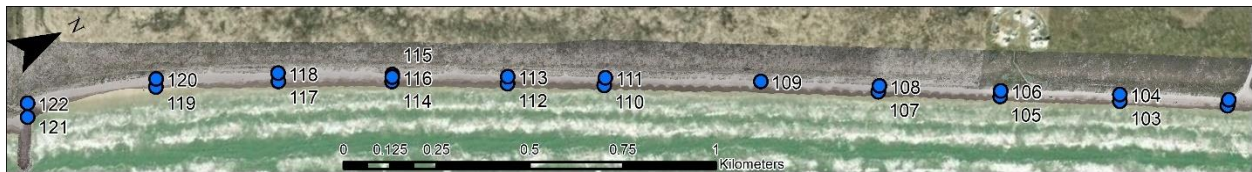


Figure 59. Rapid orthomosaic check point locations.

Table 19. Rapid orthomosaic check point (no GCPs) residuals showing error variance in magnitude and direction.

Count	X error (m)	Y error (m)	Z error (m)	XY error (m)	Total error (m)
101	5.632	-8.403	-2.766	10.487	0.029
103	4.304	-6.565	-4.031	8.825	0.062
104	4.399	-6.475	-4.387	8.974	0.086
105	2.909	-4.922	-5.024	7.611	0.07
106	3.001	-4.852	-5.234	7.742	0.096
107	1.699	-3.385	-5.777	6.908	0.084
108	1.760	-3.340	-6.006	7.094	0.144
109	0.790	-2.018	-6.899	7.231	0.04
110	-0.269	-0.476	-7.735	7.754	0.06
111	-0.190	-0.452	-8.027	8.042	0.071
113	-0.487	0.500	-8.381	8.410	0.036
114	-0.635	1.618	-8.604	8.778	0.037
115	-0.573	1.609	-8.802	8.966	0.04
117	-0.838	2.650	-9.500	9.899	0.077
118	-0.749	2.665	-9.770	10.155	0.117
119	-0.957	3.983	-10.936	11.679	0.079
120	-0.893	3.982	-11.199	11.920	0.125
121	-1.063	5.335	-11.500	12.722	0.073
122	-0.919	5.276	-12.004	13.144	0.074
Total	2.291	4.218	8.162	9.470	0.077

The following figures (Figure 60, Figure 61, and Figure 62) show how the error shifts throughout the rapid orthomosaic by showing the rapid orthomosaic overlaid upon the orthomosaic created using control and slower more accurate settings presenting a visualization of the errors in above Table 19.



Figure 60. North end of survey with rapid orthomosaic showing a shift to the Southeast.



Figure 61. Center of Survey with Rapid Orthomosaic showing a slight shift to the Southwest.



Figure 62. South end of survey with rapid orthomosaic showing a shift to the Northwest.

It is shown that while the rapid orthomosaic produced in this manner has good resolution and clarity with no major, sudden deformations, it would not be very suitable for accurate change detection measurements over time. But with a time savings of four and a half to five hours in processing, based on the software version and computational resources utilized, it may be a valuable method for use in rapid UAS-based site assessment by decision makers in critical situations, such as oil spills.

5.8.3 Rapid SfM Processing of Videography Data for Orthomosaic Generation

As discussed in section 4.5.2, an attempt was made generate a rapid orthomosaic using a quickly obtained video of the study site. The video used was captured on 10/14/2019 using the Phantom 4 Pro and covered the entire 3.2 km of beach in the study area. Flown manually an altitude was chosen that filled the live stream view on the flight controller's tablet with the beach nicely and worked out to be roughly 50 meters. The GSD of the video was varying across the view since the camera angle was oblique as described below, with the orthomosaic GSD being determined in processing. The video is 7.21 GB in size, and took about 20 minutes to fly and capture. As shown in Figure 15, the flight consisted of two flight lines, oriented North and South with one near the water line and one near the dune line. The camera was set to an oblique angle

of about 15° above nadir. In processing, still images were extracted from the video at one second intervals giving an end-lap of roughly 85%. The hopes were that the time saved in flying, and the lack of need for mission design and use of flight control software, could be used to rapidly generate an orthomosaic in situations where time was critical, such as oil spill response. As the stills from the video do not contain any locational information, the scene reconstruction depended completely on the sift algorithm and self-calibration in the SfM workflow. The first attempt to process the flight used the lowest/rapidest setting for the feature extraction/initial alignment. This failed to align a majority of the images and the sparse cloud generated was unusable. The second attempt at processing utilized medium settings and while most of the images were aligned and the scene reconstructed, the scene doubled over on itself, again making the data unusable. A third attempt was made using the highest/slowest settings, and once again the scene was doubled over on itself making the data unusable for orthomosaic generation.

As shown in Figure 63, Figure 64, Figure 65, and Figure 66, without precise side-lap control and only having two flight lines, there was not enough feature matching and correspondence information for scene reconstruction. A few attempts were made to add control points to try to get a successful reconstruction, but all was for naught. The author decided that the added effort in processing, or the added time and batteries to obtain more flight lines would offset any advantages in rapid orthomosaic generation gained from using video for mapping the study site. In other words, if more flights up and down the beach were videoed, bringing the total from two to four it is likely that there would be enough image geometry to get an SfM solution using stills from video sans their image locations. This may be a viable option for a UAS pilot that for some reason did not want to use mapping flight control software and/or auto pilot, but the product would be less accurate than doing so with little to no time savings.

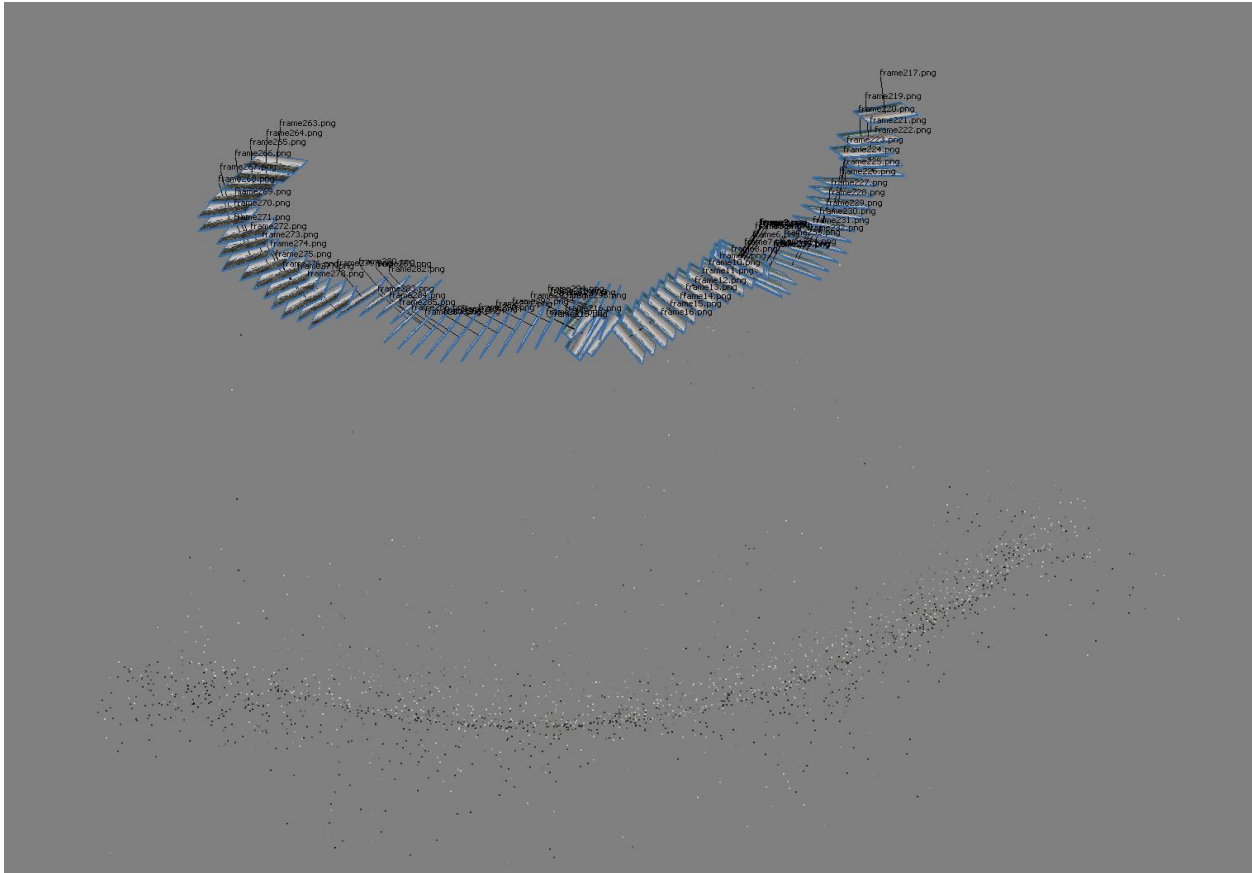


Figure 63. Attempted scene reconstruction from video stills with no geotags using rapid processing settings.

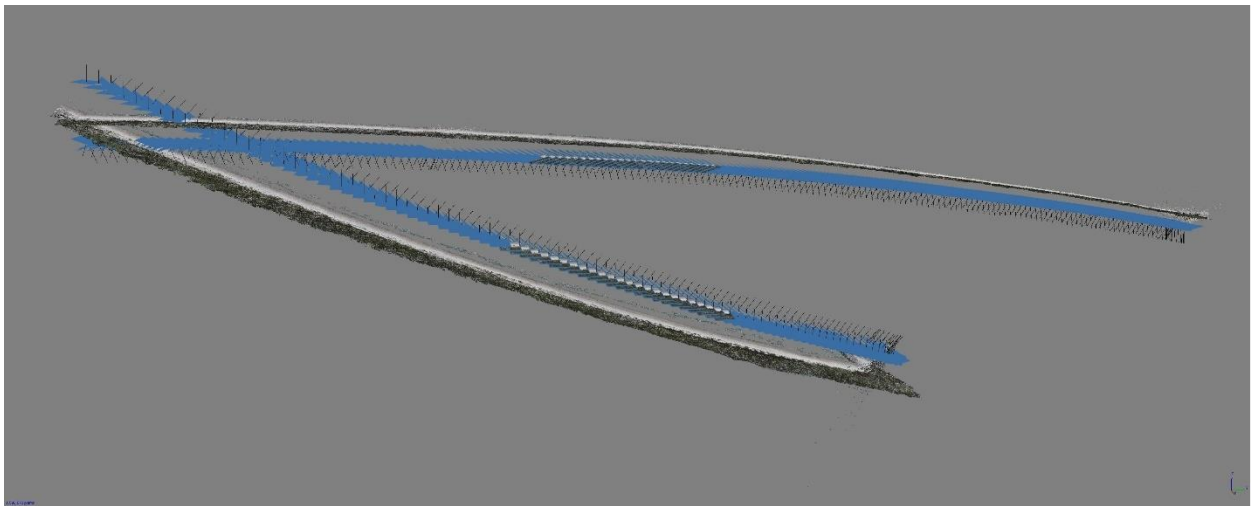


Figure 64. Attempted scene recreation from video stills with no geotags using medium rapid/accurate processing settings.

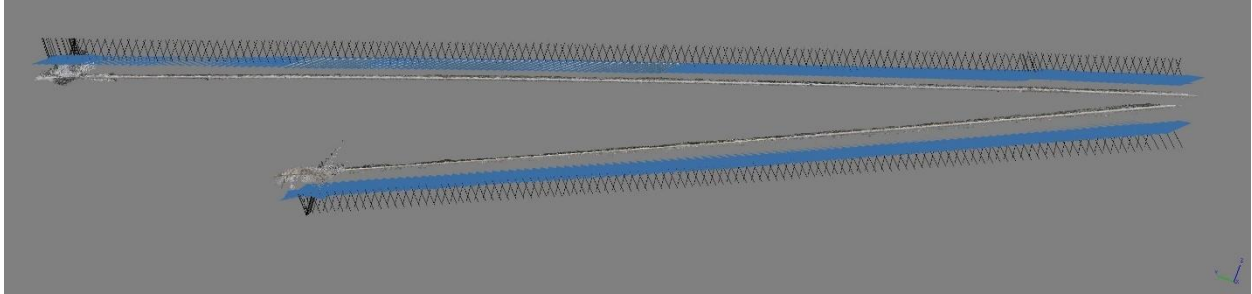


Figure 65. Attempted scene recreation from video stills with no geotags using slowest/most accurate processing settings.

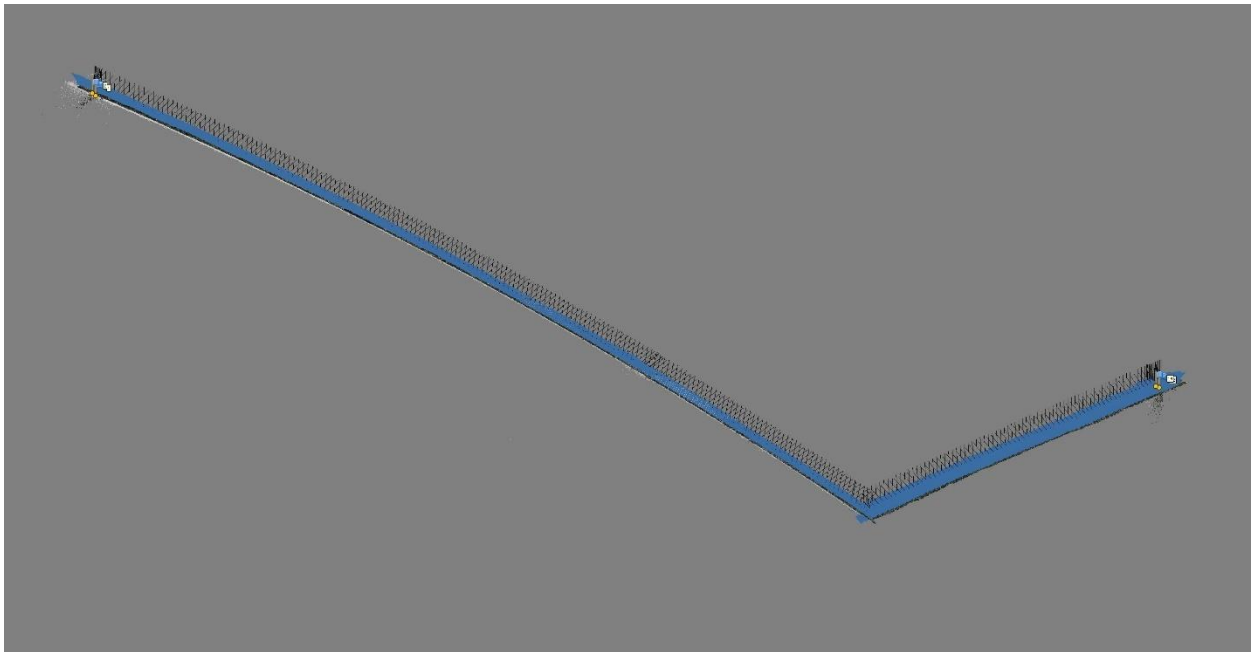


Figure 66. Attempted Scene Recreation from video stills with no geotags using slowest/most accurate processing settings and minimal control.

5.8.4 Advantages of UAS Video to Standard SCAT Reconnaissance

As discussed in Section 4.5, recording video from a UAS to document the beach in video format was considered.

The video on the UAS used was stored on the micro-SD in the craft. From that point it can be transferred into whatever storage medium is appropriate. The video itself is easy to produce and costs nothing more than the wear on the UAS and the electricity needed to charge the batteries. Yet it provides valuable documentation of the beach. In the video produced for this

study one could easily make out clumps of seaweed that are near 10 cm around. The application of UAS recorded videos for documentation of spill events seems advantageous and could be considered for use by decision makers.

5.8.5 Importance of Documenting the Video Flight and Inclusion of Landmarks

The study video contains several identifiable landmarks such as beach access road number 2, the Fish Pass Jetties, and a wooden dune walk over bridge connecting to a neighborhood. As there is no locational metadata from the UAS GNSS recorded to the video, and the inclusion of landmarks could help with the documentation of the location recorded. It is important to note that common UAS systems do not store location data in their video files. It is advisable to make note of the area being videoed.

Most off the shelf UAS systems, the DJI Mavic series for example, provide a real time distance from the remote-control unit to the UAS. When documenting a beach with video, it may be prudent to record one's remote-control location with a handheld GNSS or possibly take a picture with the UAS that has the location stamped in its Exif data, then note the distance flown in order to maintain record of the area covered. Another possibility for location documentation would be to extract the flight logs of the day from the UAS. This is possible with DJI products by connecting them to a computer and transferring the .DAT files from the craft. The said files may then be converted to .KML files and easily viewed in Google Earth. Such a record appears in Figure 15 above.

CHAPTER VI

Conclusion

6.1 Summary and Contributions

This study aimed to examine how UAS-SfM can be implemented to best benefit the SCAT processes during spill events on Texas sandy beaches. By performing field tests on Texas beaches with the goal to simulate conditions in the environment of concern, experiments were executed with the goal of determining best practice recommendations for the TGLO to aid in integrating UAS-SfM surveying into SCAT procedure.

Without GCPs, SfM processing with PPK/RTK-enabled image locations can achieve remarkably higher accuracy (i.e., RMSE = 7.95 cm on z residual for 10 check points) than that with autonomous GNSS image geotags (i.e., RMSE = 161.84 cm on z residual for 10 check points). Adding more GCPs can exponentially improve the overall accuracy for autonomous GNSS geotagged images. For the specific study area, 10 GCPs made the accuracy of the autonomous GNSS SfM products (i.e., RMSE = 2.49 cm on z residual for 10 check points) comparable to that of the PPK/RTK-enabled products (i.e., RMSE = 2.09 cm on z residual for 10 check points). After this point, adding more GCPs did not significantly improve the SfM accuracy for both GNSS image location determination methods. Therefore, if aircraft hardware cost is largely a limiting factor and rigorous control networks that follow ASPRS Accuracy Standards for UAS surveys are planned to be used, the advantage of RTK/PPK differential GNSS image locations over autonomous is minimal.

The z residuals of a generated DSM were better near the center of the beach and worse towards the water and in the dunes and vegetation. However, DoD results between TLS derived DSMs and UAS DSMs revealed that the TLS DSMs created in this study contained systematic

errors, notably tilt due to georeferencing and registration issues, so they were not, in this specific case, useful ground truths for comparative analysis to the UAS-SfM DSMs.

A rigorous GCP control network can substantially alleviate bowing effect and reduce z residuals to cm level. In case GCPs are not available, missions that utilize high overlap oblique imagery and also include multi-elevation coverage will also effectively eliminate the doming/bowling effect. This helps improve the geometry of the scene when calculating the internal camera parameters, particularly for solving the radial distortion parameters. If multi-elevation coverage is not an option in some scenarios, the survey missions should try multiple tilt viewing angles off nadir for collecting images. On the other hand, if tilting viewing angles is not technically feasible (especially for fix-wing crafts), attempts should be made to include multiple flight altitudes.

Some autonomous GNSS units geotag erratic height values on images. Although height adjustments to the image geotags prior to SfM processing produces negligible accuracy increase in DSM rendering, this still help reduce time and effort in identifying aerial target locations within the image set.

If the images were taken by the UAS under the PPK/RTK operation mode, a consistent vertical datum should be maintained for the coordinates of both GCPs and image locations throughout the project. In case a survey stretches a long distance without the need of a real-time response, to ensure best SfM processing accuracy, the ellipsoidal height datum is recommended for both image locations and GCPs before converting the vertical datum of the final products to orthometric height. However, if the mission is time critical or the SfM software has the proper geoid model, attempts can be made with orthometric heights directly.

The ability to rapidly process DSM and orthomosaic may be considered essential in oil spill response. The study demonstrated that using rapid processing settings in Metashape may save up to several hours for the specific study area with the cost of product quality and overall accuracy. A systematic shift was observed in a generated orthomosaic using autonomous GNSS geotagged images while a decent spatial resolution and clarity was achieved. Consideration should be made of the balance between time/effort budget and the overall quality of the geospatial products obtained from the SfM processing.

While currently UAS are being used for scouting and general site assessment to great benefit, *survey grade* georeferencing and mapping with UAS-SfM is not performed on a regular basis or part of the prescribed workflow of the SCAT process to the authors knowledge. This study has shown that the integration of knowledge, equipment, and practice of the UAS-SfM remote sensing discipline could have a beneficial impact in terms of cost savings, mapping quality, impact assessment, and resource deployment on SCAT. A few examples are using accurate change detection to quantify sediment removed during a cleanup effort, georeferenced and visual documentation of vegetation health by means of UAS-SfM generated orthomosaics of spill sites, and georeferenced documentation of oiled sediment erosion or deposition via UAS-SfM generated DSMs. For more information, see the document procured in conjunction with this study (Starek et al., 2020).

6.2 Future Work

To improve knowledge on methods for accurate georeferencing of UAS-SfM on sandy beaches it would be valuable to explore more detail into PPK and RTK geotagging methods and how they relate to the survey methods used for the GCP/check point network. For example, performing an aerial target network survey using RTK off of a local base station on a well-

established point, then using an RTK Real Time Network (RTN) to survey the same aerial targets to check for agreement between the two correction methods. Then using that same base station's static log for PPK processing of image locations as well as performing a flight using the RTK RTN to obtain image locations. It would be enlightening to compare the residuals from said flights to the differently obtained target locations. Furthermore, along the same lines, it would be interesting to look at long term repeatability of surveys on the Texas coast to examine the difficulties of being on the edge of the Continuously Operated Reference Station (CORS) network for both RTN and OPUS static solutions and how they apply to georeferencing with the goal of high accuracy change detection using UAS-SfM. Also, the author would like to examine the effects of having moving water with floating foam in the images used for SfM model generation, and how much accuracy is gained, if any, by masking out said water from the images.

REFERENCES

- Abdel-Aziz, Y. I. & Karara, H. M. (2015). Direct linear transformation from comparator coordinates into object space coordinates in close-range photogrammetry. *Photogrammetric Engineering & Remote Sensing*, 81(2), 103-107.
<https://doi.org/10.14358/PERS.81.2.103>
- Anderson, C. M., Mayes, M., & Labelle, R. (2012). *Update of Occurrence Rates for Offshore Oil Spills*. Herndon, VA: Department of the Interior. https://boem-prod.opengov.ibmcloud.com/sites/default/files/uploadedFiles/BOEM/Environmental_Stewardship/Environmental_Assessment/Oil_Spill_Modeling/AndersonMayesLabelle2012.pdf
- Al-Shammari, A., Levin, E., Shults, R. (2018). OIL SPILLS DETECTION BY MEANS OF UAS AND LOW-COST AIRBORNE THERMAL SENSORS. *ISPRS, IV-5*, 293-301.
<https://doi.org/10.5194/isprs-annals-IV-5-293-2018>
- ALTUS Positioning Systems. (2013, June 12). *Altus Positioning System APS-3 surveying specific high precision satellite receiver and communications*. ALTUS Positioning Systems. <http://test.altus-ps.com/aps-3/aps-3.html-0>
- ALTUS Positioning Systems. (2015). *APS-3 user manual, revision 3.0.0*. ALTUS Positioning Systems. <https://kb.unavco.org/kb/file.php?id=796>
- ASPRS. (2014). ASPRS positional accuracy standards for digital geospatial data.
http://www.asprs.org/a/society/committees/standards/Positional_Accuracy_Standards.pdf
- Brasington, J., Langham, J., & Rumsby, B. (2003). Methodological sensitivity of morphometric estimates of coarse fluvial sediment transport. *Geomorphology*, 53(3–4), 299–316.
[https://doi.org/10.1016/S0169-555X\(02\)00320-3](https://doi.org/10.1016/S0169-555X(02)00320-3)

- Carlson. (2016). *Carlson SurvCE reference manual*. Carlson Software.
http://files.carlsonsw.com/mirror/manuals/SurvCE_V5_Manual.pdf
- Carrivick, J. L., Smith, M. W., & Quincey, D. J. (2016). *Structure from motion in the geosciences*. John Wiley & Sons, Ltd. DOI:10.1002/9781118895818
- Chang, A., Jung, J., Maeda, M. M. & Landivar, J. (2017). Crop height monitoring with digital imagery from Unmanned Aerial System (UAS). *Computers and Electronics in Agriculture*, 141, 232-237. <https://doi.org/10.1016/j.compag.2017.07.008>
- Chu, T., Starek, M. J., Brewer, M. J., Murray, S. C., & Pruter, L. S. (2017). Assessing lodging severity over an experimental maize (*zea mays* L.) field using UAS images. *Remote Sensing*, 9(9), 923. <http://dx.doi.org/10.3390/rs9090923>
- DJI. (n.d.). *Phantom 4 Pro – Specs, Tutorials & Guides – DJI*. Retrieved October 8, 2019, from <https://www.dji.com/phantom-4-pro/info>
- Fazeli, H., Samadzadegan, F., & Dadrasjavan, F. (2016). Evaluating the potential of RTK-UAV for automatic point cloud generation in 3D rapid mapping. *International Archives of the Photogrammetry, Remote Sensing and Spatial Information Sciences - ISPRS Archives*, 41(July), 221–226. <https://doi.org/10.5194/isprsarchives-XLI-B6-221-2016>
- Fonstad, M. A., Dietrich, J. T., Courville, B. C., Jensen, J. L., & Carbonneau, P. E. (2013). Topographic structure from motion: A new development in photogrammetric measurement. *Earth Surface Processes and Landforms*, 38(4), 421–430.
<https://doi.org/10.1002/esp.3366>
- Furukawa, Y., & Ponce, J. (2010). Accurate, dense, and robust multiview stereopsis. *IEEE Transactions on Pattern Analysis and Machine Intelligence*, 32(8), 1362-1376.
DOI:10.1109/TPAMI.2009.161

- Gindraux, S., Boesch, R., & Farinotti, D. (2017). Accuracy assessment of digital surface models from unmanned aerial vehicles' imagery on glaciers. *Remote Sensing*, 9(2), 186.
<https://doi.org/10.3390/rs9020186>
- Greenwood, F. (2015). Mapping in practice. In Kakaes, K., Greenwood, F., Lippincott, M., Meier, P., & Wich, S. (Eds.), *Drones and aerial observation: New technologies for property rights, human rights, and global development* (pp. 49-55). New America.
<http://drones.newamerica.org/primer/DronesAndAerialObservation.pdf>
- Hayakawa, Y.S., Obanawa, H. (2020). Volumetric Change Detection in Bedrock Coastal Cliffs Using Terrestrial Laser Scanning and UAS-Based SfM. *Sensors*, 20(12), 3403.
<https://doi.org/10.3390/s20123403>
- Hartley, R. I. & Sturm, P. (1997). Triangulation. *Computer Vision and Image Understanding*, 68(2), 146-157. <https://doi.org/10.1006/cviu.1997.0547>
- James, M. R. & Robson, S. (2012). Straightforward reconstruction of 3D surfaces and topography with a camera: Accuracy and geoscience application. *Journal of Geophysical Research: Earth Surface*, 117(F3). <https://doi.org/10.1029/2011JF002289>
- James, M. R. & Robson, S. (2014). Mitigating systematic error in topographic models derived from UAV and ground-based image networks. *Earth Surface Processes and Landforms*, 39(10), 1413–1420. <https://doi.org/10.1002/esp.3609>
- James, M. R., Robson, S., & Smith, M. W. (2017). 3-D uncertainty-based topographic change detection with structure-from-motion photogrammetry: Precision maps for ground control and directly georeferenced surveys. *Earth Surface Processes and Landforms*, 42(12), 1769–1788. <https://doi.org/10.1002/esp.4125>

- Javernick, L., Brasington, J., & Caruso, B. (2014). Modeling the topography of shallow braided rivers using structure-from-motion photogrammetry. *Geomorphology*, 213, 166–182.
<https://doi.org/10.1016/j.geomorph.2014.01.006>
- Jiao, Z., Jia, G., Cai, Y. (2019). A new approach to oil spill detection that combines deep learning with unmanned aerial vehicles. *Computers & Industrial Engineering*, 135, 1300-1311. <https://doi.org/10.1016/j.cie.2018.11.008>
- Leica. (n.d.). *Leica CS10/CS15 user manual, version 5.0*. Retrieved November 21, 2021 from https://www.surveyequipment.com/PDFs/Leica_Viva_CS10_CS15_User_Manual.pdf
- Longuet-Higgins, H. C. (1981). A computer algorithm for reconstructing a scene from two projections. *Nature*, 293, 133-135.
- Lowe, D. G. (2004). Distinctive image features from scale-invariant keypoints. *International Journal of Computer Vision*, 60(2), 91–110.
<https://doi.org/10.1023/B:VISI.0000029664.99615.94>
- Odonkor, P., Ball, Z., Chowdhury, S. (2019). Distributed operation of collaborating unmanned aerial vehicles for time-sensitive oil spill mapping. *Swarm and Evolutionary Computation*, 46, 52-68. <https://doi.org/10.1016/j.swevo.2019.01.005>
- Mitasova, H., Hardin, E., Starek, M. J., Harmon, R. S., Overton, M. F., & Carolina, N. (2011). *Landscape dynamics from LiDAR data time series* [Paper presentation].
Geomorphometry, Redlands, CA.
<https://geospatial.ncsu.edu/geoforall/publications/Mitasova2011geomorphometry.pdf>
- NOAA. (2013). *Shoreline Assessment Manual*. 4th Edition. U.S. Dept. of Commerce. Seattle, WA: Emergency Response Division, Office of Response and Restoration, National Oceanic and Atmospheric Administration. 73 pp + appendices.

- NOAA, Office of Response and Restoration. (2021, March 2). *Shoreline Cleanup and Assessment Technique (SCAT)*. <https://response.restoration.noaa.gov/oil-and-chemical-spills/oil-spills/resources/shoreline-cleanup-and-assessment-technique-scat.html>
- NOAA, (2021, November, 25). VERTICAL DATUM TRANSFORMATION. NOAA. <https://vdatum.noaa.gov/>
- Riegl. (2017). *Riegl VZ-400*. Retrieved November 20, 2021, from http://www.riegl.com/International_uploads/tx_pxriegldownloads/10_DataSheet_VZ-400_2017-06-14.pdf
- Ryan, J. C., Hubbard, A. L., Box, J. E., Todd, J., Christoffersen, P., Carr, J. R., Holt, T. O., & Snooke, N. (2015). UAV photogrammetry and structure from motion to assess calving dynamics at Store Glacier, a large outlet draining the Greenland ice sheet. *The Cryosphere*, 9(1), 1–11. <https://doi.org/10.5194/tc-9-1-2015>
- Sanz-Ablanedo, E., Chandler, J. H., Rodriguez-Perez, J. R., & Ordonez, C. (2018). Accuracy of unmanned aerial vehicle (UAV) and SfM photogrammetry survey as a function of the number and location of ground control points used. *Remote Sensing*, 10(10), 1606. <https://doi.org/10.3390/rs10101606>
- Schwind, M. (2016). Comparing and characterizing three-dimensional point clouds derived from structure from motion photogrammetry. [Master's thesis]. Texas A&M University – Corpus Christi.
- Seitz, S. M., Curless, B., Diebel, J., Scharstein, D., & Szeliski, R. (2006). A comparison and evaluation of multi-view stereo reconstruction algorithms. *2006 IEEE Computer Society Conference on Computer Vision and Pattern Recognition - Volume 1 (CVPR'06)*, 1, 519–528. <https://doi.org/10.1109/CVPR.2006.19>

- SenseFly. (n.d.) *eBee PLUS*. Retrieved November 20, 2021 from
<https://optron.com/sensefly/products/ebee-plus/>
- Slocum, R. K. & Parrish, C. E. (2017). Simulated imagery rendering workflow for UAS-based photogrammetric 3D reconstruction accuracy assessments. *Remote Sensing*, 9(4), 396.
DOI:10.3390/rs9040396
- Slocum, R. K., Wright, W., Parrish, C., Costa, B., Sharr, M., & Battista, T. A. (2019). Guidelines for bathymetric mapping and orthoimage generation using sUAS and SfM, an approach for conducting nearshore coastal mapping. *NOAA Technical Memorandum NOS NCCOS*, 265. <https://doi.org/10.25923/07mx-1f93>
- Snaveley, N., Seitz, S. M., & Szeliski, R. (2008). Modeling the world from internet photo collections. *International Journal of Computer Vision*, 80(2), 189–210.
<https://doi.org/10.1007/s11263-007-0107-3>
- Stanton, C., Starek, M. J., Elliott, N. C., Brewer, M. J., Maeda, M., & Chu, T. (2017). Unmanned aircraft system-derived crop height and normalized difference vegetation index metrics for sorghum yield and aphid stress assessment. *Journal of Applied Remote Sensing*, 11.
DOI:10.1117/1.JRS.11.026035
- Starek, M. J., Mitasova, H., Hardin, E., Weaver, K., Overton, M., & Harmon, R. S. (2011). Modeling and analysis of landscape evolution using airborne, terrestrial, and laboratory laser scanning. *Geosphere*, 7(6), 1340-1356. <https://doi.org/10.1130/GES00699.1>
- Starek, M. J., Davis, T., Prouty, D., & Berryhill, J. (2014). Small-scale UAS for geoinformatics applications on an island campus. In *Ubiquitous Positioning Indoor Navigation and Location Based Service (UPINLBS)* (pp. 120-127).
<http://dx.doi.org/10.1109/UPINLBS.2014.7033718>

- Starek, M. J., Gingras, M., & Jeffress, G. (2019). Application of unmanned aircraft systems for coastal mapping and resiliency. In Rajabifard, A. (Ed.), *Sustainable development goals connectivity dilemma: Land and geospatial information for urban and rural resilience* (p.109). CRC Press. <https://doi.org/10.1201/9780429290626>
- Starek, M.J., Berryhill, J.B., (2020). Guidelines and considerations for Surveying of Oil spill Events on Sandy Beaches with UAS. (TGLO Technical Report, Contract No. 18-140-000-A683)
- Stretcha, C., Olivier, K., & Pascal, F. (2012, February 8). Automatic mapping from ultra-light UAV imagery. [Conference session]. EuroCOW, Barcelona, Spain.
- Szeliski, R. (2011). *Computer vision: Algorithms and applications*. Springer Science & Business Media.
- Thompson, A. (2010, April 23). *FAQ: The Science and History of Oil Spills*. Live Science. <https://www.livescience.com/9885-faq-science-history-oil-spills.html>
- Tjalling, D. H., Nijland, W., McArdell, B. W., Kalthof, M. W. (2021). Case Report: Optimization of Topographic Change Detection with UAV Structure-From-Motion Photogrammetry Through Survey Co-Alignment. *Frontiers in Remote Sensing*, (24). <https://doi.org/10.3389/frsen.2021.626810>
- Tournadre, V., Pierrot-Deseilligny, M., & Faure, P. H. (2015). UAV linear photogrammetry. *ISPRS - International Archives of the Photogrammetry, Remote Sensing and Spatial Information Sciences, XL-3/W3*, 327–333. <https://doi.org/10.5194/isprsarchives-XL-3-W3-327-2015>
- Triggs, B., McLauchlan, P. F., Hartley, R. I., & Fitzgibbon, A. W. (2000). Bundle adjustment—a modern synthesis. In B. Triggs, A. Zisserman, & R. Szeliski (Eds.), *Vision algorithms:*

- Theory and practice* (Vol. 1883, pp. 298–372). Springer Berlin Heidelberg.
https://doi.org/10.1007/3-540-44480-7_21
- Turner, D., Lucieer, A., & Wallace, L. (2014). Direct georeferencing of ultrahigh-resolution UAV imagery. *IEEE Transactions on Geoscience and Remote Sensing*, 52(5), 2738–2745. <https://doi.org/10.1109/TGRS.2013.2265295>
- Ullman, S. (1979). The interpretation of structure from motion. *Proceedings of the Royal Society of London*, 203(1153), 405-426. DOI:10.1098/rspb.1979.0006
- U.S. Energy Information Administration (EIA). (2021, September 7) Frequently Asked Questions - How much oil is consumed in the United States?
<https://www.eia.gov/tools/faqs/faq.php?id=33&t=6>
- USGS. (2017). Unmanned aircraft systems data post-processing: Structure-from-motion photogrammetry. Retrieved November 30, 2019 from
<https://uas.usgs.gov/nupo/pdf/PhotoScanProcessingDSLRLMar2017.pdf>
- USGS. (2017). National Unmanned Aircraft Systems (UAS) Project Office processing UAS imagery using Agisoft Photoscan. USGS National UAS Project Office. Retrieved November 30, 2019 from
<https://uas.usgs.gov/nupo/pdf/BauerPhotoscanNASAMarch2017.pdf>
- Wackrow, R. & Chandler, J. H. (2011). Minimising systematic error surfaces in digital elevation models using oblique convergent imagery. *The Photogrammetric Record*, 26(133), 16–31. <https://doi.org/10.1111/j.1477-9730.2011.00623.x>
- Westoby, M. J., Brasington, J., Gasser, N. F., Hambrey, M. J., & Reynolds, J. M. (2012). ‘Structure-from-Motion’ photogrammetry: A low-cost, effective tool for geoscience

- applications. *Geomorphology*, 179, 300-314.
<https://doi.org/10.1016/j.geomorph.2012.08.021>
- Wheaton, J. M., Brasington, J., Darby, S. E., & Sear, D. A. (2009). Accounting for uncertainty in DEMs from repeat topographic surveys: Improved sediment budgets. *Earth Surface Processes and Landforms*, 35(2), 136-156. <https://doi.org/10.1002/esp.1886>
- Wu, C. (2014). Critical configurations for radial distortion self-calibration. *2014 IEEE Conference on Computer Vision and Pattern Recognition*, 25–32.
<https://doi.org/10.1109/CVPR.2014.11>
- Zach, C. (2014). Robust bundle adjustment revisited. In Fleet, D., Pajdla, T., Schiele, B., & Tuytelaars, T. (Eds.), *Computer vision – ECCV 2014. Lecture notes in computer science* (Vol. 8693, pp. 772-787). Springer. https://doi.org/10.1007/978-3-319-10602-1_50
- Zarco-Tejada, P. J., Diaz-Varela, R., Angileri, V., & Loudjani, P. (2014). Tree height quantification using very high resolution imagery acquired from an unmanned aerial vehicle (UAV) and automatic 3D photo-reconstruction methods. *European Journal of Agronomy*, 55, 89-99. <https://doi.org/10.1016/j.eja.2014.01.004>

End Lap: 80%

Predicted GSD: 0.6 cm/px

UAS: DJI Phantom 4 Pro

Image Georeferencing Method: Autonomous GNSS

Flight Control Software: Ground Station Pro

Visibility: Clear

Winds: 15 kts onshore

Notes: The sun was getting low making long shadows

1.1.2 02/12/2018

02/12/2018 – This flight covered the entire test area from the jetties to the access road. Two craft were flown, the DJI Phantom 4 Pro and the eBee Plus. A control network of 10 targets was laid out and surveyed with a survey grade GNSS. There were two main goals for this day. Goal one was to examine the feasibility of surveying the entire 3.2 km stretch with one person, as in how many targets could be set and how many flights could be performed in one day. This involved getting a feel for the economy of the process by evaluating the number of batteries required to map the entire beach with both craft at the highest resolution feasible. The second main goal for the day was to acquire accurately georeferenced topographical data of the test site for use in change detection evaluation from both a fixed wing and rotor craft. The rotor craft mission consisted of three flights or batteries and captured 985 images. The fixed wing mission consisted of three flights or batteries and captured 563 images. In performing the survey, the targets were laid out in pairs using a vehicle and a handheld GNSS to determine five roughly equal intervals along the 3.2 km study site. The GCP's locations were measured using the survey grade GNSS at

this time. Next the flights were flown, the fixed wing first then the rotor craft. After the flights, the targets were collected by vehicle.

A problem did arise during this survey. The ground control points located at the south end of the study site were moved by beach goers, leaving no control at that end of the survey. This created problems with processing as can be seen later. But being a lesson learned, a method was developed that prevented disturbance of targets during future surveys.

Flight Properties eBee Plus:

Coverage: the 3.2 km between fish pass and Access Road No 2

Number of flights/batteries: 3

Number of images collected: 563

Flight time: 10:15 am to 12:30 pm

Altitude: 70 meters ATO in flight control software

Side Lap: 80%

End Lap: Max achievable 60% - 70%

Predicted GSD: 1.6 cm\px

UAS: eBee Plus

Image Georeferencing Method: Autonomous GNSS

Flight Control Software: Emotion 3

Visibility: 10 nm/Clear

Winds: 15kts NNE Side Shore

Notes: Flights went well no problems

Flight Properties DJI Phantom 4 Pro:

Coverage: the 3.2 km between fish pass and Access Road No 2

Number of flights/batteries: 3

Number of images collected: 985

Camera orientation: Nadir

Flight time: 1:00 pm to 2:00 pm

Altitude: 70 meters ATO in flight control software

Side Lap: 80%

End Lap: 80%

Predicted GSD: 1.6 cm\px

UAS: DJI Phantom 4 Pro

Image Georeferencing Method: Autonomous GNSS

Flight Control Software: Ground Station Pro

Visibility: 10 nm/Clear

Winds: 7kts N Side Offshore

Notes: Smooth flights no issues

Control Network Details

Number of GCPs: 10

Geometry: Equal interval pairs

1.1.3 06/14/2018

06/14/2018 – There were three primary goals of this field day. The first goal was to collect data that would allow the comparison of UAS generated DSMs to GNSS collected point elevation data. This allowed comparison of Z residuals acquired from check points and GNSS topo points. The second main goal for the day was to acquire accurately georeferenced topographical data of the entire 3.2 km test site for use in change detection evaluation from both a fixed wing and rotor craft. The third main goal of the survey was to acquire video of the test site via the rotorcraft for exploration of its use in rapid mapping. Two aircraft were flown, the eBee Plus and the DJI Phantom 4 pro. A control network of 22 targets was laid out and surveyed with the survey grade GNSS. And additional 22 bare earth topo points were collected throughout the test area.

The rotorcraft mission consisted of three flights for acquiring still images that took place between 11:30 am and 12:35 pm, taking 976 images, and one flight for acquiring video that took place between 12:40 pm and 12:55 pm. The fixed wing mission consisted of one flight and took place between 1:05 pm and 1:50 pm and acquired 408 images.

In performing the survey, the targets were laid out in pairs at equal intervals from a vehicle using a handheld GPS. Next the rotorcraft was flown acquiring still images, then the fixed wing was flown, and finally the rotor craft video flight was performed. After the flights, the Survey grade GNSS was used to measure the aerial target locations and collect topo points, all while picking up the targets.

To prevent beach goers from disturbing the painted plywood targets, lathes were driven through each target's handle hole and tied with pink survey flagging. This seemed to work and prevented the targets from being disturbed by humans. However, one of the targets was disturbed by a wave as the tide came up making it unusable.

Flight Properties eBee Plus:

Coverage: the 3.2 km between fish pass and Access Road No 2

Number of flights/batteries: 1

Number of images collected: 408

Flight time: 1:05 am to 1:50 pm

Altitude: 118.6 meters ATO in flight control software

Side Lap: 85%

End Lap: Max achievable 60% - 70%

Predicted GSD: 2.8 cm\px

UAS: eBee Plus

Image Georeferencing Method: Autonomous GNSS

Flight Control Software: Emotion 3

Visibility: 10 nm/Clear

Winds: 12kts ESE Onshore

Notes: Flights went well no problems

Flight Properties DJI Phantom 4 Pro:

Coverage: the 3.2 km between fish pass and Access Road No 2

Number of flights/batteries: 3

Number of images collected: 985

Camera orientation: Nadir

Flight time: 11:30 pm to 12:35 pm

Altitude: 100 ATO meters in flight control software

Side Lap: 80%

End Lap: 80%

Predicted GSD: 2.53 cm\px

UAS: DJI Phantom 4 Pro

Image Georeferencing Method: Autonomous GNSS

Flight Control Software: Ground Station Pro

Visibility: 10 nm/Clear

Winds: 11kts SE Side Onshore

Notes: Smooth flights no issues

Control Network Details

Number of GCPs: 22 planned, 21 actual

Geometry: Equal interval pairs with addition of 22 topo points

1.1.4 08/15-17/2018

08/15-17/2018 – This series of field days consisted of multiple flights over three consecutive days. The second day 8/16/18 is included as a quarterly flight for change detection evaluation. The three-day experiment phase of the study took place over the Southern 1.6 km of the study area. It involved rigorous ground truthing, utilizing a high number of aerial targets, 32, as GCPs and check points. The full three-day trial will be discussed in full detail later, the parts that pertain to its inclusion as a quarterly flight will be discussed here.

Two aircraft were flown, the eBee Plus and the DJI Phantom 4 Pro. Twenty-two targets were utilized as GCPs and were laid out in 11 pairs at equal intervals. The survey also utilized 10 aerial targets used as check points that were laid out singly at equal intervals between the GCP pairs. The DJI Phantom 4 Pro mission was comprised of 3 flights. Flight one was flown at 25 meters and captured 410 images. Flight 2 was flown at 45 meters and captured 149 images, this flight design captured images at an angle of 15° above nadir and was performed with the camera facing the shore so that the wider width of the image was parallel to the features of the dune faces and water line. Flight 3 was flown at 70 meters and captured 193 images. All three rotorcraft flights took place between 10:45 am and 11:50 am. The eBee plus flight took place between 1:00 pm and 2:00 pm, was flown at 90 meters and captured 240 images. The image locations were determined using Post Process Kinetic GNSS and are more accurate than the previous autonomous positions obtained from the eBee Plus.

In performing the survey, the targets were laid out in the morning, then measured and retrieved at the end of the day. The aerial targets were laid out at equal intervals of 50 meters throughout the 1.6 km test area. The targets were staggered between pairs and singles, with the pairs used as GCPs and the singles used as check points. The flights were flown in the late morning and early afternoon amongst the other work for the three-day experiment.

Flight Properties eBee Plus: Day 2

Coverage: The Southern 1.6 km of the test area, the 1.6 km North of the fish pass jetties

Number of flights/batteries: 1

Number of images collected: 240

Flight time: 1:00 pm to 2:00 pm

Altitude: 85 meters ATO in flight control software

Side Lap: 85%

End Lap: Max achievable 60% - 70%

Predicted GSD: 2.0 cm\px

UAS: eBee Plus RTK/PPK

Image Georeferencing Method: Post Process Kinetic (PPK) GNSS

Flight Control Software: Emotion 3

Visibility: 10 nm/Clear

Winds: 12kts SSE Side-Onshore

Notes: Flights went well no problems

Flight Properties DJI Phantom 4 Pro: Day 2

Coverage: The Southern 1.6 km of the test area, the 1.6 km North of the fish pass jetties

Number of flights/batteries: 1

Number of images collected: 405

Camera orientation: Nadir,

Flight time: 12:20 pm to 12:40 pm

Altitude: 50 meters ATO in flight control software

Side Lap: 80%

End Lap: 80%

Predicted GSD: 1.4 cm\px

UAS: DJI Phantom 4 Pro

Image Georeferencing Method: Autonomous GNSS

Flight Control Software: Ground Station Pro

Visibility: 10 nm/Clear

Winds: 11kts SE Side Onshore

Notes: Smooth flights no issues

Control Network Details

Number of GCPs: 22 GCPs and 10 check points

Geometry: Equal interval pairs for the GCPs every 100 meters with single aerial targets in between pairs.

1.1.5 12/17/2018

12/17/2018 – The primary goal of this flight was to examine ways to reduce the doming/bowl effect. The study area was divided into halves, Northern and Southern, for the missions. The craft flown was the DJI Phantom 4 Pro capturing 1,714 images in 5 flights. The flights were divided into 6 missions spread across multiple batteries.

The goal for the Northern half of the study area was to test how the angle of image capture affects the ability to solve the camera parameters. Three missions were flown at the same elevation and overlap but with different amounts of obliqueness. One mission was flown at nadir, looking straight down, one mission flown at 10° above nadir, and one mission flown at 15° above nadir. An additional mission was flown above these at nadir and with an intended 25% greater GSD.

The goal for the Southern half was capture data with a small ground sample distance of 0.5 cm/px as well as the same 1 cm/px as the Northern half. Both flights were flown at 10° above nadir in order to prevent the bowing/oming effect.

Flight Properties of DJI Phantom 4 Pro

A control network of 14 Targets were laid out in equal interval pairs with survey lathes and tape to prevent tampering. The flights were performed then the targets were measured and retrieved.

Flight/battery 1: 11:21 am to 11:55 am Total 208 images

Mission 1: 208 images, 0408 – 0625, 20 meters ATO, 10° above nadir, 0.5 cm/px, Southern half, side lap: 80%, end lap: 80%

Flight/battery 2: 12:25 pm to 12:50 pm Total 493 images

Mission 1: 493 images 0626 – 0120, 20 meters ATO, 10° above nadir, 0.5 cm/px, Southern half, side lap: 80%, end lap: 80%

Flight/battery 3: 1:00 pm to 1:20 pm Total 334

Mission 2: 334 images 0122 – 0455, 40 meters ATO, 10° above nadir, 1 cm/px, Southern half, side lap: 80%, end lap: 80%

Flight/battery 4: 1:25 pm to 1:47 pm Total 512 images

Mission 3: 260 images 0456 – 0715, 40 meters ATO, 10° above nadir 1 cm/px, Northern half, side lap: 80%, end lap: 80%

Mission 4: 252 images 0716 – 0967, 40 meters ATO, 15° above nadir 1 cm/px, Northern half, side lap: 80%, end lap: 80%

Flight/battery 5: 1:52 pm – 2:17 pm Total 436 images

Mission 5: 267 images 0968 – 0237 40 meters ATO nadir 1 cm/px, Northern half, side lap: 80%, end lap: 80%

Mission/battery 6: 165 images 0238 – 0404 55 meters ATO nadir 1.25 cm/px, Northern half, side lap: 80%, end lap: 80%

Image Georeferencing Method: Autonomous GNSS

Flight Control Software: Ground Station Pro

Visibility: 10 nm/Clear

Winds: calm 2 to 5 kts and variable

Notes: Smooth flights no issues

1.1.6 02/04/2019

02/04/2019 – This field day utilized a group of undergrads that were using the data collected for a project. This allowed the collection of much more ground truth than was possible previously.

Twenty-Six aerial targets and 264 topo points, including twelve profiles were collected in the

study area. This presented an opportunity to examine general accuracies in more detail than with other quarterly flights. Due to the amount of groundwork being done only the Southern half of the study area was surveyed. The weather was cool but very calm with winds nonexistent. While this allowed for efficient use of flight batteries, a sea fog was present, limiting visibility. With the limited visibility, observers were stationed along the beach to keep constant eyes on the UAS. The fog also allowed examination of its effects on camera calibration and survey accuracy. Four flights/batteries were used to gather a total of 1657 images. The mission plan was one large block designed to acquire five legs along the entirety of the flight area and more at the Southern end near the jetties. The mission utilized 80% end lap and 80% side lap. The target altitude was 30 meters ATO giving a GSD of approximately 0.8 cm/px.

Flight Properties:

Coverage: The Southern 1.6 km of the test area, the 1.6 km North of the fish pass jetties

Number of flights/batteries: 4

Number of images collected: 1657

Camera orientation: Nadir, 5° above Nadir

Flight time: 1:00 pm to 2:40 pm

Altitude: 30 meters ATO in flight control software

Side Lap: 80%

End Lap: 80%

Predicted GSD: 0.8 cm\px

UAS: DJI Phantom 4 Pro

Image Georeferencing Method: Autonomous GNSS

Flight Control Software: Ground Station Pro

Visibility: < 1 nm, foggy

Winds: 0 kts dead calm

Notes: Smooth flights no issues

1.2 Three-day field experiment and GNSS corrections used

1.2.1 Field work/data collection

The three-day experiment phase of the project took place over the course of August 15th through August 17th, 2018. The goal was to collect a large number of aerial images and ground truthing data for use in examining the effects of differentially corrected GNSS image locations versus autonomous GNSS image locations for use in SfM-MVS DSM generation and their subsequent use for change detection. The main aircraft utilized was the eBee Plus RTK/PPK. This system provides the ability to post process corrections of its image locations autonomously acquired image locations via a Post Process Kinetic workflow. This allows the ability to have both a set of autonomous image locations and differentially corrected image locations for the same set of imagery. This is useful for controlling an experiment of comparing the accuracies of products made from each location acquisition method as the only difference during processing is the image locations and accuracies. The autonomously gained locations have accuracies near 5 to 10 meters while the PPK corrected locations have accuracies near 1 to 3 centimeters.

An extensive aerial target control network was laid out and surveyed in each day utilizing the targets described in section 4.1.3 and shown below in Figure 67, Figure 68, and Figure 69. The GNSS work for the target location measurements was done using a local base station. On

8/13/2018, two days before the experiment, in order to maintain continuity of corrections for the three days, a one-and-a-half-foot long half inch iron rod was set into the sand of the beach near the fore dune line in the center of the southern half of the study area. A hole was dug about a foot deep, a six-inch-long two inch by two inch wooden grade stake was driven into the bottom of the hole. The iron rod was then driven into the top of the grade stake forcing it further into the ground until the top of the iron rod was roughly even with the top of the hole. Three one inch by two inch ten-inch-long wooden stakes were then driven into the ground adjacent to the grade stake and iron rod forming roughly a triangular shaped support. The hole was then filled, and the sand thoroughly tamped until hard using a shovel and boots. The stakes were used to decrease the likelihood of the iron rod sinking or shifting during the duration of its use. The sand at the base of the hole where the stakes were driven was hard and firm making the stakes difficult to drive. The altus GNSS antenna was set up on a 2 meter fixed height tripod, leveled and left to log static for 5 hours and 31 minutes. The static observation was uploaded to the NGS run Online Positioning User Service (OPUS).

The returned rapid ephemeris position was entered into the data collector and used as the point location for broadcasting corrections from the subsequently set up base stations occupying the iron rod each of the three field days. The NAD83(2011) UTM 14N meters Horizontal projected coordinate system and NAD83(2011) ellipsoidal Vertical heights were chosen for use for the three days. Since the eBee plus RTK/PPK collects ellipsoidal altitudes, it was decided to examine this data without using an orthometric datum to prevent any errors in conversion of the image locations. It is possible to convert any generated products to a chosen vertical datum.

Each of day the base station was set up on a 2 meter fixed height tripod and used to broadcast corrections to the rover unit while measuring target positions. The second purpose of

the base station was to log static data while on and broadcasting corrections. It is important that static is being logged throughout the duration of the eBee plus flight as it is used to calculate the final corrected positions.

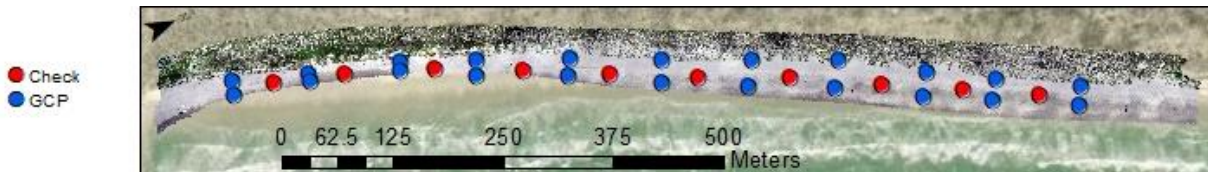


Figure 67. The aerial target network and Orthomosaic from Day 1, August 15th, showing the control geometry used that gave the lowest residuals on the check points.

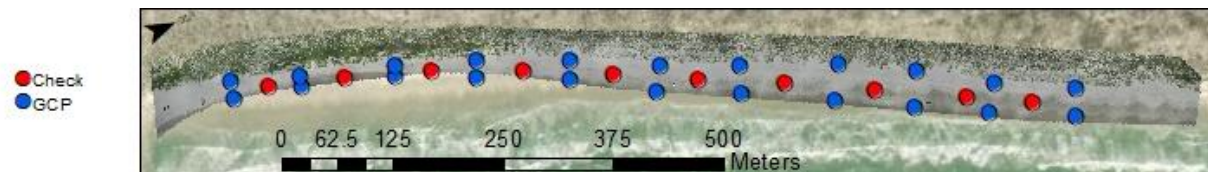


Figure 68. The aerial target network and Orthomosaic from Day 2, August 16th, showing the control geometry used that gave the lowest residuals on the check points.

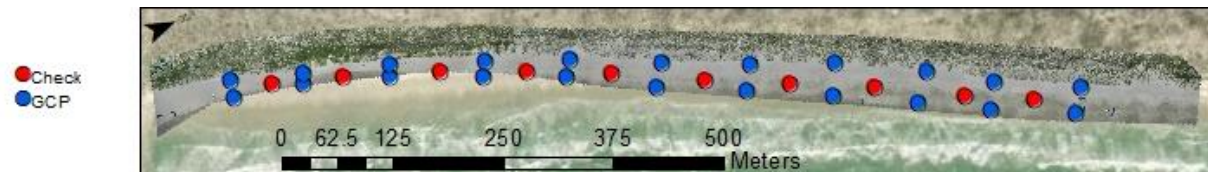


Figure 69. The aerial target network and Orthomosaic from Day 3, August 17th, showing the control geometry used that gave the lowest residuals on the check points.

On all three days a Terrestrial Laser Scanner (TLS) was implemented to gain further ground truth data. Two scan positions were utilized that captured a point cloud of the middle section of the test area. The TLS was georeferenced by a set of tripod mounted reflective targets, eight per day, that were set up and surveyed in along with the aerial targets. The TLS control network can be seen below in Figure 70, Figure 71, and Figure 72.

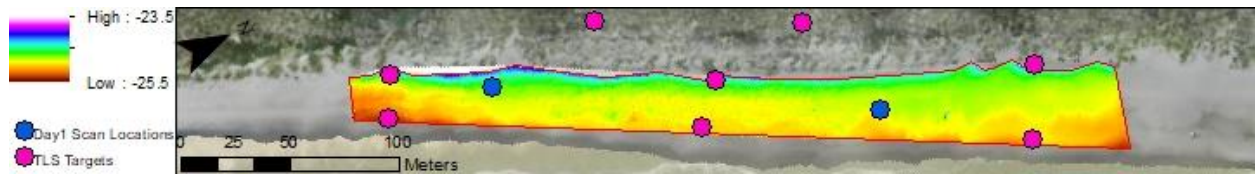


Figure 70. Day 1 8/15/2018 scanner locations and control target network for the TLS overlaid on a clipped DSM created from the TLS data.

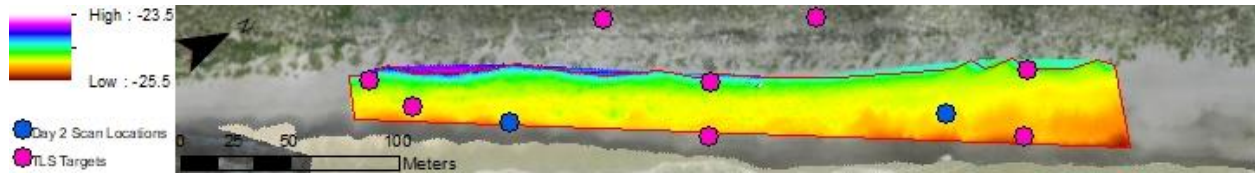


Figure 71. Day 2 8/16/2018 scanner locations and control target network for the TLS overlaid on a clipped DSM created from the TLS data.

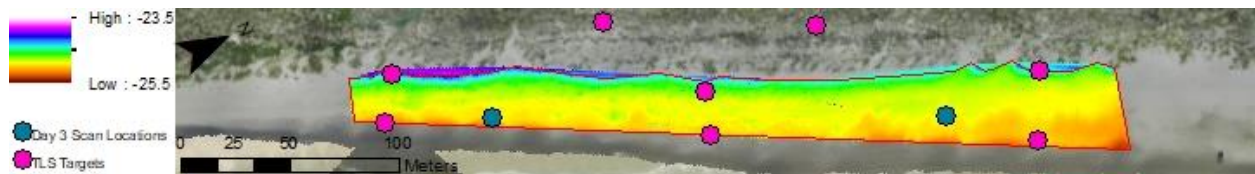


Figure 72. Day 3 8/17/2018 scanner locations and control target network for the TLS overlaid on a clipped DSM created from the TLS data.

Day 1: 8/15/2018:

Flight Properties DJI Phantom 4 Pro:

Coverage: The Southern 1.6 km of the test area, the 1.6 km North of the fish pass jetties

Number of flights/batteries: 1

Number of images collected: 405

Camera orientation: Nadir,

Flight time: 12:20 pm to 12:40 pm

Altitude: 50 meters ATO in flight control software

Side Lap: 80%

End Lap: 80%

Predicted GSD: 1.4 cm\px

UAS: DJI Phantom 4 Pro

Image Georeferencing Method: Autonomous GNSS

Flight Control Software: Ground Station Pro

Visibility: 10 nm/Clear

Winds: 11kts SE Side Onshore

Notes: Smooth flights no issues

Flight Properties eBee Plus RTK/PPK:

Coverage: The Southern 1.6 km of the test area, the 1.6 km North of the fish pass jetties

Number of flights/batteries: 1

Number of images collected: 223

Flight time: 11:15 am to 11:55 am

Altitude: 90 meters ATO in flight control software

Side Lap: 85%

End Lap: Max achievable 60% - 70%

Predicted GSD: 2.0 cm\px

UAS: eBee Plus RTK/PPK

Image Georeferencing Method: Post Process Kinetic (PPK) GNSS

Flight Control Software: Emotion 3

Visibility: 10 nm/Clear

Winds: 15kts SSE Side-Onshore

Notes: Flights went well no problems

Day 2: 8/16/2018:

Flight Properties DJI Phantom 4 Pro: Day 2

Coverage: The Southern 1.6 km of the test area, the 1.6 km North of the fish pass jetties

Number of flights/batteries: 3

Flight/battery 1:

Number of images collected: 410

Camera orientation: Nadir

Flight time: 10:50 am to 11:05 am

Altitude: 70 meters ATO in flight control software

Side Lap: 80%

End Lap: 80%

Predicted GSD: 1.9 cm\px

UAS: DJI Phantom 4 Pro

Image Georeferencing Method: Autonomous GNSS

Flight Control Software: Ground Station Pro

Visibility: 10 nm/Clear

Winds: 11kts SSE Side-Onshore

Notes: Smooth flights no issues

Flight/battery 2:

Number of images collected: 149

Camera orientation: 15° above nadir

Flight time: 11:25 am to 11:35 am

Altitude: 90 meters ATO in flight control software

Side Lap: 80%

End Lap: 80%

Predicted GSD: 2.5 cm\px

UAS: DJI Phantom 4 Pro

Image Georeferencing Method: Autonomous GNSS

Flight Control Software: Ground Station Pro

Visibility: 10 nm/Clear

Winds: 12kts SSE Side-Onshore

Notes: Smooth flights no issues

Flight/battery 3:

Number of images collected: 192

Camera orientation: nadir

Flight time: 11:40 am to 11:50 am

Altitude: 110 meters ATO in flight control software

Side Lap: 80%

End Lap: 80%

Predicted GSD: 3.0 cm\px

UAS: DJI Phantom 4 Pro

Image Georeferencing Method: Autonomous GNSS

Flight Control Software: Ground Station Pro

Visibility: 10 nm/Clear

Winds: 14kts SSE Side-Onshore

Notes: Smooth flights no issues

Flight Properties eBee Plus RTK/PPK: Day 2

Coverage: The Southern 1.6 km of the test area, the 1.6 km North of the fish pass jetties

Number of flights/batteries: 1

Number of images collected: 240

Flight time: 1:00 pm to 2:00 pm

Altitude: 85 meters ATO in flight control software

Side Lap: 85%

End Lap: Max achievable 60% - 70%

Predicted GSD: 2.0 cm\px

UAS: eBee Plus RTK/PPK

Image Georeferencing Method: Post Process Kinetic (PPK) GNSS

Flight Control Software: Emotion 3

Visibility: 10 nm/Clear

Winds: 12kts SSE Side-Onshore

Notes: Flights went well no problems

Flight Properties eBee Plus RTK/PPK: Day 3

Coverage: The Southern 1.6 km of the test area, the 1.6 km North of the fish pass jetties

Number of flights/batteries: 1

Number of images collected: 241

Flight time: 11:00 am to 12:00 pm

Altitude: 85 meters ATO in flight control software

Side Lap: 85%

End Lap: Max achievable 60% - 70%

Predicted GSD: 2.0 cm/px

UAS: eBee Plus RTK/PPK

Image Georeferencing Method: Post Process Kinetic (PPK) GNSS

Flight Control Software: Emotion 3

Visibility: 10 nm/Clear

Winds: 10 kts SSE Side-Onshore

Notes: Flights went well no problems

APPENDIX 2

Cover Page of Best Practices Guidelines Created for the TGLO in Conjunction with Writing this Thesis

Technical Report
Guidelines and Considerations for Surveying of Oil Spill Events
on Sandy Beaches with UAS



Prepared for:

Mr. Steve Buschang
Director of Research and Development
State Scientific Support Coordinator
Texas General Land Office

GLO Project Contract Number: 18-140-000-A683



Acknowledgement

The views, statements, findings, conclusions and recommendations expressed herein are those of the author(s) and do not necessarily reflect the views of the Texas General Land Office (TGLO).

Document Preparation

Authors

Michael J. Starek¹, Ph.D., Jacob Berryhill²

¹Associate Professor of Geospatial Systems Engineering

²Graduate Research Assistant

Texas A&M University-Corpus Christi

Measurement Analytics Lab (MANTIS)

Conrad Blucher Institute for Surveying and Science

Contact

6300 Ocean Drive, Unit 5799, Corpus Christi, TX 78412

Ph: 361-825-3978, Fax: 361-825-5848

Email: michael.starek@tamucc.edu



June 2020

APPENDIX 3

Code Script

3.1 Code to Calculate the RMSE from a DoD

This script was written in Python 3.7.4 and uses the numpy and matplotlib libraries. The script runs on a raster in ascii format with the headers removed.

```
import numpy as np
import matplotlib.pyplot as plt

#Function to clean list: remove a specified value, any white space or new line statements, and convert to Floats
def cleaner(seq, value):
    temp = []
    for number in seq:
        number = number.strip()
        if (number != value) and (number != ''):
            temp.append(float(number))
    return temp

# function to return RMSE of list
def RMSE(list):
    return np.sqrt(np.mean(np.square(list)))

# Open raster .TXT in variable "rastertxt" ENTER DoD FILENAME AND LOCATION HERE!
rastertxt = open('placeholder_DoD_Name.txt', 'r')

# read .txt into a list
raster = rastertxt.read().split(' ')

# Remove No Data Values of -9999
raster = cleaner(raster, '-9999')

print('Total number of valid cells in DoD =')
print(len(raster), '\n')
print('RMSE of DoD =')
print(RMSE(raster), '\n')
```

```
print('Mean of DoD =')
print(np.mean(raster), '\n')
print('Minimum of DoD =')
print(np.amin(raster), '\n')
print('Maximum of DoD =')
print(np.amax(raster), '\n')
print('Standard Deviation of DoD =')
print(np.std(raster), '\n')

plt.hist(raster,bins=1000)
plt.ylabel('Number of Cells in DoD')
plt.xlabel('Original - SR Initialized meters')
plt.title('Original - SR Initialized DoD 1000 bins')
plt.show()

rastertxt.close()
#fout.close()
```